Small-scale studies of the Milky Way disc and halo gas with absorption-line spectroscopy

Dissertation

zur

Erlangung des Doktorgrades (Dr. rer. nat.)

der

Mathematisch-Naturwissenschaftlichen Fakultät

der

Rheinischen Friedrich-Wilhelms-Universität Bonn

vorgelegt von

SOROUSH NASOUDI SHOAR

aus

Teheran

Bonn 2011

Angefertigt mit Genehmigung der Mathematisch-Naturwissenschaftlichen Fakultät der Rheinischen Friedrich-Wilhelms-Universität Bonn.

1. Referent:	Prof. Dr. Klaas S. de Boer
2. Referent:	Prof. Dr. Ulrich Klein

Tag der Promotion: 27.03.2012
Erscheinungsjahr: 2012

Summary

The space between the stars is filled with atoms, charged particles (ions), molecules, and dust grains, known as the interstellar medium (ISM). Although with, on average, low densities, the ISM constitutes a laboratory of physical processes under extreme conditions, and plays a central role in the evolution of the galaxies. Progressive studies in the last decades have shown that the ISM is more complex and dynamic than previously thought, consisting of mixed gas and structures on both large and small scales. The presence of the so-called small-scale structures, structures on scales below 1 pc, has required a deeper understanding of the ISM and the physical processes involved in its evolution. Despite the number of detections, the nature of these small-scale structures is still poorly understood, and it is not always clear whether the observed changes in the optical depth or the absorption line profiles trace the variations in the densities, or changes in the physical conditions of the gas. Furthermore, a systematic study on the subject is very difficult, as the sensitivity of absorption line spectroscopy is often required, and the desired observations are limited, and not easily obtained.

Here, we use different approaches and different wavelength regimes of optical, ultraviolet (UV), and far-ultraviolet (FUV) absorption spectra, and H I 21-cm emission from single-dish radio telescopes to study the fine structures of the gas in the disc and halo of the Milky Way. The FUV range in particular, provides a unique opportunity to study a number of atoms and ions, and most importantly molecular hydrogen (H_2), which enable us to derive the physical properties of the gas, such as the temperature and the density. We further use lines of sight of small angular separations in order to study the variations in physical properties on small spatial scales. As main result, we present lines of sight towards six stars in the Large Magellanic Cloud (LMC) with projected linear extent of ~ 1.5 pc, within which we find variations in the gas temperature and in total particle volume density in the Milky Way disc gas, and indication to structures down to 0.1 pc. In two of these sightlines, we further detect H_2 in the halo gas, and find indications to overpressured small structures on scales of ~ 100 AU. The distribution of detected H_2 absorbers throughout the Galaxy further demonstrates the ubiquity of these absorbers and the cold discrete structures associated with them, the number of which is highest at low velocities, suggestively closer to the Milky Way disc. This emphasises the role of turbulences and dynamical processes driven by Galactic fountains, which can produce high-density transient regions during the cooling and fragmentation phase.

Contents

List of Figures

List of Tables

Chapter 1

Introduction

This Chapter gives an overview on the interstellar medium. It describes the distribution of interstellar matter in our Galaxy and reviews the research that has led to the discovery and further explorations of small-scale structure. The topic of this thesis is to study these substructures in the diffuse interstellar gas in the disc and halo of the Milky Way. Most of this gas is diffuse in the sense that it has low neutral gas column densities, so low that it is sometimes below the detection limit of the large H I *surveys. Therefore, the sensitivity of the absorption-line spectroscopy is required to be able to study such small structures.*

1.1 The multi-phase interstellar medium

The space between the stars is filled with atoms, charged particles (ions), molecules, and dust grains, known as the interstellar medium (ISM). Although with, on average, low densities (much lower than what could be produced on Earth), the ISM constitutes a laboratory of physical processes under extreme conditions, and plays a central role in the evolution of the galaxies.

Extended studies in new wavelength domains and with new measuring techniques have made remarkable progress in the last decades, leading to findings that have questioned our previous knowledge on the subject, and shown that the ISM is more complex and dynamic than previously thought. It was long expected that the interstellar medium consists of two "phases": a cold dense phase of neutral and molecular gas with temperatures $T < 300$ K, and a warm intercloud phase of less dense and weakly ionised gas, with temperatures $T \sim 10^4$ K, co-existing in static equilibrium. This model was put forward by Pikel'Ner (1967) and Field et al. (1969), as the first attempt to explain the inhomogeneity of the interstellar gas in density and pressure. Thanks to the technological developments, in particular with the launch of satellites in the early 1970s, the hot interstellar medium, previously predicted by Spitzer (1956) as the Galactic "corona", was recognised through the detection of C IV and O VI absorption lines. This hot coronal gas was established as the third phase with temperatures $T \sim 10^6$ K, and was understood to be unstable and widely spread, constituting most of the volume of the ISM in the Galaxy. A few years later, a three-phase model was introduced by McKee & Ostriker (1977), who managed to put forward a consistent picture of the ISM, taking the supernova explosions as the main dynamical input into an inhomogeneous cloudy medium.

Today we know that the ISM is a highly dynamical mix of gas, dominated by supernova explosions, but also by a number of other complex physical processes and dynamical inputs, such as stellar winds, expanding H II regions, turbulences, magnetic fields and cosmic rays, all affecting the interstellar gas over many different scales. The main components of this multi-phase ISM are: a warm and cold neutral medium (WNM and CNM), a warm and hot ionised medium (WIM and HIM) heated and ionised by stellar ultraviolet (UV) radiation, or by supernova shocks producing the so-called bubbles and chimneys, and molecular gas (dense clouds).

Affected by ubiquitous turbulence and ambient radiation sources, the ISM goes through a number of physical processes of heating and cooling, dissolution and fragmentation, formation of dense shells etc, all leading to the observed diverse density and temperature structures. The studies in the last three decades have shown the presence of structures on very small scales, down to a few AU. This has required a deeper understanding of the ISM and the physical processes involved in its evolution. Although the previously naive picture of the two phase ISM in equilibrium has been slowly replaced by that of a highly dynamical multi-phase ISM, consisting of mixed gas and structures on both large and small scales, a detailed model, which can quantitatively explain the observations, and be applied to all observed structures of all scales, is still lacking.

As the ISM consists of a wide variety of elements in different ionisation stages and different temperatures and densities, a number of different techniques are required to gather information from the different phases. With radio telescopes and interferometers, for example, one is able to observe the ISM through the hyperfine transition of its most abundant element H I at 21 cm, with a remarkable velocity resolution, and in this way map the distribution of neutral gas in the Milky Way. Using a stellar or extragalactic object as the background source of light, the technique of absorption-line spectroscopy enables us to detect the cool low-column density gas, and the different elements that co-exist with the H I gas, with much higher sensitivity, and with a pencil beam resolution as the light from the point source travels through the intervening gas to us observers.

Thanks to the technical developments the whole electromagnetic spectrum from γ and X-rays, to far-ultraviolet (FUV), ultraviolet (UV), optical, infrared and radio wavelengths is accessible with powerful and sensitive telescopes. There are, however, still limitations in our observations and we need to combine our careful interpretation of the collected information with theoretical modelling and physical understanding in order to reach a more complete and comprehensive picture of the ISM.

1.2 The distribution of gas in the Milky Way

The gas is not uniformly distributed in the Galaxy. Most of the Galactic gas is located in the disc of the Milky Way, co-rotating with the spiral arms and all the material within them

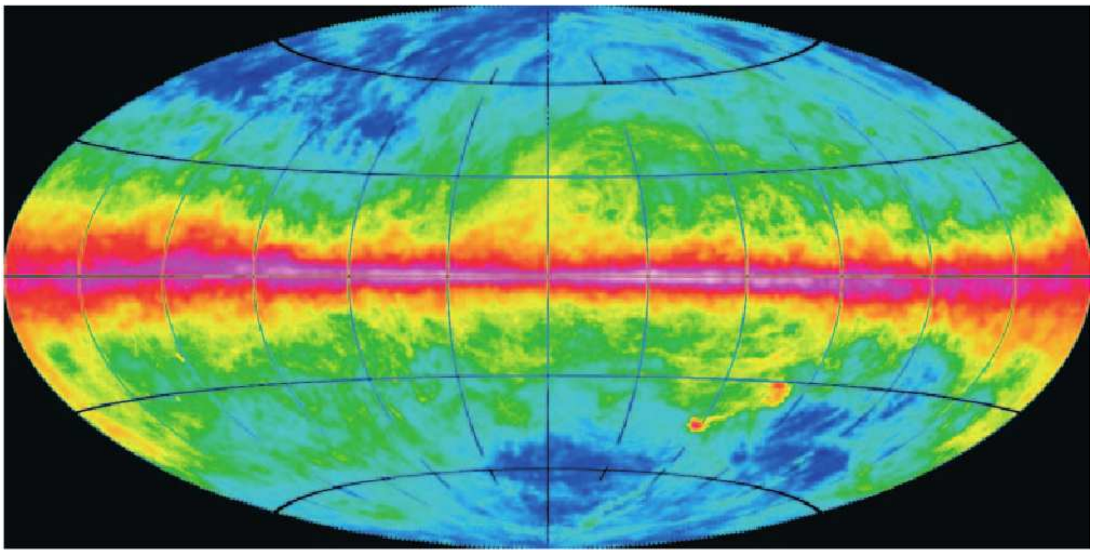

Figure 1.1: Aitoff projection all-sky map of the Galactic H I 21-cm emission based on the Leiden-Argentina-Bonn survey (Kalberla et al. 2005). The Galactic centre is in the middle. The H I emission was integrated over the velocity range $-400 < v_{\rm LSR} < +400$, yielding column densities $0 < N(\mathrm{H\,I}) < 2 \times 10^{22}\,\mathrm{cm}^{-2}$ (integrated in logarithmic scale), the value coded by colour. Figure from Kalberla et al. (2005).

around a central bulge. This is where the active star formation takes place, and where the bubbles and chimneys are formed. The disc gas is an extra-ordinarily place subject to a number of physical and dynamical processes. Fig. 1.1 shows the distribution of the neutral gas through the observed H I 21-cm emission in the Milky Way, based on the data from the Leiden-Argentina-Bonn survey (Kalberla et al. 2005). The disc gas appears within the Galactic plane (middle plane in that figure) with the highest H I column density.

Aside from the ubiquitous gas in the Galactic disc, there are also concentrations of (mainly neutral) gas in the inner and outer halo of the Milky Way, all with a range of different metal abundances. Clouds in the halo can be detected when they have radial velocities deviating from the gas that takes part in the Galactic disc rotation.[1] These detections are divided into intermediate-velocity clouds (IVCs) and high-velocity clouds (HVCs).

The origin of the halo gas falls under three main scenarios (see e.g., Bregman (2004) and references therein): 1) As a result of supernovae explosions the gas is ejected into the halo, eventually cools down, condenses, and is pulled back into the Galactic disc due to the gravitational attraction. This scenario is called the Galactic fountain model (Shapiro & Field 1976; Bregman 1980). 2) Interaction between galaxies and the Milky Way (tidal interactions, ram-pressure stripping, major and minor merging), is stripping the gas from

---

[1] There are likely halo clouds with $v_{\rm rad} \simeq 0\ \mathrm{km\,s^{-1}}$, as first pointed out by Kaelble et al. (1985). Such clouds can not be detected due to confusion by the Galactic disc gas.

the galaxy. One example for this is the gas in the Magellanic Stream with a metallicity of ~ 0.3 solar, similar to that of the Magellanic Clouds. 3) Low-metallicity gas (metallicity of ~ 0.1 solar) from the intergalactic space is falling into the halo due to the gravitational attraction of the Milky Way.

Despite the differences in the origin and properties of the IVCs and HVCs, it is not always straightforward to distinguish between these two. They are loosely characterised by their observed radial velocities. Often, this radial velocity is expressed in the local standard of rest (LSR) frame, v_{LSR}, which accounts for the peculiar motion of the Sun with respect to the Galactic rotation. The v_{LSR} can be derived from the observed (heliocentric) radial velocity v_{helio} for the certain Galactic l and b coordinates

$$v_{\mathrm{LSR}} = v_{\mathrm{helio}} + 9\cos(l)\cos(b) + 12\sin(l)\cos(b) + 7\sin(b)\,. \tag{1.1}$$

Another, more refined way of distinguishing between these clouds, and also from the disc gas, was introduced by Wakker (1991) in terms of the so-called "deviation velocity" v_{DEV}. This concept takes into account the maximum/minimum velocity of the gas participating in the disc rotation, which differs for different Galactic directions. This is expressed as

$$v_{\mathrm{DEV}} = \begin{cases} v_{\mathrm{LSR}} - v_{\mathrm{min}}, & \text{if } v_{\mathrm{LSR}} < 0 \\ v_{\mathrm{LSR}} - v_{\mathrm{max}}, & \text{if } v_{\mathrm{LSR}} > 0 \end{cases}, \tag{1.2}$$

where v_{min} and v_{max} are the minimum, respective maximum velocities expected from the Galactic disc for the given Galactic l and b coordinates.

In the technique of spectroscopy, one uses the concept of radial velocity (often in terms of v_{LSR}) and the rest-wavelength of known transitions of individual atoms/ions to identify the different gas components in the spectra. Below, these gas components are presented with respect to their v_{LSR}.

1.2.1 Local disc gas

The highest concentration of the Milky Way gas is found within a relatively thin gaseous disc with a thickness of ~ 500 pc (note the violet-coloured mid-plane of Fig. 1.1). The interstellar gas, however, extends above and below this disc into the so-called thick disc[2] with a scale height of up to $|z_{\mathrm{scale}}| \sim 1$ kpc. This transition region between the Galactic thin disc and the halo, also known as the disc-halo interface, was first discovered by Shane (1967); Lindblad (1967), but was then considered to be a relatively homogeneous envelope of H I gas surrounding the thin disc. Later studies showed that this transition region is not a smooth layer of gas, but contains cloudy structure with sizes down to few parsecs (Lockman et al. 1986; Lockman 2002).

As this material is subjected to chemical enrichment with nucleosynthetic products from the stellar interiors (ejected into the space by stellar winds and supernova explosions), the disc gas has consequently approximately solar metallicity. The disc gas is not homogeneous,

---

[2] See e.g., the review by Kalberla & Kerp (2009) and references therein.

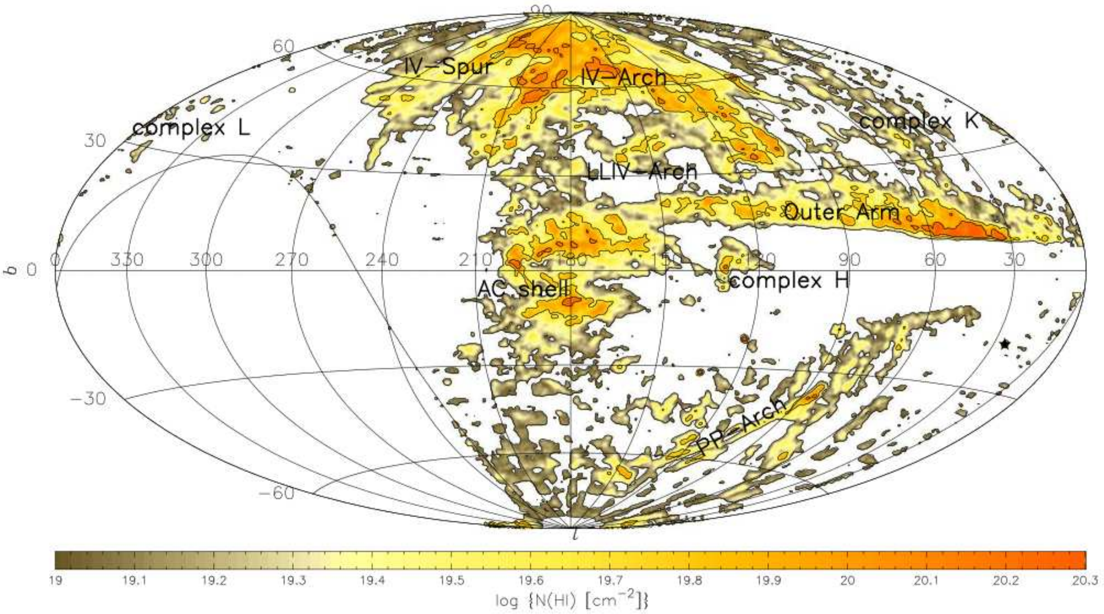

Figure 1.2: Aitoff projection all-sky map of the Galactic IVCs in Galactic coordinates, for H I column densities $N(\mathrm{H\,I}) \geq 10^{19}\,\mathrm{cm}^{-2}$, based on 21-cm data from the Leiden-Dwingeloo Survey (Hartmann & Burton 1997). The map was integrated for deviation velocities, v_{DEV}, between -35 and -90 km s^{-1}. The contour levels correspond to H I column densities of 1, 5, and 12 $\times 10^{19}\,\mathrm{cm}^{-2}$. For an all-sky map of the Galactic IVCs with positive velocities, see Wakker (2004). Figure from Wakker (2004).

but exists in a wide range of densities and temperatures. The total thermal pressure, p, of the local H I gas is believed to vary between $10^3 \leq p/k \leq 10^4$ cm^{-3} K (Wolfire et al. 1995), k being the Boltzmann constant.

The local disc gas can be observed in all sky directions, normally around $v_{\mathrm{LSR}} \simeq 0$ km s^{-1}. In some Galactic directions however, velocities of $|v_{\mathrm{LSR}}| \lesssim 25$ km s^{-1} can be expected from the gas that is dynamically connected with the disc.

1.2.2 Intermediate-velocity clouds (IVCs)

The Galactic fountain model provides one of the most successful scenarios to explain the origin of the intermediate-velocity clouds (IVCs). This exchange of the gas between disc and halo is also reflected in the nearly solar metallicities observed for most IVCs (Wakker 2001), and their both positive and negative radial velocities in the range of 30 km s^{-1} $\leq |v_{\mathrm{LSR}}| \leq 90$ km s^{-1}. Thus, the observed IVCs in the lower Galactic halo are believed to be the cooled gas which is falling back into the disc. Fig. 1.2 shows the distribution of the Galactic IVCs with deviation velocities $-35 \leq v_{\mathrm{DEV}} \leq -90$ km s^{-1}, based on H I 21-cm data from the Leiden-Dwingeloo Survey (Hartmann & Burton 1997).

Distance measurement to the IVCs (and HVCs) is not an easy task. The most direct

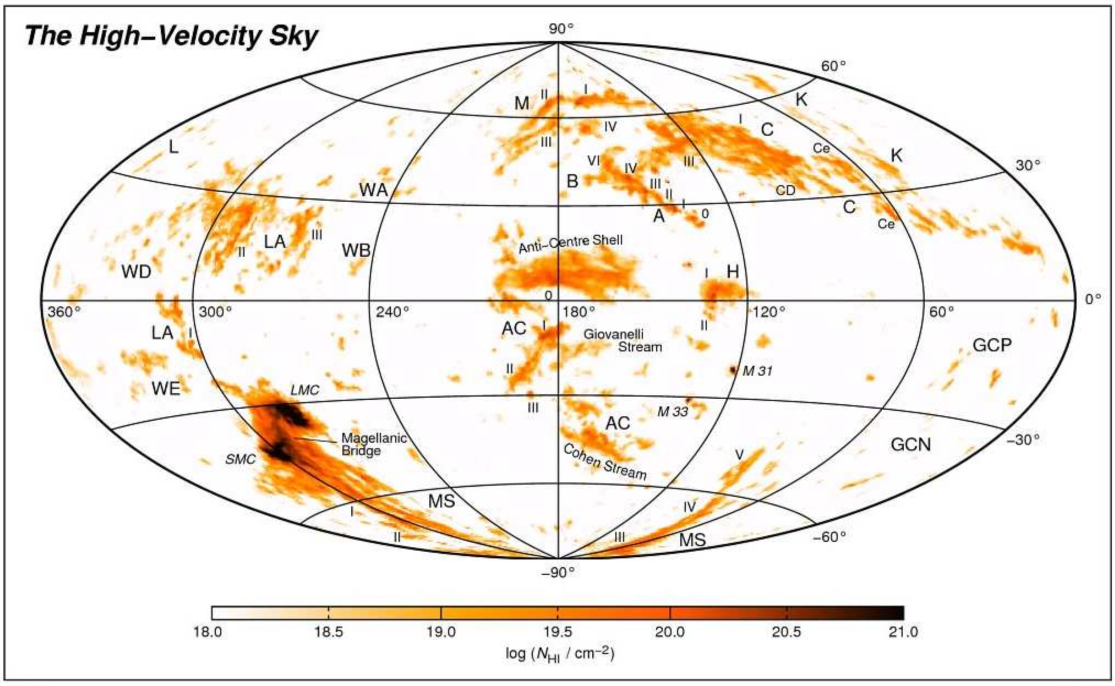

Figure 1.3: Aitoff projection all-sky map of the Galactic HVCs in Galactic coordinates, created by Westmeier (2007), based on 21-cm data from the LAB Survey (Kalberla et al. 2005), and the Milky Way model of Kalberla et al. (2007). The model was used to derive a velocity range allowed for HV gas for each position in the sky, over which the integrated column density map was created.

method is to estimate a range of distances based on the available halo stars that might be located in front of, or behind the halo gas (as indicated by the IS absorption lines). Another, less precise, method is to use the intensity of the possible Hα emission from a halo cloud to derive the distance between the stellar disc of the Milky Way and the Hα shining gas (assuming that the Milky Way radiation field is the main source of ionisation of that cloud). There has, however, been major progress recently in determining the distances to many IVCs and HVCs (Wakker 2001; Wakker et al. 2007, 2008; Thom & Chen 2008). Studies based on the former method suggest that most IVCs are at distances of $\lesssim 2\,$kpc (see Wakker (2001) and references therein). Among the IVCs with known distances are IV-Arch and LLIV-Arch with $0.5 \leq d \leq 2.0$ kpc.

1.2.3 High-velocity clouds (HVCs)

The existence of high-velocity (HV) gas in the halo of the Milky Way, discovered in H I 21-cm by Muller et al. (1963), has fascinated astronomers for many years. One speaks of HVCs, when $|v_{\rm DEV}| > 90$ km s^{-1} (see Sect. 1.2.2 for the definition of $v_{\rm DEV}$). Already in 1956, it was predicted by Spitzer (1956) that a hot Corona of gas surrounds these neutral gas clouds and provides the necessary thermal pressure to preserve the clouds. The numerous studies in new wavelength domains and with new measuring techniques have revealed more aspects on the HVCs (see e.g., Wakker et al. (2004) for an overview of these developments). Observations have also shown that HVCs are a common phenomenon both in the Milky Way, and around other galaxies (M31, M51, M101, NGC 891). Fig. 1.3 shows the distribution of the Galactic HVCs, based on H I 21-cm data from the Leiden-Argentine-Bonn (LAB) Survey (Kalberla et al. 2005).

The nature and origin of the HV gas however, still remains controversial, and is not explainable by one single scenario, as the observations show that HVCs have disparate chemical compositions. While the Galactic fountain model, mentioned earlier, is mostly valid for the IVCs, there are HVCs that can be the result of interactions between the Milky Way and neighbouring galaxies, or are composed by somewhat already processed infalling gas from the intergalactic medium, or alternatively, the remnants of early galaxy formation.

The HVCs have shown to have in general lower metallicities than the IVCs, or the disc gas, but not quite as low as one would expect for primordial gas. A range of 0.1 to 1.0 solar metallicity has been observed for a number of HVCs, and the distances are estimated to be in the range of 5 to 50 kpc (Wakker 2001; Wakker et al. 2007, 2008; Thom & Chen 2008).

To get a better understanding on the gas distribution around the Milky Way and the nature and origin of the IVCs and HVCs, the information on the metallicities and the accurate distances to these clouds are necessary, but extremely difficult to obtain.

1.2.4 Low-velocity clouds (LVCs)

Low-velocity clouds (LVCs) are nearby clouds (within $|z_{\mathrm{scale}}| < 1$ kpc) that move with absolute LSR velocities $|v_{\mathrm{LSR}}| < 50\ \mathrm{km\,s^{-1}}$. Thus they have velocities smaller than or at the low-velocity end of what is defined for IVCs (see Sect. 1.2.2), but are generally physically connected with the local disc gas. Some of these are listed in HVC catalogues (Wakker & van Woerden 1991), and some are recognised as cold infalling gas likely located in the transition region between the Galactic disc and halo (Stanimirović et al. 2006; Peek et al. 2009). However, as pointed out by Kaelble et al. (1985), and observed through the so-called low-velocity halo clouds (LVHCs, e.g., Peek et al. 2009), there are likely clouds in the halo, with very low radial velocities, which can be confused with the disc emission/absorption.

1.3 Constraints on small-scale structure in the ISM

Studies of the interstellar medium in the last decades have shown a number of observed variations on scales smaller than 1 pc, indicating the existence of the so-called small-scale structure. These have been reported at wavelengths from radio to optical, in the form of temporal or spatial variations in H I optical depth or changes in the absorption line profiles, and/or differences in particle column densities over a wide range of small spatial scales.

The typical expected scale length of the substructures in the cold neutral medium (CNM) was for long believed to be $\gtrsim 1\,\mathrm{pc}$, for the observed column densities to be in agreement with the known typical temperatures and pressures. The small-scale structures instead have volume densities and in turn pressures that are far higher than the ones expected from the CNM. The existence of these substructures is therefore puzzling, and their nature, ubiquity, and origin, still poorly understood. Our current understanding of a turbulent ISM, however, favours the idea that the small-scale structures are short-lived, transient phenomena, rather than stable clouds in a classical (thermal) pressure-equilibrium.

Below I summarise the main detections and developments on this field, with concentration on the cold neutral gas, as this is the main topic of this thesis. Fore more extensive studies, see Haverkorn & Goss (2007), and the references within the Sections below.

1.3.1 Variations in the H I opacity

The first evidence of the so-called small-scale structure was provided in 1976, based on changes in the opacity of the H I 21-cm absorption line over scales of ∼ 70 AU. This was discovered by Dieter et al. (1976), using a single-baseline VLBI observation of the quasar 3C 147.

By the end of 1980s, the search for these H I opacity variations had advanced to multi-epoch observations of H I 21-cm absorption against pulsars with time variability (Clifton et al. 1988; Deshpande et al. 1992). Pulsars are high-velocity objects. Therefore, by monitoring them over reasonable time intervals, one samples the gas on tiny scales as the line of sight is dragged across the intervening gas. Hence, the possible variations in the spectral line can be probed on the projected scales of tens to hundreds of AUs. This field of study was soon enriched with a number of new, and repeated observations (Frail et al. 1994; Johnston et al. 2003; Stanimirović et al. 2003; Minter et al. 2005; Stanimirović et al. 2010), using different radio telescopes such as Parkes, Green Bank Telescope, and Arecibo, but not all showed significant variations over the observed scales. As the technology and thereby the data quality improved, some of the earlier measured variations were questioned by the new measurements (Johnston et al. 2003; Stanimirović et al. 2003; Minter et al. 2005).

With significantly advanced interferometers, with higher resolution available, new VLBA observations of 3C 147 (previously observed by Dieter et al. 1976) were carried out, as well as several small-scale studies towards other extragalactic sources (e.g., Faison et al. 1998; Faison & Goss 2001; Brogan et al. 2005). Again, some of these observations showed significant variations on scales down to ∼ 10 to 25 AU, and some did not.

The positive detection of tiny-scale atomic structures (TSAS) in this way, indicated structures[3] of 20 to 1000 AU, with typical estimated particle volume densities of $n \sim 10^4$ to 10^5 cm^{-3}, and pressures of about $p/k \sim 10^7$ cm^{-3}K, far higher than the general densities and pressure for typical ISM. The filling factor as estimated by (Spangler & Vázquez-

---

[3] The scales mentioned in this review are mainly the transverse dimensions, based on angular separations over which the variations are observed, and not necessarily the physical size of an object.

Semadeni 2007) is, however, very low at ~ 0.001.

1.3.2 Tracing small-scale structures in the optical domain

Spatial or temporal variations in the shape of the absorption line profiles were seen already long ago (Münch 1953). Münch (1957) further recognised variations in the optical absorption lines that were not seen in the associated H I 21-cm data (observed with a larger beam). However, it was only recently that a new approach took form by analysing total gas column densities, or changes in the physical conditions based on the tracing ions such as Na I, Ca I, Ca II, K I, and Ti II. As these elements are depleted (or highly depleted in case of Ti II) into dust grains, and/or affected by the ionisation condition in the gas, the observed variations can be used to trace the changes in the local physical conditions of the gas, although such interpretation is not always straightforward. As the H I small-scale structure studies advanced, this new approach also developed, using absorption-line spectroscopy of stars in globular clusters, open clusters, binary stars, and proper-motion stars.

Globular clusters, containing many background stars with small angular separations, provide a grid of very close sightlines with angular scales of only few arcseconds. The optical high spectral resolution studies of stars in globular clusters have in this way traced column density variations in mainly interstellar Ca II and Na I absorption lines on scales down to 0.01 pc (e.g. Cohen 1978; Bates et al. 1990, 1991, 1995; Meyer & Lauroesch 1999; Andrews et al. 2001).

Using high spectral resolution observations of mainly Na I in the foreground of nearby binaries and multiple star systems with angular separations of < 20 arcsec, variations on the projected scales of 500 to 30000 AU have been probed (e.g., Meyer 1990; Watson & Meyer 1996; Lauroesch et al. 2000). In some other cases, where a proper-motion star was the target, the repeated observations have revealed the spatial variations in the gas on scales smaller than the ones provided by multiple stars and binaries, as the lines of sight sample different parts of the same cloud at different times (Welty & Fitzpatrick 2001; Welty 2007). When measurements on small-scale structure were repeated, temporal variations have been found in several cases. Examples have been presented in the above cited investigations by, e.g., Lauroesch et al. (2000), and Lauroesch & Meyer (2003)[4].

Thus, optical absorption-line studies have shown structures in the diffuse ISM on scales of order of 1000 AU. Variations in the absorption lines have been probed also on an order of magnitude smaller scales, but these structures are not as pervasive.

---

[4] It should be pointed out that there are more variations reported in the literature, many of which are suspected to be associated with filamentary structures in the shells of supernova remnants, or associated with hot stellar environment, where the motion of the foreground gas itself can produce the variability.

1.3.3 FUV/UV tracers of small-scale structures and molecular substructures

As mentioned above, in optical absorption-line spectroscopy most cases of temporal or spatial small-scale structures are observed as the variations of mainly Na I and Ca II absorption line profiles. It is not always clear whether these trace the variations in the densities, or changes in the physical conditions of the gas. There have been follow-up UV-observations in some cases, providing further interpretations on these results. Using absorption lines from fine-structure levels of C I in UV spectra, valuable information can be gained about the physical properties of the gas, such as density and pressure (de Boer & Morton 1974; Jenkins & Tripp 2001). Based on this, e.g., Welty (2007) discovered that the observed variations in Na I and Ca II lines towards HD 219188 reflect the variation in the density and ionisation in the gas, and do not refer to high-density clumps.

There are a number of studies on the substructures in the gas, observed in molecules, such as e.g., H_2, CO and CH (Pan et al. 2001; Lauroesch et al. 2000; Richter et al. 2003a,b; Heithausen 2002, 2004; Marggraf et al. 2004; Boissé et al. 2009). Heithausen (2004) discovered substructures in the molecular gas (based on CO observations), on scales of few hundred AU, corresponding to high densities ($n \sim 10^3$ to 10^4 cm^{-3}) and low masses ($\sim 10^{-3}\,M_\odot$), and came to the conclusion that these structures have too low mass to be gravitationally bound. On a smaller scale of 5 to 104 AU, Boissé et al. (2009) found no variation in the column density of the H_2, observed over a period of almost five years towards the Galactic high-velocity star HD 34078. This despite the variations in the CH column densities found over the same period. They concluded that the variation in CH and CH^+ should be due to the chemical structure of a gas that is in interaction with the star itself. H_2 on the other hand, located in a quiescent gas unaffected by the star, remains homogeneously distributed. Hence no small-scale density structure was proposed in the quiescent gas within this scale.

A different approach was used by Richter et al. (2003a,b) using the many absorption lines of molecular hydrogen in the Lyman and Werner bands. Their study suggested that the partly molecular halo gas in the observed line of sight resides in a dense filament, which possibly corresponds to the tiny-scale atomic structures in the diffuse ISM (Richter et al. 2003a).

1.3.4 Possible explanations and ISM modelling

Observations of H I opacity variations, or column density variations of neutral, ionised, or molecular tracers, point to structures with inferred typical densities and pressures far higher than what can be expected from the interstellar medium. Several attempts have been taken in order to explain the various observations, whether by providing a solution to the density and pressure problem, or rather giving a description of the interstellar properties that would lead to such observed spatial variations:

- Geometric solution suggested by Heiles (1997). In this model, the "actual" volume densities and pressures are not as extreme as the values implied from observations, provided that these discrete structures are very cold, non-spherical, and highly anisotropic. For this, so-called filaments and sheets were suggested which happen to be aligned with the actual lines of sight, when the small-scale structures (or even tiny-scale atomic structures, TSASs) are observed. More observations would be necessary here to investigate the frequency of this phenomenon and the chance alignments.

- Fractal geometries driven by turbulences (Elmegreen 1997). The small variations might reflect fluctuations in the physical conditions, driven by turbulent motions (Elmegreen 1997, 1999; Cho et al. 2002).

- Separate population of cold dense self-graviting clouds (Walker & Wardle 1998; Draine 1998; Wardle & Walker 1999). Such AU-sized cloudlets (provided a mass on the order of $\sim 10^{-3}\,M_{\odot}$) can, according to these authors, cause microlensing of optical light. Such clouds are also proposed to account for the missing baryonic dark matter (Pfenniger et al. 1994; de Paolis et al. 1995; Gerhard & Silk 1996; Walker & Wardle 1998).

- Statistical fluctuations, proposed by Deshpande (2000), separate from all the other explanations. Deshpande (2000) concludes that the variations in optical depth observed for two different lines of sight of certain separation does not refer to a cloud with that projected size, but is rather due to the optical depth function in a medium containing density and velocity structures on all scales, which can be represented by a spatial power law. Thus, the small-scale structures are observational projection effects.

- Temporary structures with somewhat higher temperature than the CNM, resulted from discrete objects or turbulent fluctuations (Jenkins & Tripp 2001; Jenkins 2004).

If these structures represent density and pressure enhancements, a true theoretical challenge is to generate models for these structures to exist in the embedded low-density warm neutral and ionised medium. With recent developments in the field, the simple equilibrium descriptions in the theoretical models have been replaced by a complicated, highly dynamical, turbulence dominated medium, considering structures on both large and small scales (see reviews by Vazquez-Semadeni et al. 2000; Ballesteros-Paredes et al. 2007). For this, there are simulations which take into account the role of Magnetic hydrodynamic waves in mediating turbulent pressure balance (Mac Low et al. 2005; de Avillez & Breitschwerdt 2005). There are however a number of unsolved issues here which require more detailed analysis.

1.4 Thesis content

Despite the number of detections of the small-scale variability in the interstellar gas, not enough effort has been made to understand the nature and the physical properties such as actual sizes and densities of these structures. However, the volume filling factor of these structures is expected to be low, which makes a systematic study on the subject very difficult. Thus, questions on the nature and ubiquity of the small-scale structures remain without definite answers.

It is useful to combine the observations from different wavelength regimes when studying these structures, although the desired observations are limited, and not always available, or easily obtained. While the optical absorption-line spectroscopy provides sensitive pencil beam information with high spectral resolution, helping to resolve the gas components along a line of sight and to trace the diffuse ISM, it comes with little direct information on the actual physical conditions of the gas. Yet, such informations are crucial for understanding the nature of these structures. Furthermore, for better understanding the morphology of the ISM structures on small scales, the spatial information is needed to be combined with the physical path length of the absorbers along a line of sight, in order to get a three-dimensional view of the structures we study. These are the topics of this thesis.

In this work, different wavelength regimes, and approaches have been used to study the Milky Way disc and halo gas on small scales. The main emphasis is placed on the H_2, as the analysis of the absorption by this molecule will yield important information about the physical conditions in the gas. The UV and FUV spectral ranges further offers a unique opportunity to study a number of abundant atoms and their ions, which have many of their transitions within this wavelength regime. For the spatial resolution, the Large Magellanic Cloud (LMC), with many bright stars spread over a small field of view, provides an excellent background with large and small angular separations.

The outline of this thesis is as follows:

- In Chapter 2, I review the physics of the absorption and emission lines, and describe how information can be gained from the observations, and how it can be used in interpreting the interstellar gas properties.
- As H_2 serves as an important source of information for the physical properties of the gas, I dedicate Chapter 3 to the special nature of molecular hydrogen.
- In Chapter 4, I describe the basics of the data used in this work, and describe the methods. A more detailed analysis is given within the corresponding Chapters when necessary.
- In Chapter 5, I present six LMC lines of sight, towards which variations are found in column densities of H_2 in the Milky Way disc gas, and trace these variations to the actual density variations and changes in the physical properties of the gas.
- In Chapter 6 two LMC sightlines are presented, showing detection of H_2 in the halo intermediate-velocity gas. Based on these detections, the implications to small-scale structures are discussed.
- In Chapter 7, I discuss the low-column density halo structures detected in optical Na I (and possibly Ca II) towards QSOs, and their possible indication of small sized

clumps. These structures are then compared to the ones detected by H_2 absorption in this work and in some other studies, based on which possible constraints on the small-scale structure are discussed.

- Chapter 8 contains the summary and the overall conclusions of this work, as well as the outlook.

Chapter 2

Physics of interstellar spectral lines

In this Chapter, the background in physics relevant to this work is given, which helps in understanding how information can be gained from the observations, and how it can be used in interpreting interstellar gas properties.

2.1 Background sources of light

To study cool "invisible" neutral[1] gas which does not emit light in a significant manner, one uses the technique of absorption-line spectroscopy. Before the invention of radio telescopes this was essentially the only method, and still today it is the most sensitive one to obtain information about the neutral gas, provided that there are background sources of light. These can be any form of continuum radiation sources, such as stars, quasi-stellar objects (QSOs), active galactic nuclei (AGNs), and gamma-ray bursts (GRBs). As the light of these sources passes through the intervening gas, the photons of specific energies get absorbed and give rise to absorption lines, each with a wavelength corresponding to the energy of the absorbed photon. The detected absorption lines in this way give clues to the atoms present in the gas, the chemical composition, and the physical conditions.

2.1.1 Hot OB stars

OB stars are one of the most suitable background sources. These are luminous hot stars (effective temperature $T_{\rm eff} > 20,000$ K), of spectral types O and B, which emit strong far-ultraviolet (FUV) and ultraviolet (UV) radiation. Such radiation unveils most interstellar species, because many atoms and ions have their resonance spectral lines within the FUV and UV range. As a result, an observed spectrum is the stellar continuum flux with structures driven by possibly stellar wind, broad stellar lines, P-Cygni profiles[2], and a

---

[1] Neutral gas means that the hydrogen is mainly neutral, while other elements can exist in both neutral and ionised forms.

[2] A P-Cygni profile is characterised by a broad emission line with a corresponding blueshifted absorption, produced by an expanding gaseous shell moving away from the star.

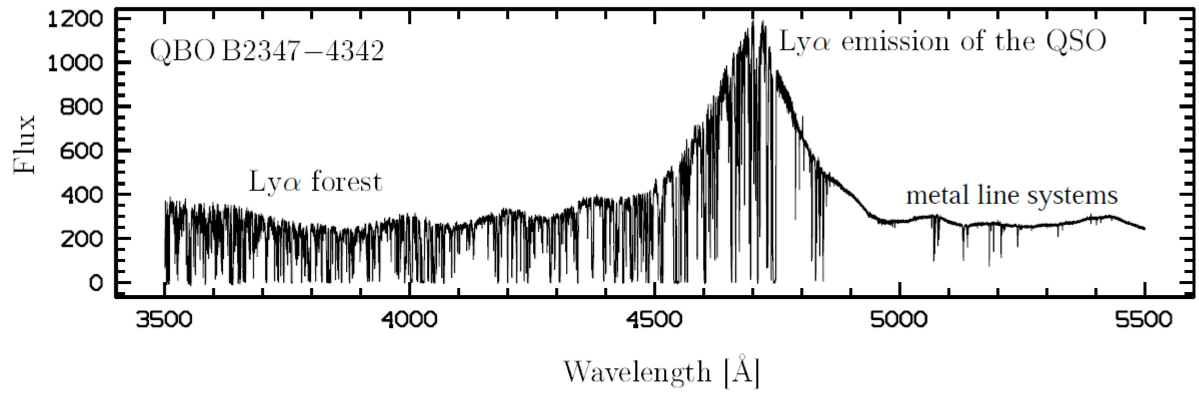

Figure 2.1: Spectrum of QSO B2347−4342 (at redshift $z = 2.9$) observed with VLT/UVES. The Lyman-α emission line of the QSO is redshifted to $\lambda \sim 4700\,\text{Å}$, on the left side of which there are the many absorption lines of the Lyman-α forest, and on the right side mainly some of the intervening metal absorptions. Figure from Ben Bekhti (2009).

large number of weak and strong interstellar absorption lines.

Another advantage of measurements using nearby stars in the halo or in the Magellanic Clouds as background lightsources is the upper distance limit to the gas, set by the distance of the star. This is useful when studying the gas of higher radial velocities to make sure that the gas indeed belongs to the Milky Way halo, a certainty which is not provided by the extragalactic background sources.

Although OB stars are convenient background sources to study the Milky Way disc and halo gas, the number of appropriate stars that can be used is limited, and they are not distributed homogeneously over the whole Galactic sky.

2.1.2 QSO spectra

There are many aspects that make QSOs useful targets for observations in astrophysics. Being distant extragalactic bright objects, the spectra of QSOs reveal a substantial amount of astrophysical information, not only on the interstellar gas of the Milky Way, but also on the intergalactic gas, and the gas in the haloes of other galaxies. The UV light of a QSO (like any other type of extragalactic source) is absorbed by the intervening H I gas between the QSO and the observer, giving rise to Lyman-α lines (first observed by Bahcall & Salpeter 1965). This intervening H I gas belongs to the intergalactic medium (IGM) at all redshifts; or is sometimes related to galaxies and protogalaxies which the line of sight is passing through, resulting in multiple absorptions of velocity-shifted wavelengths on the left side (shorter wavelength) of the Lyman-α emission of the QSO. Thus, the spectra of QSOs can be studied for many reasons, and consequently they are frequently observed. Being extragalactic objects distributed over all directions on the sky, they also represent appropriate background sources for mapping the distribution of the gas in the outer regions of the Milky Way.

A QSO spectrum consists of a power-law continuum, with a peak Lyman-α emission, on the blue (left) side of which there are the many absorption lines of Lyman-α forest, and on the red (right) side few absorption lines, mainly by intervening metal absorptions (see Fig. 2.1). Due to the complexity of the line identifications for the many absorbers in the QSO spectra, it is favourable to use doublet lines such as Ca II (λ_0: 3934.8, 3969.6 Å) and Na I (λ_0: 5891.6, 5897.6 Å) in the optical, or Mg II (λ_0: 2795.5, 2802.7 Å) in the UV, when studying the interstellar absorption in the disc and halo of the Milky Way.

2.2 Absorption lines

2.2.1 Radiation transport and optical depth

When the electromagnetic radiation from a thermal source passes through a medium, the photons of particular frequencies get absorbed, emitted (or re-emitted), or scattered by atoms and ions of the medium. Consequently, the total intensity, I_ν, changes over the distance ds according to the radiative transfer equation

$$\mathrm{d}I_\nu = -\kappa_\nu I_\nu^0 \mathrm{d}s + j_\nu \mathrm{d}s\,, \tag{2.1}$$

where I_ν^0 is the incident intensity, and κ_ν and j_ν are the absorption respective emission coefficients.

The light which is removed from the beam (by absorption or scattering) is expressed in terms of optical depth τ_ν, a measure of transparency of the medium

$$I_\nu = I_\nu^0\, \mathrm{e}^{-\tau_\nu}\,, \tag{2.2}$$

where τ_ν is correlated with the absorption coefficient via: $\tau_\nu \equiv \int \kappa_\nu \mathrm{d}s$.

The optical depth increases with the number density of particles (n) along the path through the cloud (of the length ds), given by

$$\tau_\nu = \int_0^s n\sigma_\nu\, \mathrm{d}s\,, \tag{2.3}$$

where σ_ν is the scattering cross-section, described in Sect. 2.2.2 below.

Normally, what we observe in absorption (and emission), is the total number of the particles (and not the number density) along a certain line of sight, which produce the absorption (or emission) line. This quantity is referred to as the column density N, which is defined as the number of particles per cm^2 in a cylinder along the path of the medium. Thus, along a certain line of sight we have: $\tau_\nu = N\,\sigma_\nu$, where N is the total number of particles over the path ds.

2.2.2 Transition probabilities

The optical depth as a function of frequency can be expressed more explicitly, in terms of the profile shape function $F(\nu)$ (explained in detail in Sect. 2.2.3), the atomic structure constant $\frac{\pi e^2}{m_e c}$, the oscillator strength f_{lu}, and the particle volume density n

$$\tau_\nu = \frac{\pi e^2}{m_e c}\, f_{lu}\, F(\nu)\mathrm{d}\nu \int_0^s n\, \mathrm{d}s \,, \tag{2.4}$$

where m_e is the electron mass, and $\frac{\pi e^2}{m_e c}\, f_{lu}\, F(\nu)$ the scattering cross-section σ_ν in Eq. (2.3). f_{lu} is the transition probability expressed in terms of oscillator strength, also called f-value, and is related to the Einstein constant B_{lu} (for absorption) through

$$f_{lu} = \frac{m_e c}{\pi e^2}\, h\nu\, B_{lu} \,, \tag{2.5}$$

where the subscripts l and u are the lower and upper states, respectively.

The f-value is a dimensionless number and ranges from 0 to 1 (stronger transitions will have an f-value closer to 1, and degeneracy of real electronic systems gives a value greater than 1). This value is mostly determined from empirical laboratory measurements, but may also be calculated theoretically.

Thus the observed absorption lines carry information on the discrete processes in the medium through which the photons have travelled. To obtain this sort of information we need to understand the characteristics of the observed spectral lines.

2.2.3 The spectral line profile

The shape of a spectral line produced by a specific atomic transition is the result of the intrinsic line profile, and the Maxwellian velocity distribution of the absorbing particle, and thus can be described by the two functions: Lorentz function $L(\nu)$, and Gauss function $D(\nu)$. The convolution of the two makes the observed profile, the Voigt function (detailed derivation of these functions can be found in e.g., Gray (1992), or similar astrophysical notes).

Lorentz function

Even for a motionless isolated atom, a certain broadening of the radiative bound-bound transitions, so-called natural broadening, or radiative damping, occurs. This is due to the finite lifetime of the upper state imposed by spontaneous deexcitation. Spontaneous deexcitation to lower states diminishes the population of the upper states, with the transition probabilities: $\gamma_u \equiv \sum_l A_{ul}$, where A_{ul} is the Einstein coefficient for spontaneous emission. Thus the time interval, during which the electron will probably stay in the upper state u, can be obtained from: $\Delta t = 1/\gamma_u$. The spread in the energy (and so in the frequency) follows according to Heisenberg's uncertainty principle: $\Delta E = \hbar/\Delta t$, and is associated with

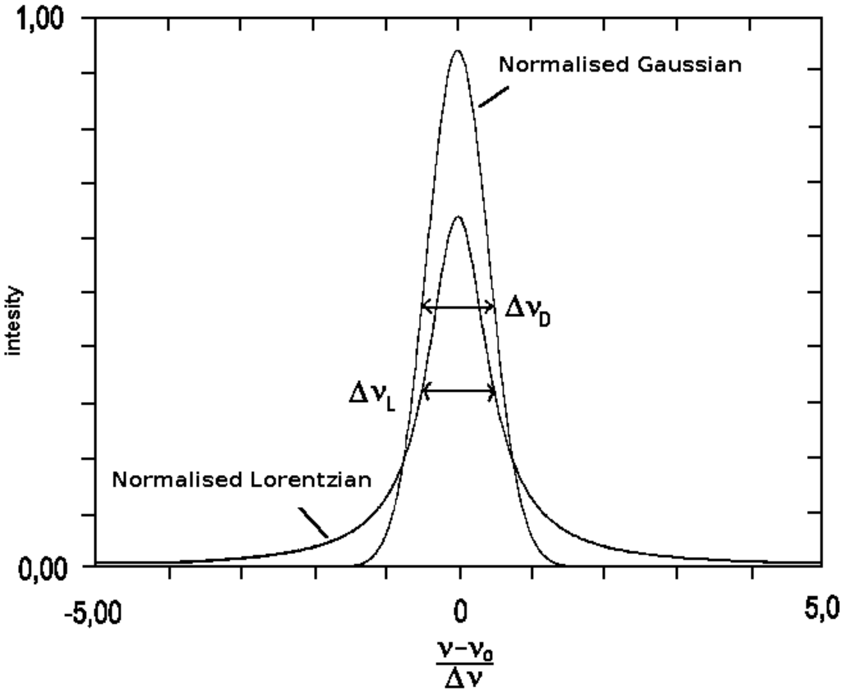

Figure 2.2: Comparison of Gaussian and Lorentz profile of similar width ($\Delta\nu_{\mathrm{D}} \approx \Delta\nu_{\mathrm{L}}$). $\Delta\nu_{\mathrm{D}}$ and $\Delta\nu_{\mathrm{L}}$ are the FWHM of the Gaussian and the Lorentz profile, respectively (see Sect. 2.2.3 for more details). Figure was taken from `http://www.pci.tu-bs.de/aggericke/PC4e/Kap_III/Linienbreite.htm`, and slightly modified.

the finite lifetime of the particle in state u, by: $\Delta E \approx \hbar\gamma$, where γ is called the damping constant of the transition.

This intrinsic characteristic of the absorption is described by the so-called Lorentz function $L(\nu)$, which is the Fourier transform from the time domain to the frequency domain, describing the distribution about the line frequency ν_0

$$L(\nu) = \frac{\gamma/4\pi^2}{(\nu-\nu_0)^2 + (\gamma/4\pi)^2} \,. \tag{2.6}$$

The function is normalised according to $\int_0^\infty L(\nu)\mathrm{d}\nu = 1$.

The Lorentz profile has a sharp peak at ν_0, with a full width at half maximum (FWHM) set by the damping constant: $\Delta\nu_{\mathrm{L}} = \gamma/2\pi$. The wings of the Lorentzian profile, called damping wings, decline according to $1/(\nu-\nu_0)^2$ (see Fig. 2.2).

Gauss function

The thermal and turbulent motions of atoms or molecules, cause a Doppler shift in the velocities of the particles. The temperature-dependent spread in particle velocities is described statistically by a Maxwell-Boltzmann distribution for the fraction of particles in a sample in equilibrium at a temperature T, having a velocity between v and $v + \mathrm{d}v$

$$n(v)\mathrm{d}v = 4\pi n \left(\frac{m_a}{2\pi kT}\right)^{3/2} \exp\left(-\frac{m_a v^2}{2kT}\right) v^2 \,\mathrm{d}v \,, \tag{2.7}$$

where m_a is the mass of the atom, and k the Boltzmann constant.

Along a line of sight, this is observed as a spread in frequencies of the interacting photons, and results in the broadening of the spectral line. The profile is consequently described by a Gauss function (also called for Doppler profile)

$$D(\nu) = \frac{1}{\sqrt{\pi}\Delta\nu_{\mathrm{D}}} \exp\left[-\left(\frac{\nu-\nu_0}{\Delta\nu_{\mathrm{D}}}\right)^2\right] , \tag{2.8}$$

where $\Delta\nu_{\mathrm{D}} = \frac{\nu_0}{c}\sqrt{\frac{2kT}{m_a}}$ is the most probable deviation from the rest frequency, reflecting the most probable speed of the particles.

The FWHM of the Gauss function is usually much broader than the natural broadening (the FWHM of the Lorentz function) of the line. The wings however, fall off much faster than the wings of the Lorentz profile due to the exponential tail of the Maxwellian distribution (see Fig. 2.2[3]).

Voigt profile

The final spectral profile, the Voigt profile, $F(\nu)$, is the convolution of the Lorentz profile (Eq. (2.6)) and the Doppler profile (Eq. (2.8)). This can not be derived analytically, but is closely related to the Hjerting function (Hjerting 1938), and can be written as

$$F(\nu) = L(\nu) * D(\nu) = \int_{-\infty}^{+\infty} L(\nu - x) D(x) \mathrm{d}x = \frac{1}{\sqrt{\pi}\Delta\nu_{\mathrm{D}}} H(\alpha, z) , \tag{2.9}$$

where $H(\alpha, z)$ is the Hjerting function

$$H(\alpha, z) = \frac{\alpha}{\pi} \int_{-\infty}^{+\infty} \frac{e^{-y^2}}{(z-y)^2 + \alpha^2} \mathrm{d}y , \tag{2.10}$$

with $\alpha = \frac{\gamma/2}{2\pi\Delta\nu_{\mathrm{D}}}$ and $z = \frac{\nu-\nu_0}{\Delta\nu_{\mathrm{D}}}$.

Generally, the width of the Lorentzian profile is much smaller than the one of the Doppler profile. For $\Delta\nu_{\mathrm{D}} \gg \gamma$, we have $\alpha \ll 1$ and the resulting profile will be close to a Gaussian, with the width decided by the $\Delta\nu_{\mathrm{D}}$. For $\alpha \gg 1$ on the other hand, $H(\alpha, z)$ becomes more complicated, and the profile is no longer a Gaussian. Here the damping wings of the Lorentzian profile appear in the Voigt profile. This behaviour of the absorption line profile with the optical depth of the medium is more explicitly described in Sect. 2.3.

2.2.4 Measurements of absorption lines

Equivalent width

The strength of the observed absorption line depends on the discrete atomic processes: the probability of the particular transition, the amount of particles within a column contributing to the absorption, and the thermal and turbulent motion in the gas.

---

[3] Note that in Fig. 2.2 the FWHM of the Lorentz function is as broad as the FWHM of the Gauss function. The consequence of this in the observed absorption profiles will be discussed later in Sect. 2.3.

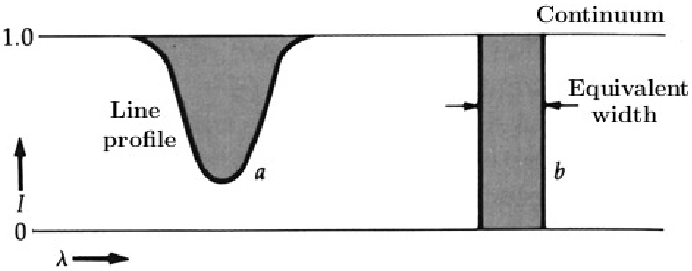

Figure 2.3: Shows an absorption line profile (a), and its equivalent width (b) for a normalised continuum. The grey region in (a) has the same area as the one in (b). Figure from `http://ircamera.as.arizona.edu/astr_250/Lectures/Lec_15sml.htm`.

The strength of the spectral line is expressed in equivalent width, W_λ: the width of a rectangle, with the length up to the continuum level I_cont, that has the same area as the integrated area under the absorption line profile (expressed in wavelength instead of frequency)

$$W_\lambda = \int_0^\infty \frac{I_\text{cont} - I_\lambda}{I_\text{cont}}\,\mathrm{d}\lambda = \int_0^\infty (1 - e^{-\tau_\lambda})\,\mathrm{d}\lambda\,. \tag{2.11}$$

For a normalised continuum, $I_\text{cont} = 1$, the W_λ is directly gained from the integrated area of the absorption line (see Fig. 2.3).

Doppler parameter

As mentioned, $\Delta\nu_\text{D}$ (or $\Delta\lambda_\text{D}$), corresponds to the most probable value in the particle velocity distribution. This parameter is referred to as the Doppler parameter, or the b-value ($b = \frac{c}{\lambda_0}\Delta\lambda_\text{D}$), expressed in [km s^{-1}], and describes the degree of the line broadening. Physically, the Doppler parameter is not only caused by the temperature, but also by the turbulent motions of the particles[4]. Assuming that the turbulent velocities also follow a Gaussian distribution, the total b-value can be written as the sum of a thermal b_therm, and a turbulent b_turb component

$$b = \sqrt{b^2_\text{therm} + b^2_\text{turb}}\,, \tag{2.12}$$

with the thermal component being related to the temperature of the gas, and the mass of the atom

$$b_\text{therm} = \left(\frac{c}{\lambda_0}\right)\Delta\lambda_\text{D} = \sqrt{\frac{2kT}{m_a}} = 0.129\sqrt{\frac{T}{A}}\,, \tag{2.13}$$

where A is the atomic weight of the particle.

2.3 Curve of growth (CoG)

The increase of the equivalent width as a function of the number of absorbing atoms (in N [cm^{-2}]) in a specific state, can be expressed logarithmically in graphic form of the so-called curve of growth (CoG, Fig. 2.4). As an absorption line is specified by its wavelength, and has a strength depending on the transition probability (expressed in terms of f-value),

---

[4] Only microturbulence contributes to the broadening of individual interstellar absorption lines.

and the amount of the absorbing material N, the behaviour of equivalent width is changing with all these three parameters. This rather complicated function can be divided into three different regimes, based on the opacity of the intervening material (for more detailed derivations, see e.g., Draine 2011).

- **Optically thin case $\tau \ll 1$, linear or Doppler part of the CoG:**

  For small optical depth, the equivalent width from Eq. (2.11) can be simplified to

  $$W_\lambda = \int_0^\infty (1 - e^{-\tau_\lambda})\,\mathrm{d}\lambda = \int_0^\infty \tau_\lambda\,\mathrm{d}\lambda\,. \tag{2.14}$$

  Recalling Eq. (2.4), and Eq. (2.9), W_λ can be expressed as

  $$W_\lambda = \frac{\pi e^2}{mc} f_{lu} \int_0^s n\,\mathrm{d}s \int_{-\infty}^{+\infty} \frac{\lambda^2/c}{\sqrt{\pi}\Delta\lambda_\mathrm{D}} H(\alpha, z)\,\mathrm{d}\lambda\,. \tag{2.15}$$

  For small optical depth, where $\alpha \ll 1$, the profile of the line can be simplified to a Doppler function, thus

  $$\int_{-\infty}^{+\infty} \frac{\lambda^2/c}{\sqrt{\pi}\Delta\lambda_\mathrm{D}} e^{-\left(\frac{\nu-\nu_0}{\Delta\nu_\mathrm{D}}\right)^2} \mathrm{d}\lambda = \frac{\lambda^2}{c}\,, \tag{2.16}$$

  and we obtain for a line of sight with $\int n\,\mathrm{d}s = N$, the relation

  $$\frac{W_\lambda}{\lambda} = \frac{\pi e^2}{mc^2} N f_{lu} \lambda\,. \tag{2.17}$$

  Thus, for small optical depth the equivalent width increases proportionally to N, independent of the Doppler broadening of the line. This is the linear, or the Doppler part of the CoG (the absorption line profile is described by a Doppler/Gaussian profile).

- **Intermediate optical depth $\tau \sim 1$, flat or logarithmic part of the CoG:**

  As the centre of the line becomes optically thick, the wings start to deepen (see Fig. 2.4.b). This causes only little change in the equivalent width of the line, and for a constant b-value, W_λ increases proportionally to the logarithm of N

  $$\frac{W_\lambda}{\lambda} \propto \log(N f_{lu} \lambda)\,. \tag{2.18}$$

  Here, the absorption line profile can no longer be described by a Gaussian function, and the integration of the profile as a function of optical depth becomes analytically impossible. Instead the equivalent width can be related to the optical depth at the centre of the line τ_0

  $$\frac{W_\lambda}{\lambda} \approx 2\,\frac{b}{c}\sqrt{\ln(\tau_0)}\,, \tag{2.19}$$

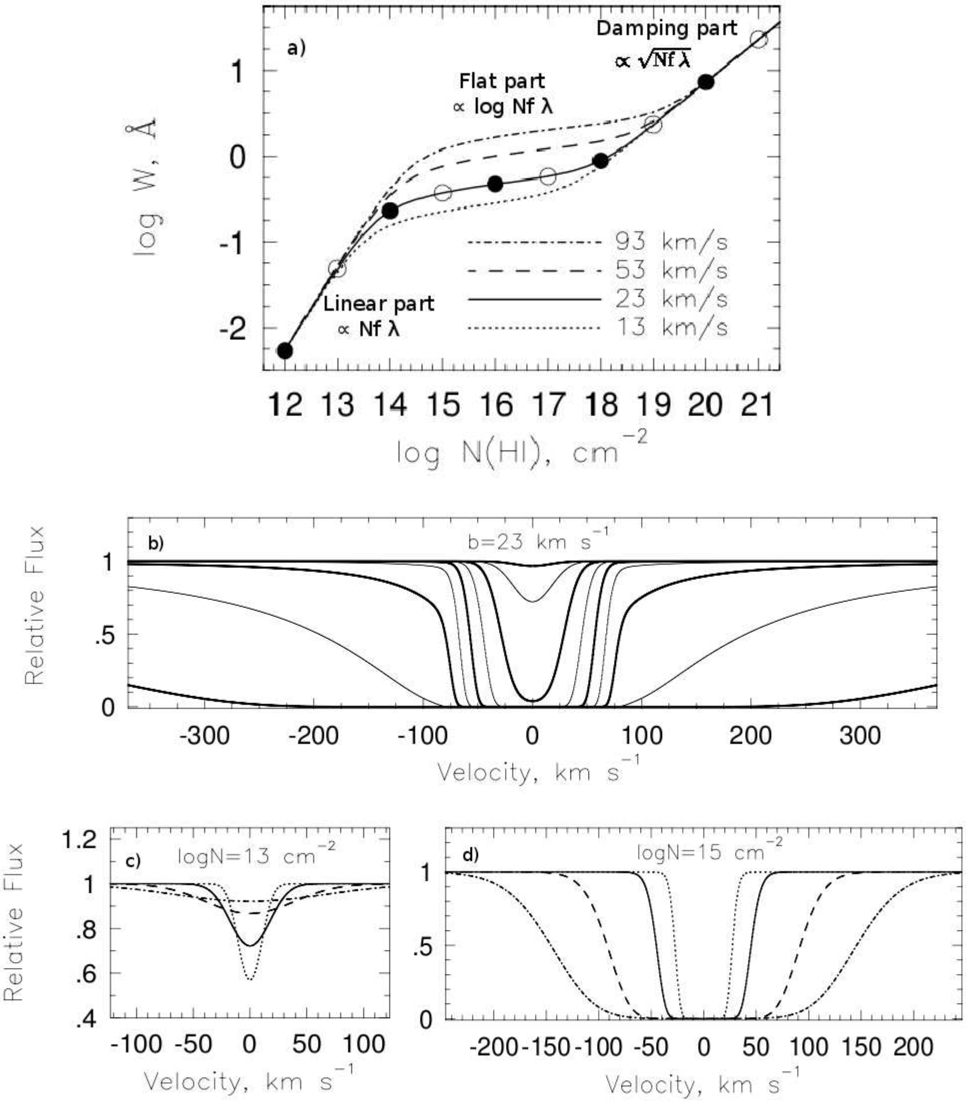

Figure 2.4: Illustrates the CoG for different Doppler parameters, and the absorption profiles related to the different regimes. **a)** The CoG for the Lyman-α transition, showing the logarithmic relation between the equivalent width W [Å], and the column density $N(\mathrm{H\,I})$ [cm^{-2}], for different b-values of: $b = 13, 23, 53, 93$ km s^{-1}(presented in the lower right part of the plot). The different regimes (linear, flat, and damping part) are also indicated. The filled and empty circles on the solid curve ($b = 23$ km s^{-1}) correspond to the absorption profiles in b). **b**) shows absorption profiles with $b = 23$ km s^{-1} for $\log N(\mathrm{H\,I}) = 12$ to 20. The thick curves correspond to the filled circles in a), and the thin ones to the open circles. **c)** Shows how the strength of the absorption lines, corresponding to the linear (or Doppler) part of the CoG, do not depend on the b-value. The different lines correspond to the different b-values (see a)), while the column density, $\log N(\mathrm{H\,I})$ = 13, is kept the same. All profiles correspond to the same equivalent width. **d)** Shows profiles corresponding to the flat part of the CoG, with $\log N(\mathrm{H\,I}) = 15$, but for different b-values. The core of the line is optically thick, and the only significant change in the equivalent width is made by the contribution of the Doppler parameter in the wings. This figure was taken from Charlton et al. (2000), and slightly modified.

where

$$\tau_0 = 1.497 \times 10^{-15} \frac{N f_{lu} \lambda}{b} \,. \tag{2.20}$$

Contrary to the optically thin case, here the determination of N is highly dependent on the Doppler parameter of the absorption, and very uncertain except when several lines of the same ion are used.

- **Optically thick case $\tau \gg 1$, damping or square-root part of the CoG:**

  For very high densities, the medium becomes optically thick, $\alpha \gg 1$ (Eq. (2.10)), and the Lorentz function dominates over the Doppler function.

  The Hjerting function (Eq. (2.10)) can now be approximated to $H(\alpha, z) \approx \alpha/(\sqrt{\pi} z^2)$. Thus the line profile as a function of wavelength, $F(\lambda)$ (Eq. (2.9)), can be simplified to

  $$F(\lambda) = \left(\frac{\lambda^2}{4 c \pi^2} \right) \frac{\gamma}{(\lambda - \lambda_0)^2} \,. \tag{2.21}$$

  The damping wings of the Lorentzian profile $(1/(\lambda - \lambda_0)^2)$ start to contribute to the wings of the line, and cause a more rapid growth in the equivalent width (see Fig. 2.4.d). Eq. (2.11) can be written as

  $$\frac{W_\lambda}{\lambda} = \sqrt{\frac{e^2 \lambda \gamma}{m c^3}} \sqrt{N f_{lu} \lambda} \,. \tag{2.22}$$

  When the damping sets in depends on the damping constant γ, which is different for each transition.

Knowing this behaviour of the equivalent width as a function of $(N f_{lu} \lambda)$, the curve of growth provides as a basic and excellent tool to determine the amount of various absorbing material along a line of sight (see Chapter 4 for this sort of analysis).

2.4 H I 21-cm emission

The most abundant interstellar element, H I, is best detected through its emission at 21 cm, in the radio spectral range. This emission is the result of the change in the spin of the electron relative to the proton spin. When the spin flips from parallel to anti-parallel, a photon is emitted with an energy corresponding to $\lambda \approx 21$ cm.

2.4.1 Brightness temperature

In radio astronomy one speaks of the radiation in terms of brightness temperature T_B [K] (instead of flux or intensity). This is the temperature a hypothetical blackbody needs to have to emit the observed amount of continuum radiation at λ_{obs}

$$T_B = \frac{\lambda_{\mathrm{obs}}^2 \, S}{2 \, k \, \Omega} \,. \tag{2.23}$$

Here S is the flux density in [Jy/beam], k the Boltzmann constant, and Ω the beam solid angle of the telescope. Note that T_B is not the kinetic temperature, but a measure for the observed radiation, and widely used in radio astronomy, also when the source is not a black body.

2.4.2 Column density

In H I 21-cm observations, the column density of the observed neutral hydrogen gas, $N(\mathrm{H\,I})$ in cm^{-2}, can be obtained directly by integrating the flux (given as T_B) over the spectral emission line, under the assumption that the gas is optically thin ($\tau \ll 1$)

$$N(\mathrm{HI}) = 1.823 \times 10^{18} \int T_B \, \mathrm{d}v \,, \tag{2.24}$$

with T_B being the brightness temperature in K, and $\mathrm{d}v$ being the velocity range in $\mathrm{km\,s^{-1}}$, over which T_B is integrated. For a full derivation, see e.g., de Boer (2006).

2.4.3 Upper temperature limit

Because of the long life time (i.e., small damping constant) of the 21-cm transition, the emission line profile has a width dominated by the one of the Doppler function (recalling Sect. 2.2.3). Thus, using the Maxwellian distribution, one can derive an upper limit for the kinetic temperature, T_{max} [K], of the gas from the width of the H I emission line

$$T_{\mathrm{max}} = \frac{m_{\mathrm{H}} \, \Delta v^2_{\mathrm{FWHM}}}{8 \, k \, \ln 2} \approx 21.8 \times \Delta v^2_{\mathrm{FWHM}} \,, \tag{2.25}$$

where v_{FWHM} [$\mathrm{km\,s^{-1}}$] is the FWHM of the H I line, m_{H} the mass of the hydrogen atom, and k the Boltzmann constant. The kinetic temperature derived in this way serves as an upper limit, because the broadening of the emission line is not only produced by thermal, but also turbulent motions in the gas (see Sect. 2.2.4).

2.5 Abundances and ionisation balance

The amount of elements heavier than hydrogen and helium, relative to the amount of H I in an object, is expressed as the metal abundance, or the metallicity of the object. As the result of constant chemical enrichment of the interstellar medium by stars and supernova explosions, and the usage of the interstellar material in formation of the next generation of stars, the metal abundances give clues on the age and the enrichment mechanism of the objects, and indicate how much they have participated in this global chain process. The amount of an element relative to the amount of H I, is therefore expressed in comparison to the element abundances in the Sun. The gas in the solar vicinity for example, is expected to have approximately a solar metallicity. It is common to express the abundances of the elements in terms of relative abundances. The relative abundance [X/H], of a certain element X, is expressed as

$$[\mathrm{X/H}] = \log\left(\frac{N(\mathrm{X})}{N(\mathrm{H})}\right) - \log\left(\frac{N(\mathrm{X})}{N(\mathrm{H})}\right)_{\odot} , \tag{2.26}$$

where N is the column density in cm^{-2}, and X the sum of all ionisation stages of the element.

For solar metallicity the term [X/H] is by definition, zero. In reality however, abundances differ from solar for various reasons. When studying the interstellar gas, even of solar origin, an underabundance is often observed, in particular for some elements, such as Fe, Si, Ca. The main reason for the observed underabundance is that these elements are depleted and bound into dust grains, hence a fraction of them can not be observed in absorption. Furthermore, when deriving the relative abundances, we often have information on the elements in certain ionisation stages, that might not be the dominant ionisation stage of that element in the intervening gas. A partial ionisation of the hydrogen may also affect the derived ratios for relative abundances. Thus, the derived relative abundances do not only reflect the metallicity, but also the depletion factor, and the ionisation structure of the gas.

Although in neutral gas most of the hydrogen gas is in neutral form, other elements can exist in neighbouring ionisation states, the relative proportions of which are set by the ionisation and recombination conditions in the gas. In more extreme conditions, where the gas is exposed to a strong radiation field, most of the hydrogen gas may be ionised, and the gas is referred to as ionised gas, or H II region. Below, the relevant processes are described (see e.g., de Boer (2006) for more detailed descriptions).

The total ionisation rate Γ_{total} can be expressed in terms of

$$\Gamma_{\mathrm{total}} = \Gamma_{\mathrm{phot.ion}} + \Gamma_{\mathrm{coll.ion}} + \Gamma_{\mathrm{ch.exch.}} , \tag{2.27}$$

where the dominant factor is $\Gamma_{\mathrm{phot.ion}}$ due to the ambient radiation field, either being the average interstellar radiation field, or a nearby radiation source such as a star. $\Gamma_{\mathrm{coll.ion}}$ is the ionisation rate by collisions, effective in hot or highly dense regions, and $\Gamma_{\mathrm{ch.exch.}}$ the ionisation rate by charge exchange between particles during an encounter.

Ionisation of a particle may eventually be followed by the reversed process, either by the ion catching the electron in a collision and becoming a neutral atom again (radiative recombination, α_{rad}) or involving two electrons where the atom gets excited and the colliding electron will occupy the state of the excited electron (di-electric recombination, α_{diel}), or through charge exchange of particles (charge exchange recombination, $\alpha_{\mathrm{ch.exch.}}$). Thus, the total recombination rate depends on the electron density n_e and the temperature of the gas, and can be expressed in terms of the above mentioned recombination mechanisms

$$[\alpha(T)\, n_e]_{\mathrm{total}} = (\alpha_{\mathrm{rad}} + \alpha_{\mathrm{diel}})\, n_e + \alpha_{\mathrm{ch.exch.}}\, n_x , \tag{2.28}$$

where n_x is the number density of the particles involved in charge exchange reactions. This term is however, normally negligible compared to $(\alpha_{\mathrm{rad}} + \alpha_{\mathrm{diel}})\, n_e$.

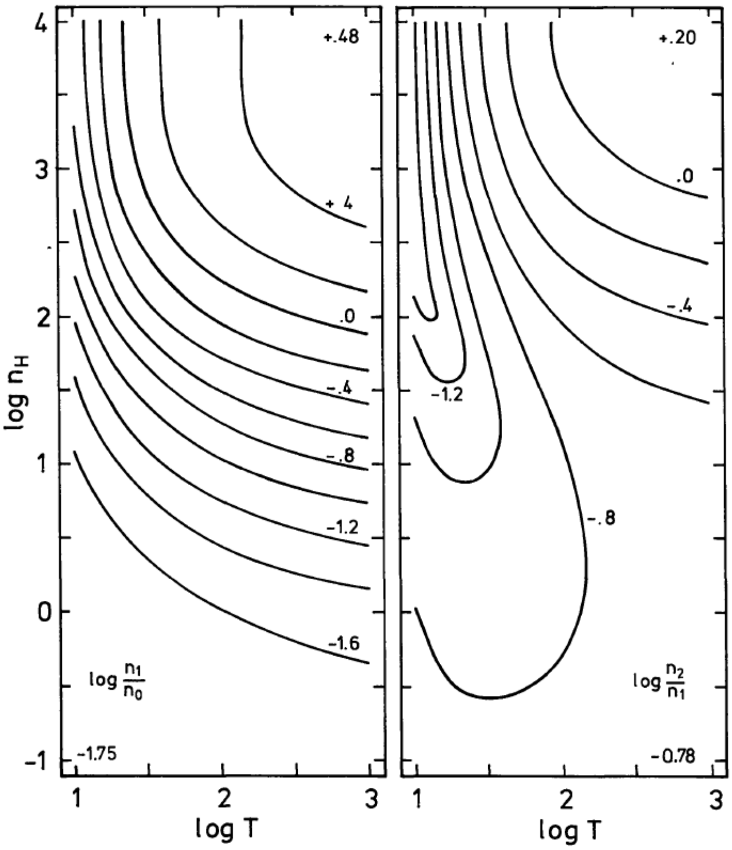

Figure 2.5: The ratios of the population density, log $\frac{n_1}{n_0}$ and log $\frac{n_2}{n_1}$ (the subscripts), of the fine-structure levels of C I are plotted as a logarithmic function of density $n_{\rm H}$ and temperature T. n_0, n_1, and n_2 are the population density of the states $^3P_0$, $^3P_1$, and $^3P_2$ respectively. The value on the top right corner indicates the statistical limit, and the one on the bottom (one on left, other on right) corner the radiative limit. Figure from de Boer & Morton (1974).

The relative particle density in neutral and ionised form, $n_{\rm atom}$ and $n_{\rm ion}$ can then be expressed according to a balance between the ionisation and the recombination rates

$$\frac{n_{\rm ion}}{n_{\rm atom}} = \frac{\Gamma_{\rm total}}{[\alpha(T)\, n_e]_{\rm total}} . \tag{2.29}$$

On a line of sight, one normally assumes that this is directly related to $N_{\rm ion}/N_{\rm atom}$, an assumption which likely is valid for the denser regions dominated by absorption.

2.6 C I fine-structure excitation, and neutral gas parameters

In neutral gas, the atoms and ions are in the ground state. Some of these are split into fine-structure levels, the population of which is reflected by the density and temperature of the gas. Here the example of Carbon is described (see also de Boer (2006) for other examples), which has been used in interpreting the interstellar gas properties, as mentioned in the previous Chapter.

The ground state of C I is split into three states: $^3P_0$, $^3P_1$, and $^3P_2$, denoting the fine-structure levels C I, C I*, and C I** respectively. Different processes can be responsible in populating these states (see e.g., de Boer & Morton (1974) for a review of all these processes.). The main mechanisms however, are collisional excitation and UV-pumping. Collisions by hydrogen atoms is the dominant population mechanism (except at low densities), leading to direct excitation to the upper levels. A collision cross-section is calculated by Bahcall & Wolf (1968) for each transition. Collisions by other particles are negligible, except maybe for H_2. The second process, the UV-pumping, becomes more important at low densities (the dominant excitation mechanism at $n_\mathrm{H} < 10\,\mathrm{cm}^{-3}$, de Boer & Morton 1974), and depends on the ambient UV-radiation field. As the excitation of the atom follows by a decay to one of the fine-structure levels of the ground state, the full excitation balance between the levels must be considered for understanding of the local gas conditions. A full excitation state calculation is shown in form of a diagram by de Boer & Morton (1974), here in Fig. 2.5. There, the relative populations of the fine-structure levels are expressed as a function of density and temperature, based on a balance between all mentioned processes.

Chapter 3

The physics of molecular hydrogen

The physical properties of molecular hydrogen play a very important role for many interpretations and conclusions in this work. Thus, in this Chapter I review the structure of the H_2 molecule, the H_2 absorption line spectrum, and the processes and conditions for formation and dissociation of this molecule. All these aspects are relevant for the derivation of information about the properties of the gas in which H_2 is present.

3.1 Observing the interstellar H_2, and its importance

Molecular hydrogen is the most abundant and ubiquitous molecule in the neutral ISM. Yet, it is not easily observed. Because H_2 is a symmetric molecule and has no permanent dipole moment it does not emit radiation, unless it is located in an energetic environment where it can be excited in vibrational states, and become visible by the decay through spectral lines in the near-IR part of the spectrum. At low temperatures however, the only efficient way to detect H_2 is through absorption-line spectroscopy in the FUV. As the FUV and UV part of the spectrum are blocked by the Earth's atmosphere, the detection of H_2 absorption became possible only with the launch of UV-sensitive detectors above the atmosphere in the early 70s. The first detection of H_2 in absorption was reported by Carruthers (1970) towards ξ Persei with a rocket-borne UV-spectrometer. The H_2 absorption-line studies soon advanced by the launch of the COPERNICUS satellite and the presentation of first results by Spitzer et al. (1973). More satellites, with higher velocity resolution soon followed, among which is the latest FUV spectrograph, FUSE, which had enormous success.

Provided that there are appropriate background sources, FUV absorption-line spectroscopy serves as a very sensitive method in detecting H_2, down to $N(\mathrm{H}_2) \approx 10^{14}$ cm^{-2} (the detection limit, depending on the instrument), in regions where the average gas column densities are relatively low[1]. The studies in the last decade have shown the ubiquity of molecular hydrogen in the Milky Way in different directions of the sky (Shull et al. 2000; Richter et al. 2003b; Jenkins et al. 2003; Gillmon et al. 2006). Latest studies have

---

[1] For $N(\mathrm{H}_2) > 10^{21}$ cm^{-2} absorption-line studies become difficult due to dust extinguishing the FUV light, an effect proportional to the amount of H_2.

further shown that H_2 can also exist in more puzzling conditions, like in Galactic halo IVCs (Gringel et al. 2000; Richter et al. 2001; Bluhm et al. 2001; Richter et al. 2003a,b), and HVCs (Richter et al. 1999; Richter et al. 2001; Sembach et al. 2001). For a review see Richter & de Boer (2004).

Being the most abundant molecule makes the interstellar H_2 a popular subject of study. It is however, the link to the conditions in which it can form and survive that makes its detection most desirable. It is therefore important to understand the physical properties connected with the presence of this molecule to understand the gas within which it resides.

3.2 The structure of H_2: excitation, rotation, and vibration

The electronic states of H_2 are denoted Σ, Π, and Δ, with the total electron angular momentum, Λ, of $0\hbar$, $1\hbar$, and $2\hbar$, projected on the unit vector along the nuclear axis, k (i.e., Σ with the angular momentum of $0\hbar$ being the ground electronic states). The ground electronic state is described as $X^1\Sigma_g^+$. The notation X is for ground state singlet (excited electronic states are labelled alphabetically, with capital letters for singlet, and lower case letters for triplet states). The superscript 1 reflects the orientation of the total spin angular momentum, $2S + 1 = 1$, i.e., the total spin of the electrons $S = 0$. In electronic ground state, only this configuration with anti-parallel electron spins is stable. The subscript g (or u) stand for the even (or odd) symmetry of the electron wave function, and the superscript $+$ (or $-$) for even (or odd) symmetry of the electron spin state. Singlet-triplet transitions are forbidden, and the first allowed electronic transitions for H_2 are: $X^1\Sigma_g^+ \rightarrow B^1\Sigma_u^+$ (Lyman bands), and $X^1\Sigma_g^+ \rightarrow C^1\Pi_u$ (Werner bands), with energies from 11 to 14 eV.

Each electronic state of H_2 is split by a set of vibration and rotation levels. Fig. 3.1 shows the potential energy curves of the electronic ground and excited states of H_2. There are 14 bound vibrational levels in ground electronic state, described by the quantum number v, where the vibrational level $v = 14$ correspond to the dissociation energy at ≈ 4.5 eV for the molecule in ground state. Excitation to higher vibrational level leads, therefore to dissociation. For each vibrational level, a set of rotational states are possible (up to the dissociation energy), given by the quantum number J. As the molecule rotates around its axis, its angular momenta combine in ways which for the lowest state are described by Hund's case b coupling. The nuclear rotation R, and the electronic angular momentum Λk combine into a vector N. J is the resulting total angular momentum formed by the vector N and the total spin of the electrons S (note that $N = J$ for ground electronic state).

According to Pauli's principle, only one combination of nuclear spins is possible for each rotational level in a certain electronic state. This leads to two distinct states for the hydrogen molecule: a) The para-H_2 with anti-parallel proton spins, i.e., the total nuclear spin $I = 0$. The spin wavefunction is antisymmetric, and consequently the nuclear wavefunction is symmetric. Thus, only rotational states with even J numbers are possible, i.e., $J = 0, 2, 4, \mathrm{etc.}$ b) The ortho-H_2 with parallel proton spins, i.e., total nuclear spin

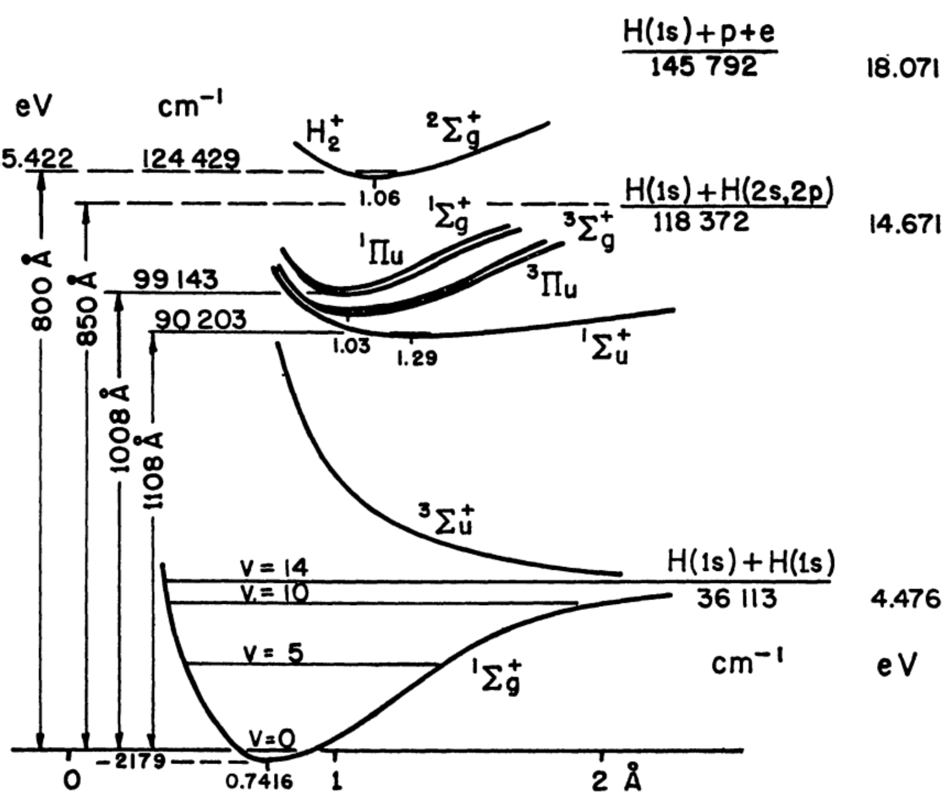

Figure 3.1: Potential energy curves of the ground state and lower excited states of H_2. The horizontal lines inside the potential indicate the vibrational energy levels $v = 0$ to 14 of the ground state, up to the dissociation energy of 4.476 eV. The transitions upwards to $^1\Sigma_u^+$, with all the rotational vibrational levels, involve the Lyman band, and the ones to $^1\Pi_u$, the Werner band. The excitation wavelengths are indicated, as well as the energies for photodissociation and photoionisation. Figure from Field et al. (1966).

$I = 1$. Here the spin wavefunction is symmetric, so the nuclear wavefunction must be antisymmetric, and rotational states with odd J numbers are possible, i.e., $J = 1, 3, 5,$ etc.

When comparing the relative population of even and odd J levels (see the next Section), it is important to consider the different statistical weights of these levels. The statistical weight for a level J is given by $(2I + 1)(2J + 1)$, where $(2I + 1) = 3$ for ortho-H_2 (odd J) with aligned nuclear spin, and 1 for para-H_2 (even J) with anti-aligned nuclear spin.

Transitions with $\Delta J = +2, +1, 0, -1, -2$ are traditionally called O-, P-, Q-, R-, or S-transitions. These are labelled as $(v' - v'')$O(J''), $(v' - v'')$P(J''), etc, with the superscripts $'$ and $''$ referring to the upper and lower levels, respectively. The transition (1-0)R(1) for example, also written as R(1)1-0, indicate transition from $J = 2$ to 1, with a change in vibrational state, v, from 1 to 0.

H_2 is homopolar, i.e., it has no permanent dipole moment in its electronic ground

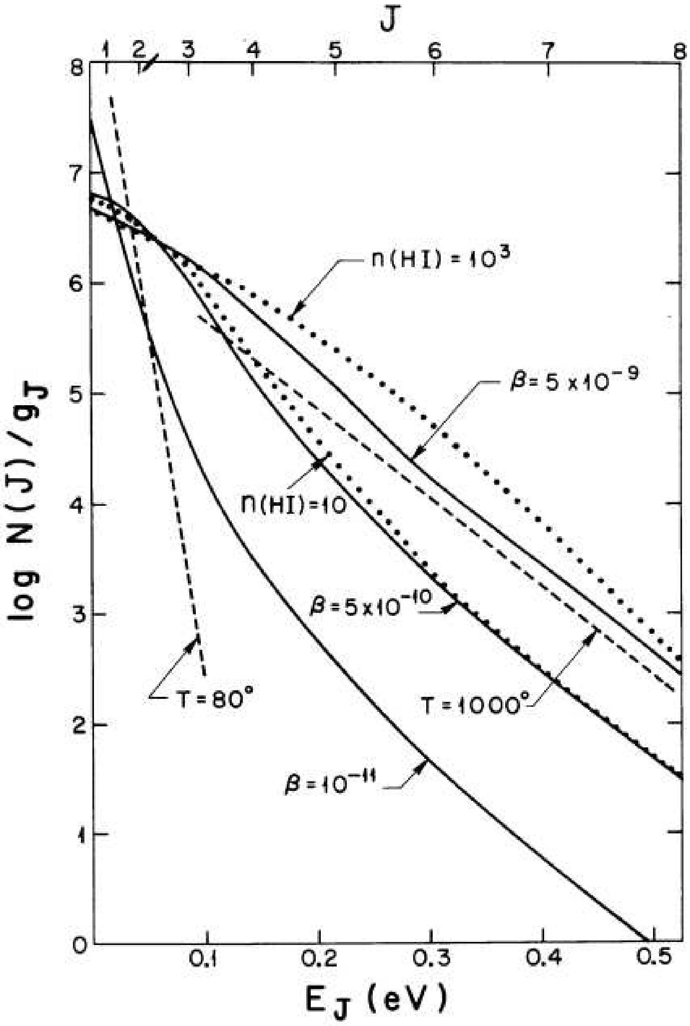

Figure 3.2: Theoretical population densities of rotational levels for H_2. Computed particle density n_J of H_2 in level J (values of J shown at the top) divided by the statistical weight g_J, are plotted on a logarithmic scale against the excitation energy E_J. The two dashed lines represent Boltzmann distribution at $T = 80$ and 1000 K. The solid lines are the theoretical curves for $T = 80$ K for a gas of density $n(\mathrm{H\,I}) = 10$ cm^{-3}, and for three different β, the probability, per second, of photoabsorption. The dotted lines are the theoretical curves for hypothetical cloud at $T = 1000$ K and $\beta = 5 \times 10^{-10}$ s^{-1}, but for two different values of $n(\mathrm{H\,I})$. Figure from Spitzer & Zweibel (1974).

state. Thus, dipole transitions $\Delta J = \pm 1$ within the ground state are forbidden. Only quadrapole transitions are allowed, which have their wavelengths in the near infrared part of the spectrum. When excitation to higher electronic states are additionally involved, $\Delta J = \pm 1$ is possible. These transitions include Lyman and Werner bands (mentioned above), and occur in the FUV part of the spectrum. Thus, Ly R(1)1-0 for example, is a transition from $X^1\Sigma_g^+$, $J = 2$, $v = 1$, to $B^1\Sigma_u^+$, $J = 1$, $v = 0$.

Detailed descriptions of the physical structure of H_2, and its role in astrophysics can be found in reviews by Field et al. (1966) and Shull & Beckwith (1982).

3.2.1 Boltzmann temperature

The lower rotational levels of H_2 are mostly populated through collisions. Consequently, the relative level population can be described by the Boltzmann law

$$\frac{N_{J+1}}{N_J} = \frac{g_{J+1}}{g_J} \cdot e^{-(E_{J+1}-E_J)/(kT_\mathrm{B})}\,, \tag{3.1}$$

where N_J and N_{J+1} are the column densities of H_2 in the lower J level (normally $J = 0$, when considering collisionally excited levels), and the upper $J+1$ level (normally $J = 1$ or 2) respectively, and g_J and g_{J+1} the corresponding statistical weights for those levels. As explained in the previous Section, $g = (2J+1)$ for even J numbers, and $g = 3\,(2J+1)$ for odd J numbers. k is the Boltzmann constant, and T_B the Boltzmann temperature.

The higher J-levels, on the other hand, are normally excited by photons from the ambient UV-radiation field through UV-pumping (Spitzer & Zweibel 1974), or by the UV photons emitted in the molecular formation. The population of these higher levels can also be described by the Boltzmann distribution above (Eq. (3.1)), for which T_B does not represent the kinetic temperature, but an "equivalent UV-pumping temperature", $T_{\mathrm{UV-pump}}$.

Fig. 3.2 shows how population densities of rotational levels change with β, the probability per second of photon absorption in the Lyman and Werner bands, for different neutral gas densities, $n(\mathrm{H\,I})$ (Spitzer & Zweibel 1974). β depends directly on the strength of the ambient UV radiation field and is consequently lower for increased molecular self-shielding. If β is smaller than the mean Galactic value of $\beta = 5 \times 10^{-10}$ s^{-1} due to shielding, the population densities of lower J-levels drop steeper for increased E_J compared to the higher J-levels ($J > 2$). The slope of the curves can be used to estimate the excitation temperature: the steeper the slope, the lower the corresponding Boltzmann temperature. The computed equilibrium populations of the H_2 rotational levels by Spitzer & Zweibel (1974) further show that the reduced β result in lower $T_{\mathrm{UV-pump}}$ of 200 to 400 K for a cloud at the kinetic temperature $T = 80$ K and $n(\mathrm{H\,I}) \leq 10^2$ cm^{-3}. This is in the range of $T_{\mathrm{UV-pump}}$ observed for the interstellar clouds. Note that the case of $T = 1000$ K is not of relevance here, as it pertains to either hot gas, or gas that is exposed to strong UV radiation by being located very close to the radiation source.

3.3 Formation and dissociation of H_2

Although the molecular hydrogen is the most abundant molecule in the universe, the formation and maintenance of it in the interstellar medium is not a straightforward process. The probability for a hydrogen atom to form a molecule through collisions with other hydrogen atoms is, under typical ISM conditions, less than 3×10^{-11} over the entire lifetime of the Galaxy (Field et al. 1966). Thus, H_2 formation through $\mathrm{H} + \mathrm{H} \rightarrow H_2 + h\,\nu$, is extremely inefficient. This is because the formation energy of $\geq 4.5\,\mathrm{eV}$ can not be released through emission, because the dipole transitions in the ground state are not allowed and will therefore in most cases lead to immediate dissociation of the newly formed molecule.

The most efficient process for H_2 formation takes place on the surface of dust grains. This process was first pointed out by van de Hulst (1948). If the H atom comes into contact with a grain of low temperature, it may stick to it, or move around over its surface long enough to meet and collide with another H atom and form H_2. The formation energy is then partly released into the grain, and partly into ejecting the molecule from the grain. It may also lead to the excitation of the newly formed molecule. The frequency of H_2 formation in this way depends on the collisional rate between the hydrogen atoms and the grains, and the probability that the atoms stick to the dust grain for a time long enough to collide with another atom. These parameters depend on the volume density of the atoms, and the temperature of the dust grain. Thus, the rate for H_2 formation on the surface of dust grains is given by

$$\left(\frac{\mathrm{d}n(\mathrm{H_2})}{\mathrm{d}t}\right) = R\, n_\mathrm{H}\, n(\mathrm{HI})\,, \tag{3.2}$$

where R is the formation rate coefficient giving the probability rate per hydrogen atom to form molecules by collisions with dust grains, n_H is the volume density of total hydrogen $n_\mathrm{H} = n(\mathrm{H\,I}) + 2n(\mathrm{H_2})$, with $n(\mathrm{H\,I})$ as the volume density of H I, and $n(\mathrm{H_2})$ as the volume density of H_2. Direct calculation of R is difficult, as the exact composition and structure of dust grains are unknown. However, empirical values derived indicate the mean value of $R \approx 3 \times 10^{-17}\ \mathrm{cm^3\,s^{-1}}$ (Jura 1974, 1975; Spitzer 1978).

Molecular hydrogen in interstellar space can be destroyed by radiative and/or collisional dissociation. UV photons are the main source of dissociation of molecular hydrogen at typical neutral gas temperatures. Direct dissociation by $X^1\Sigma_g^+ \rightarrow b^3\Sigma_u^+$ is, however, a singlet-triplet transition, thus forbidden. Instead, the absorbed photon is mostly leading to excitation to the first allowed electronic states $B^1\Sigma_u^+$ (Lyman bands) or $C^1\Pi_u$ (Werner bands), followed by a spontaneous decay to a vibrational level $v \geq 14$ in electronic ground state, which leads to the dissociation of the H_2 molecule. The total probability, per second, for a molecule in certain rotational state of the ground electronic and vibrational state to get dissociated in this way is given by R_ph. Consequently, H_2 is destructed through photodissociation with a rate of

$$R_\mathrm{ph}\, n(\mathrm{H_2}) = \langle k \rangle\, \beta\, n(\mathrm{H_2})\,, \tag{3.3}$$

where $\langle k \rangle$ gives the probability that the molecule is dissociated after photoabsorption, and β is the photoabsorption rate (Sect. 3.2.1), summed over all Lyman and Werner bands. Outside a cloud in the local disc environment, this probability is referred to as β_0, and has the mean value of $\beta_0 = 5.0 \times 10^{-10}\ \mathrm{s^{-1}}$ (Spitzer 1978). Spitzer (1978) computed $\langle k \rangle = 0.11$ averaged over the Werner and Lyman bands.

In diffuse clouds and in a H_2 formation-dissociation equilibrium, we have

$$\langle k \rangle\, \beta\, n(\mathrm{H_2}) = R\, n_\mathrm{H}\, n(\mathrm{HI})\,, \tag{3.4}$$

based on which we can derive the relation between volume densities $n(\mathrm{H\,I})$ and $n(\mathrm{H_2})$

$$\frac{n(\mathrm{H\,I})}{n(\mathrm{H_2})} = \frac{\langle k \rangle\, \beta}{R\, n_\mathrm{H}}\,. \tag{3.5}$$

Observations have shown that the fraction of hydrogen in molecular form increases rapidly with the increasing thickness of the cloud. This is due to the H_2 line self-shielding. When the column density of H I and H_2 increases and exceeds a critical level, the UV radiation can not easily penetrate through. Thus, an outer layer is formed in which the Lyman lines are absorbed, and the dissociation rate for the inner parts of the cloud decreases significantly. Sufficient self-shielding from the radiation field is therefore very important for keeping the molecules from being dissociated. As a result, the interstellar molecular hydrogen is found in the inner parts of the clouds, surrounded by outer atomic regions (Federman et al. 1979). The H_2 line self-shielding is further discussed in Chapter 5 and Chapter 6. For a more extensive description of the formation and dissociation balance of H_2 in the interstellar medium, see e.g., Spitzer (1978), and Draine (2011).

Chapter 4

On the data and analysing methods

This Chapter presents the different data sets used for the analysis in the coming Chapters. It also gives a brief introduction to the instruments from which the data has been obtained, and the information that is relevant for understanding the properties of the data. Different methods have been used in analysing the various data sets to obtain the necessary information such as the column density and the Doppler broadening of the gas seen in the absorption lines. These methods are described in this Chapter.

4.1 The spectral data

An important aspect in the spectroscopic technique is the so-called resolution of an instrument, which plays a crucial role in choosing the methods for data analysis. Therefore, this definition is explained below, before describing the data used in this work.

Spectral resolution

As described in Chapter 2, an absorption line has the shape of a Voigt profile, carrying the information on the Doppler broadening and the column densities of the absorbers. What we observe, however, is not the true line profile, but a convolution of the line profile and the instrumental response, which depends on the resolving power of the spectrograph with its detector, expressed in R (sometimes wrongly referred to as the “resolution”)

$$R = \frac{\lambda}{\Delta\lambda}\,, \tag{4.1}$$

where $\Delta\lambda$ is the instrumental resolution, which is the FWHM of the instrumental profile width in wavelength, assuming a Gaussian profile function. This is the smallest separation in wavelength that can be resolved by the spectrograph at a certain wavelength λ.

While high spectral resolution ($R > 20,000$) is often preferred in order to be able to separate and analyse the many overlapping interstellar absorption components of small Doppler parameters in the spectra, the access to high-resolution spectrographs is limited. In particular, in the range of FUV, where satellites are required (as these wavelengths are blocked by the Earth's atmosphere), the design and cost limitations today mainly offer intermediate-resolution spectrographs.

Below, the different data sets analysed in this work are presented. These have been analysed differently, mainly because of the different resolution of the instruments used. All spectra used in this work were retrieved as pre-reduced data.

4.1.1 Stellar FUV and UV spectra from Fuse and Stis

To be able to observe in far-ultraviolet and ultraviolet spectral range, one needs to advance into space, because these wavelengths are blocked by Earth's atmosphere. As one of the modern UV-satellites, the Far Ultraviolet Spectroscopic Explorer (Fuse) was launched in 1999, and operated until 2007, collecting a large amount of data, including observations of 187 hot stars in the Large Magellanic Cloud (LMC), and 100 hot stars in the Small Magellanic Cloud (SMC).

The Fuse spectral data covers the wavelength range 905-1187 Å with a resolving power of $R = \lambda/\Delta\lambda \sim$ 15,000-20,000, corresponding to a resolution of about 15 to 20 $\mathrm{km\,s^{-1}}$ (FWHM). This wavelength coverage enables the detection of absorption by many important atomic and ionised species, and by molecular hydrogen, which makes this instrument most suitable for our purpose of studying and comparing the physical properties of the disc and halo gas along different lines of sight.

The Fuse instrument consists of four co-aligned prime-focus telescopes and Rowland spectrographs with two microchannel plate detectors. To gain optimum reflectivity, two of the telescope channels are equipped with SiC coatings with maximum efficiency in the wavelength range of 905-1100 Å, and the two others with Al+LiF coatings operating in the wavelength range of 1000-1187 Å. Each detector is divided into two segments, A and B. Observations are able through four apertures: the standard LWRS aperture ($30'' \times 30''$), the MDRS aperture ($4'' \times 20''$), the HIRS aperture ($1\overset{''}{.}25 \times 20''$), and PINH aperture ($0\overset{''}{.}5$ diameter) which was never used for observations. Most of the observations are done in LWRS aperture, with some exceptions, including two of the sightlines discussed in this work: Sk -67°107 and Sk -67°106, which were observed using the MDRS aperture.

For detailed information about the Fuse instrument and observations see Moos et al. (2000) and Sahnow et al. (2000).

The Space Telescope Imaging Spectrograph (Stis) on board the Hubble Space Telescope (HST) provides a resolving power of $R = \lambda/\Delta\lambda \sim$ 30,000-110,000, corresponding to a spectral resolution of $\sim 7\,\mathrm{km\,s^{-1}}$ (FWHM) for the wavelength band between 1150 and 1730 Å. The Stis spectral data covers the wavelength range longward of the Fuse spectrum, enabling the detection of other species such as neutral carbon, as well as additional absorption lines by the atomic and ionised species covered by Fuse.

For detailed information about the Stis instrument see Woodgate et al. (1998); Kimble et al. (1998); Bostroem et al. (2010).

Table 4.1: Information about the FUSE data as retrieved from the MAST archive, and additional STIS data.

Star	RA[a] (J2000)	Dec[a] (J2000)	Spectral[a] type	V [mag]	date	programme	exp.time[b] [ks]	aperture
Sk -67°111	05 26 48.00	-67 29 33.0	O6 Iafpe	12.57	2002-03-15	C155	18.45	LWRS
					2002-03-16	C155	15.65	LWRS
					2002-03-17	C155	21.83	LWRS
					2002-03-18	C155	13.43	LWRS
					2002-03-19	C155	18.23	LWRS
					2002-03-20	C155	17.78	LWRS
LH 54-425	05 26 24.25	-67 30 17.2	O3IIIf+O5	13.08	2006-05-20	F321	18.92	LWRS
					2006-05-21	F321	15.45	LWRS
					2006-05-22	F321	22.29	LWRS
					2006-05-23	F321	8.65	LWRS
Sk -67°107	05 26 24.00	-67 30 00.0	B0	12.50	2000-02-09	A111	11.18	MDRS
					1998-11-14	GO7299 O4YN04010	2.3	0″.2×0″.2
Sk -67°106	05 26 13.76	-67 30 15.1	B0	11.78	2000-02-09	A111	11.27	MDRS
					1998-11-06	GO7299 O4YN03010	2.3	0″.2×0″.2
Sk -67°104	05 26 04.00	-67 29 56.5	O8 I	11.44	1999-12-17	P103	5.09	LWRS
					1998-11-10	GO7299 O4YN02010	2.3	0″.2×0″.2
Sk -67°101	05 25 56.36	-67 30 28.7	O8 II	12.63	1999-12-15	P117	1.26	LWRS
					1999-12-20	P117	6.25	LWRS
					2000-09-29	P117	4.38	LWRS
					1998-11-15	GO7299 O4YN01010	2.3	0″.2×0″.2
					1998-11-15	GO7299 O4YN01020	3.1	0″.2×0″.2

[a] The coordinates and spectral types of the background LMC stars are from Danforth et al. (2002).

[b] Total exposure time for all (co-added) observations made on given date.

The data

Having many bright stars with small angular separation on the sky, the LMC provides an ideal background grid for studying the gas in the disc and the halo of the Milky Way at various spatial scales. There are more than hundred stellar targets in the LMC observed spectroscopically by FUSE, allowing detailed studies of ISM properties based on the many absorptions of a number of neutral and ionised species.

We have chosen the six LMC stars Sk -67°111, LH 54-425, Sk -67°107, Sk -67°106, Sk -67°104, and Sk -67°101, with small angular separations to investigate the structure of the gas in the disc and halo of the Milky Way. The details of the studies will follow in Chapter 5 and Chapter 6. We retrieved the already reduced data from the MAST[1] archive. The data were all reduced with the CALFUSE v3.2.1 pipeline, except for the LH 54-425 and Sk -67°106, which were reduced with CALFUSE v3.2.2. Table 4.1 summarises the information about the retrieved FUSE and STIS data, as well as the properties of the background stars. The final spectral line information were provided in a heliocentric velocity scale. We co-added the calibrated data separately for each of the four co-aligned telescopes, being LiF 1A, LiF 2A, LiF 1B, and LiF 2B. The same is valid for the data from the SiC channel. However from this channel we only have data from one or two of the co-aligned telescopes. Due to the different wavelength zero points in the calibrated data, the spectra of different stars and different cameras might have a shift within $\pm 15\,\mathrm{km\,s^{-1}}$. This shift however is steady for the whole spectral range and does not affect the line identification. The typical signal-to-noise ratio[2] (S/N) of the data varies for the different detector channels and sightlines (see Table 4.2 for more information on the S/N of the FUSE and the STIS data). The data from the SiC channels have in general lower S/N, while the data quality is significantly higher for all the FUSE detectors for the Sk -67°111 and LH 54-425 spectra, because several observations were co-added.

The STIS observations were part of a programme for studying the N 51 D superbubble (Bomans 1997). Only the stars Sk -67°107, Sk -67°106, Sk -67°104, and Sk -67°101 were observed in that programme, using the echelle grating (E140M) and the aperture slit of $0\farcs2\times0\farcs2$. The reduced and calibrated STIS data were provided by Bart Wakker (priv.comm) in heliocentric velocity scale. Some of the absorption lines in the calibrated data suffer from hot pixels, appearing as narrow (one or two pixel wide) emission within the absorptions. These can affect the integrated area over the absorption profile when measuring the equivalent width in the later analysis. We therefore corrected for these hot pixels, by replacing them with a value interpolated over the adjacent pixels. The S/N per resolution element varies over the spectral range and for different lines of sight, the highest S/N $\sim$ 30 (in the spectrum of Sk -67°104, near 1300 Å). Typical values for S/N are presented in Table 4.2 for the region around 1600 Å, considering a range free from absorption.

---

[1] Multi-Mission Archive at Space Telescope: http://archive.stsci.edu/

[2] S/N was derived as the inverse of standard deviation of the noise, for an absorption-free part of the spectrum.

Table 4.2: S/N per resolution element measured within a few Ångström around the listed wavelength, for FUSE and STIS data.

Star	LiF:1A	2A	1B	2B	SiC	STIS
λ[Å]=	1047	1148	1148	1047	980	1605
Sk -67°111	97	74	66	71	55	-
LH 54-425	88	68	60	58	44	-
Sk -67°107	42	41	35	26	17	17
Sk -67°106	62	55	48	30	16	17
Sk -67°104	57	50	42	35	31	21
Sk -67°101	44	52	40	36	20	16

The line of sight towards LMC

The absorption by the interstellar medium on the line of sight towards the LMC is rather complicated, because it contains several gas components. Knowing the absorption lines in the ISM with their transition wavelengths we are able to identify the different elements, and distinguish the different gas components belonging to the disc and halo (intermediate- and high-velocity clouds) through their LSR velocities (see Sect. 1.2). The gas in front of the LMC is known for many years (Savage & de Boer 1979, 1981; Welty et al. 1999). On a line of sight there is gas in the solar vicinity, normally seen around $v_{\rm LSR} \approx 0$ km s^{-1}. Next is the intermediate velocity gas around $v_{\rm LSR} \approx +60$ km s^{-1} on essentially all LMC lines of sight; this gas likely is a foreground intermediate velocity cloud (IVC). Most lines of sight also show the presence of a high-velocity cloud (HVC) at $v_{\rm LSR} \approx +110$ km s^{-1}. Finally, the LMC gas itself shows its presence in the velocity range between +180 and +300 km s^{-1}.

In Chapter 5 and 6, we present the results and discuss the small-scale structures and the properties of the disc and halo gas in the direction of the mentioned LMC stars. The absolute wavelength calibration of the STIS data is much more reliable than for FUSE, therefore we have based the radial velocities of the different gas components towards the LMC, on the STIS data.

4.1.2 QSO optical spectra from KECK HIRES

QSO optical spectra from the KECK HIRES spectrograph, obtained by Prochaska et al. (2007) for abundance measurements on damped Lyman-α systems, are used in Chapter 7 to analyse the IVC and HVC components in various Galactic directions. HIRES is an echelle spectrograph mounted on the KECK 10-m telescope on Hawaii, providing a resolving power of $R = \lambda/\Delta\lambda \sim$ 25,000-85,000, with $R = 45,000$ at ~ 6000 Å (FWHM ~ 6.7 km s^{-1}).

The original sample included 42 pre-reduced and normalised QSO spectra (see Prochaska et al. (2007) for details), distributed over almost all Galactic longitudes (with Galactic coordinates in the range of $35.3 \leq l \leq 348.5$, $-79.2 \leq b \leq +75.8$). The HIRES data were first processed with MIDAS in order to convert the measured frequencies into LSR velocities, and to produce the table format needed for the later data analysis with the FITLYMAN tool. Most of these observations, however, turned out not to be useful for the range of Na I and Ca II lines, either because these lines were out of the spectral range (this was mainly the case for the Ca II lines), or the absorption by one or both of the doublets being in the occurred echelle order gaps. Additionally, some of the spectra were not useful because of the very bad data quality. From the original sample only 6 QSOs were suitable for the search of Na I doublets, and only 3 for Ca II[3]. The LSR velocities were used for identifying the Na I and Ca II doublets in the different IVC and HVC components in the 6 lines of sight. The results and analyses are presented in Chapter 7.

4.1.3 HI 21-cm data

Additional H I 21-cm data has been obtained to compare with the spectroscopic data in this thesis. The large H I surveys map the H I content of the Milky Way with the large single-dish radio telescopes, and have typically a detection limit of $N(\text{H I}) > 10^{18}$ cm^{-2}. Below follows a short description on the H I surveys used.

Galactic All Sky Survey (GASS)

The Parkes Galactic All Sky Survey (GASS) (McClure-Griffiths et al. 2009; Kalberla et al. 2010) is a survey of the H I gas in the Milky Way for the entire sky south of $\delta = +1°$. GASS covers LSR velocities in the range of -400 to $+500$ km s^{-1}, at a resolution of 0.82 km s^{-1}. With an angular resolution of 16′, GASS is the most sensitive beam-by-beam sampled survey of Galactic H I in the Southern sky.

The software CASA (Common Astronomy Software Application) was used for analysing the reduced and calibrated data cubes, for extracting the spectra and computing column density maps in the direction of the LMC. CASA is a package of astronomical data reduction tools and tasks, run via the IPython interface to Python, which is suited for post-processing both single-dish and interferometric data. For an extensive description see the CASA reduction cookbook[4].

Effelsberg-Bonn H I Survey (EBHIS)

The Effelsberg-Bonn H I Survey (EBHIS) (Winkel et al. 2010; Kerp et al. 2011) is an ongoing project that fully samples the H I 21-cm data of both the Milky Way and extragalactic sources up to redshifts of $z \sim 0.07$ for the whole northern sky, with the 100-m radio telescope at Effelsberg. The EBHIS has an angular resolution of 9′, and a velocity resolution of 1.25 km s^{-1}, and is the most sensitive fully-sampled survey of the northern sky.

The EBHIS data were used to search for H I 21-cm emission in IVCs and HVCs (see Chapter 7). The reduced and calibrated data cubes (pre-reduced by Benjamin Winkel,

---

[3] All 42 QSO spectra were searched for Ca II independent of Na I. But, the ones with spectra in the range of Ca II absorption were among the QSOs also suitable for Na I absorption-line measurements.

[4] http://casa.nrao.edu/

priv.comm, see also Winkel et al. 2010) were analysed using CASA, for viewing the data in search for IVCs and HVCs, computation of column density maps, and extraction of the spectra.

Leiden-Argentine-Bonn (LAB) survey

The Leiden-Argentine-Bonn (LAB) survey (Kalberla et al. 2005) is an all-sky H I 21-cm survey, combining the Leiden/Dwingeloo survey (LDS) (Hartmann & Burton 1997) of the sky north of $\delta = -30°$, and the Instituto Argentino de Radioastronomía survey (IAR) (Arnal et al. 2000; Bajaja et al. 2005) of the sky south of $\delta = -25°$. The LSR velocity coverage is in the interval of -450 to $+400$ km s^{-1}, at a resolution of 1.3 km s^{-1}. The angular resolution is 35′, lower than the one of the EBHIS. The LAB data were corrected for stray radiation, and merged at the Argelander-Institut für Astronomie in Bonn (Kalberla et al. 2005). The complete H I spectrum for any position on the sky from the LAB survey can be accessed online[5].

We used data from the LAB survey for the sightlines where, up to now, no data from EBHIS was available to search for H I emission in the IVCs and the HVCs (Chapter 7).

4.2 Absorption-line measurements

The absorption data in this work consist of both stellar and QSO spectra from different spectrographs, which have been analysed for different purposes. Furthermore, due to the different properties of the stellar and the QSO spectra, and the differences in the spectral resolutions, different approaches had to be taken into analysing the absorption lines and to gain information on the column densities and the Doppler parameters. The two main methods used, are the CoG-technique, and the Voigt-profile fitting. While the latter method is sufficient for analysing the data with high spectral resolution, the former is required when studying narrow absorption lines with an intrinsic FWHM below the one of the instrument. Table 4.3 and 4.4 list the line parameters used in the absorption-line measurements, for the metal (Table 4.3) and the H_2 absorptions (Table 4.4). The physical background is given in Chapter 2.

4.2.1 Handling of stellar spectra

Continuum normalisation

A stellar spectrum is rather complicated, with a continuum consisting of spectral structures on both local and global scales, some recognised as broad stellar lines and P-Cygni profiles (as mentioned in Sect. 2.1.1). Fig. 4.1 shows part of the FUSE spectra of the LMC stars Sk -67°111, LH 54-425, Sk -67°107, Sk -67°106, Sk -67°104, and Sk -67°101.

---

[5] http://www.astro.uni-bonn.de/~webaiub/english/tools_labsurvey.php

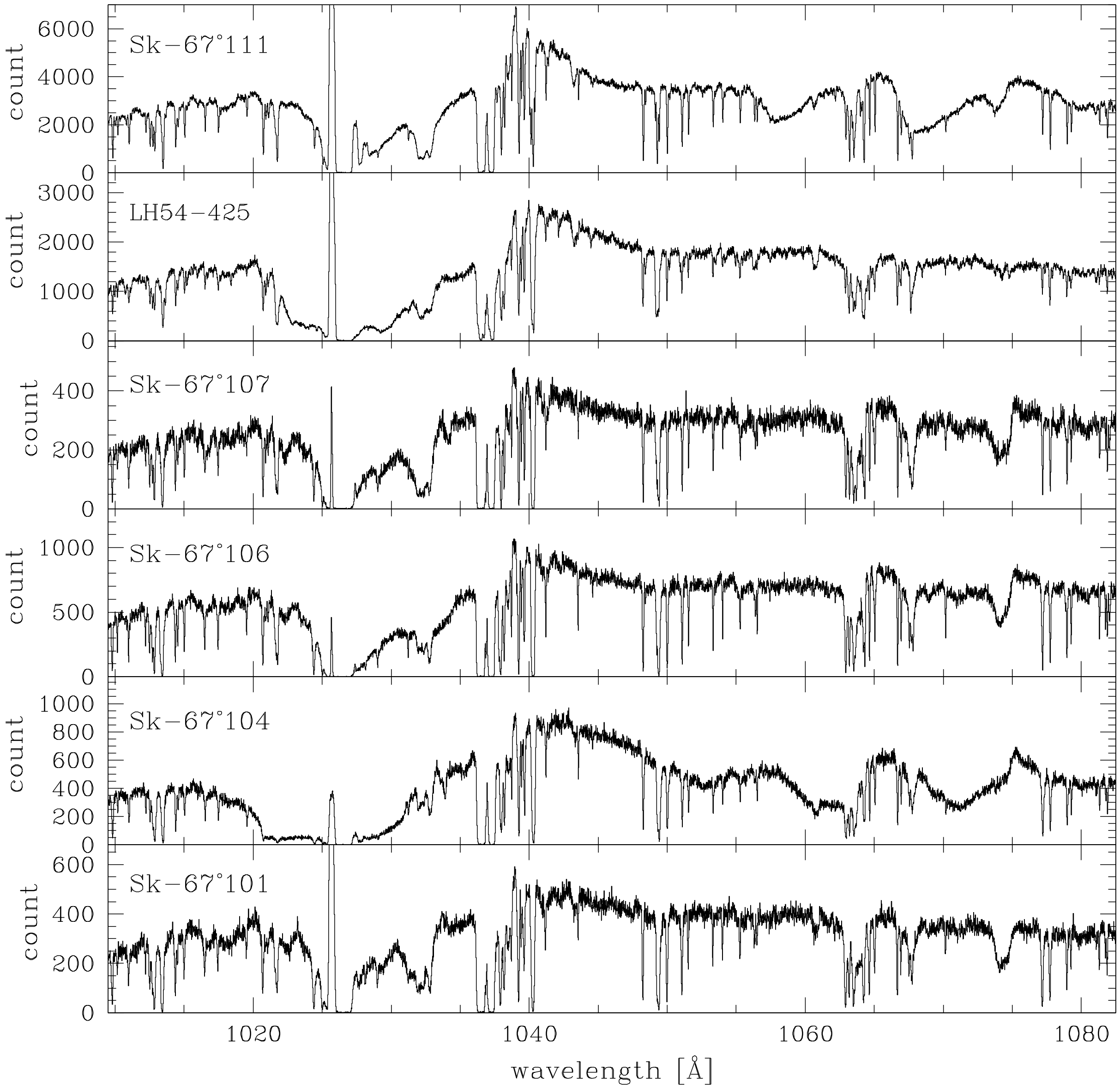

Figure 4.1: Spectra of Sk-67°111, LH 54-425, Sk-67°107, Sk-67°106, Sk-67°104, and Sk-67°101 (from top to bottom), in the wavelength range between 1010 and 1082 Å, observed with FUSE:LiF, segment A. Note the different count levels for the observed spectra, resulting in different S/N (in Table 4.2). The narrow absorption lines are due to the intervening interstellar gas, while the broad structures and the irregular continua are signatures of the individual stars.

The main part of this thesis work is based on analysing the interstellar lines embedded in the complex stellar spectrum. Before analysing the interstellar absorption lines we need to remove the unwanted stellar structures from the spectrum, by choosing an appropriate continuum level. This was done by estimating a continuum level by eye, and normalising the spectra to unity with the programme SPECTRALYZOR. SPECTRALYZOR is a tool developed by Ole Marggraf, which allows the user to define a continuum by interactively placing a sample of points. The Programme then assumes a continuum by linearly interpolating between the given points, based on which it calculates a normalised spectrum (see Marggraf (2004) for details). With this method of normalising the spectrum we eliminated the large scale variations of the continuum as well as the variations on small scales (less than 1 Å). Due to the complex shape of the stellar continuum, this way of choosing the continuum by eye is more reliable than an automatic continuum fitting. Fig. 4.2 shows an example of locally normalised continuum for some of the O I absorption lines in the spectra of the six LMC stars studied in this thesis (in Chapter 5 and Chapter 6). The upper and lower continuum choice are also indicated in that figure. These upper and lower levels have been considered in the error estimate described later in the absorption-line analysis (Sect. 4.2.2). Note that the absorption lines from those parts of the spectra where the continuum placement is highly uncertain were considered with special caution or were excluded from the final analysis.

4.2.2 CoG technique

To get around the resolution problem, one uses the well known approach of the curve of growth (CoG) in order to gain the necessary information (i.e., the amount of absorbing material along a line of sight, and the Doppler broadening) from the observed absorption lines. The theoretical background to this was given in Chapter 2. This method uses the strength of the observed absorption lines (measured as equivalent width) produced by a certain atom or ion, together with the information on the rest-wavelength, λ_0, and oscillator strengths (f-values)[6] for each absorption line to derive the column density and the b-value, simply by comparing this information to a set of theoretical CoGs. As the equivalent width is independent of the resolution of the instrument, this method is extremely useful for studying the narrow interstellar components which can not be resolved by the available instruments.

Equivalent-width measurements

The equivalent width, W_λ, was measured for each absorption line in a normalised spectrum, either by integrating the pixel to pixel area up to the continuum level using a set of MIDAS routines (developed by Philipp Richter), or by interactively fitting single or multiple Gaussian profiles to the absorption lines with the MIDAS package ALICE. For a Gaussian shaped single isolated component of moderate strength, both these methods should result

---

[6] The f-values used were taken from the list of Abgrall et al. (1993a,b) for H_2, and Morton (2003) for other species.

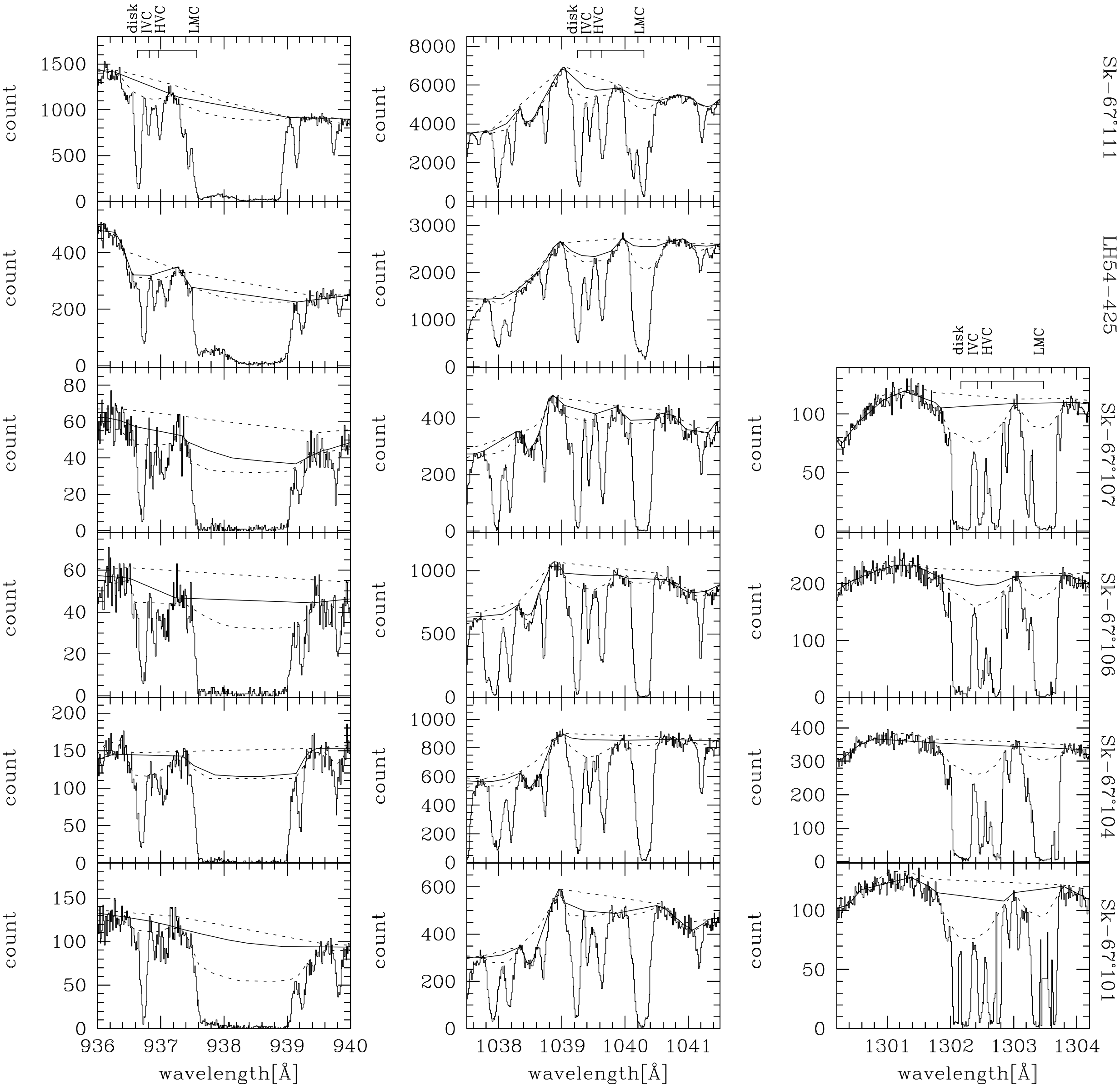

Figure 4.2: O I absorption at 936.63 (from FUSE:SiC), 1039.23 (from FUSE:LiF), and 1302.17 Å (from STIS) and the respective continuum fits are shown for all six stars (names given at right). The solid line is the continuum fit to which the spectrum has been normalised, the dashed lines show the upper and lower continuum choice. The bars at the top mark the known absorption component velocities of the local disc gas, IVC, HVC, and LMC, for the O I absorption.

in the same values for W_λ. For slightly saturated lines, however, the Gaussian fit is not sufficient. We therefore used mainly the former method of integrating the pixel to pixel area, in order to take into account the contributions in the wings of the absorption profile. The slightly blended lines on the other hand, can not simply be measured separately by integrating over the area under the assumed absorption range of a line, and multi-component Gaussian fit is required taking into account all blended components. This was done in the MIDAS ALICE, unless the absorption lines were saturated (e.g., the case for O I absorption described in Sect. 5.2). Note that, unless indicated otherwise, heavily blended lines were not considered in the final analysis

Equivalent width errors

The dominant source of error in equivalent-width measurements is the placement of the continuum. We therefore estimated the errors based on the photon noise and the global shape of the continuum. This was done by manually adopting a highest/lowest continuum within a stretch of few Ångström around each absorption line. The corresponding highest and lowest equivalent widths, $W_{\lambda,\mathrm{max}}$ and $W_{\lambda,\mathrm{min}}$, were then measured, and the error was estimated from $(W_{\lambda,\mathrm{max}} - W_{\lambda,\mathrm{min}})/2$. The minimum errors in this way depend on the local S/N and correspond to the change of the continuum around $\pm 1\sigma$ noise level, meaning for a flat continuum, the upper/lower levels were estimated by placing the continuum $\pm 1\sigma$ above/below the noise level when measuring the $W_{\lambda,\mathrm{max}}$ and $W_{\lambda,\mathrm{min}}$. Fig. 4.2 shows an example of a locally normalised continuum for some of the O I absorption lines, with the upper and lower continuum choice in each case, from which the errors for the O I absorption lines were derived.

Fitting process

The theoretical CoGs were constructed for a range of b-values in the interval of $1\,\mathrm{km\,s^{-1}}$(or $0.5\,\mathrm{km\,s^{-1}}$ for the H_2 absorptions in the IVC, Sect. 6.3), based on the damping constant γ of the strongest considered transition in each species. The chosen damping constant influences the shaped of a produced CoG at large column densities, thus affects the derivation of the N and b for an observed set of absorption lines when some of these absorptions are strong enough to be on the flat to damping part of the CoG. This also has a crucial role in the final error estimate for the derived N and b. Since the various transitions for the same atom and ion can have significantly different damping constants, we used the damping constant of the strongest transition which was used in the CoG-analysis. When more than one strong transition of similar $\log Nf\lambda$-values and significantly different γ were considered on the damping region of the CoG, we produced the CoGs based on an averaged value for γ.

The column density and the b-value for each atom and ion was determined by finding the best representative CoG, with the smallest residual from the observed data (including the errors in W_λ), through a polynomial regression. The errors in N and b were determined by adopting the range of the alternative CoGs (leading to different N and b), for which

68% of the data points had a residual within $1\,\sigma$ from the CoG coefficient. Thus the uncertainties in the column densities were based on the errors in the equivalent-width measurements and the uncertainties in the b-values.

4.2.3 Voigt-profile fitting

Spectrographs with high spectral resolution enable the independent derivation of the column density and the b-value, from Voigt-profile fitting. This task would be straightforward if the instrumental broadening is well known, but that is not always the case. An observed line profile is the convolution of the intrinsic profile with the one of the instrument. Thus, the profile fitting procedure compares a theoretical Voigt profile accounting for the given instrumental resolution, with the observed profile. Typically, the best fitted parameters are derived through a χ^2-minimisation. Below two different line profile fitting programmes are described that have been used in this work.

SPECTRALYZOR

SPECTRALYZOR (Marggraf 2004) provides a semi-interactive option for fitting Voigt profiles to a set of absorption lines, given the transition parameters and the velocity for each absorption, as well as the instrumental resolution. The interactive option of the programme enables the user to overview all the absorptions and their velocity components in a graphic interface. This aspect is very useful when dealing with the many absorptions and blends in the spectra. For this reason, the SPECTRALYZOR was used in this work for identifying the different components of all the species and their blends, and to further judge whether blends of certain elements had a considerable effect on the other absorptions in consideration, given their pre-derived N and b from the CoG-analysis. Thus, this approach was used only as an additional method for the N and b derivations (e.g., in Chapter 5).

FITLYMAN

Part of this thesis is based on analysing the optical high-resolution spectra from KECK HIRES for absorption by Na I and possibly Ca II (Chapter 7). The data were first processed with MIDAS and table formats needed for the data analysis with the FITLYMAN tool were produced.

The software package FITLYMAN (Fontana & Ballester 1995), under ESO MIDAS, is an interactive tool for the fitting of absorption lines in high-resolution normalised spectra. The graphic menu-driven interface allows the user to display the data and specify the lines to be fitted. FITLYMAN also provides the option for fitting the different transitions of the same ion simultaneously. This option was used in measuring the column densities, and the b-values for the Na I and Ca II doublets. The best fit parameters (both N and b) are achieved by searching the best representative theoretical line profile via a χ^2 minimisation procedure on a logarithmic grid. The errors in the resulting N and b were obtained by the default option in FITLYMAN, calculated by inverting the covariance matrix. The resulting errors in this way are symmetric, and do not include the uncertainties due to the noise behaviour or the continuum placement.

See Fontana & Ballester (1995) for more on the error estimates, and the ESO MIDAS help section for more explanations and details on the usage of the FITLYMAN tool.

Comparison with the CoG analysis, and error estimate

As mentioned earlier, FITLYMAN provides a straightforward tool to simultaneously fit one or more absorption lines of the same N and b. The errors provided by this method, however, are only simply representing the goodness of the fit, and do not include the errors in continuum placement or the uncertainties due to the noise behaviour in the spectra. There are furthermore a number of doublets giving b-values below the KECK HIRES instrumental resolution of $\sim 7\ \mathrm{km\,s^{-1}}$, the reliability of which should be highly influenced by the equivalent width errors. Note that if the spectral lines are not resolved the FITLYMAN derives the b-value based on the relative strength of the doublet (or multiplet) lines, equivalent to a CoG fit.

In an attempt to estimate the uncertainties of the measurements, we derived the equivalent width of some of the lines for different S/N and strength, by adopting a continuum about 1σ above and below the chosen continuum. We then estimated the errors, similar to Sect. 4.2.2, from $(W_{\lambda,\mathrm{max}} - W_{\lambda,\mathrm{min}})/2$. These errors were about 10% to 30% of the equivalent widths. By fitting the resulting equivalent widths for each doublet line, including their errors, to the CoG of b assigned by the FITLYMAN, we obtained errors of about 0.05 to 0.3 dex (including the uncertainties in the b-values).

Most of the Na I and Ca II absorption lines were on the linear, or linear-flat transition part of the CoG. While the equivalent width errors only mildly influence the uncertainties in the column densities in this regime, they do have a large effect on the b-value estimate. The small b-values ($b < 7\ \mathrm{km\,s^{-1}}$), given by the FITLYMAN are not excluded, and generally, the low b are also according to the independent measurements with the CoG, possible (although, the two different methods do not provide the same b-value). However, the uncertainties are large, as slight changes in the choice of the continuum for example would result in largely different b-values. Furthermore, some of the absorption lines in our spectra appear too narrow, caused by an irregular noise pattern, which can lead to underestimation of the broadening of the lines. So, in general, the small Doppler parameters of the Na I and Ca II absorbers found should be considered with caution.

4.2.4 Detection limits

Searching for small-scale structure in diffuse interstellar gas includes dealing with weak absorption lines. When dealing with weak lines, it is important to define a significance level, based on which we can distinguish weak absorption lines from noise features. This significance level was assessed in terms of a minimum equivalent width, $W_{\lambda,1\sigma}$, for each individual case, based on the local noise fluctuation and the instrumental resolution

$$W_{\lambda,1\sigma} = 1.066 \times \mathrm{FWHM_{inst}} \times \sigma_{\mathrm{noise}}\,, \tag{4.2}$$

where $\mathrm{FWHM}_{\mathrm{inst}}$ is the instrumental resolution in Ångström defined for the wavelength of the absorption. This is the minimum FWHM of an absorption line. The local σ_{noise} is the standard deviation in the noise around the continuum level, and is inverse to the S/N, $\sigma_{\mathrm{noise}} = \frac{1}{\mathrm{S/N}}$. Simply speaking, the $W_{\lambda,1\sigma}$ derived in this way represent the typical size of a "noise peak" for the considered part of the spectra. In general, features with an equivalent width $\geq W_{\lambda,3\sigma}$ were considered as true absorption lines. Furthermore, we treated only features with FWHMs that were not evidently below the $\mathrm{FWHM}_{\mathrm{inst}}$, the resolution of the corresponding instrument. While a detection significance of 4 or $5\,\sigma$ was generally chosen for the high-resolution data from the Keck HIRES, the limit of $3\,\sigma$ was sufficient for the Fuse data, as from those spectra only features with FWHM $\gtrsim 20$ km s^{-1} were considered, clearly being broader than the statistical noise pattern.

To derive the upper column density limit for an undetected species, an upper equivalent width was estimated, using Eq. (4.2), for the location in the spectrum, where the strongest absorption line of that species is expected to occur. This derived equivalent width was then fitted to the linear regime of the CoG of $b = 1$ km s^{-1} (unless indicated otherwise), to obtain the upper limit for the column density.

Table 4.3: List of transitions, analysed for one or more sightlines[a], the ionisation potential (IP) of the atom/ion, the rest-wavelength (λ_0)[b], f-value[b], and damping constant (γ)[b] of the transition, and the instrument with which the absorption line was detected.

Species	IP [eV]	λ_0 [Å]	f-value [$\times 10^{-3}$]	γ [$\times 10^{9}\,\mathrm{s}^{-1}$]	Instrument
C I	11.3	945.19	152.223	0.379	FUSE:SiC
		1139.79	12.3	0.021	FUSE:LiF
		1157.91	21.2	0.0351	FUSE:LiF
		1158.32	6.55	0.0109	FUSE:LiF
		1276.48	5.89	0.01	STIS
		1280.14	26.3	0.106	STIS
		1328.83	75.7756	0.288	STIS
		1560.31	77.4086	0.127	STIS
		1656.93	149.0	0.36	STIS
C I*		945.338	152.0	1.14	FUSE:SiC
		1279.89	14.3	0.117	STIS
		1560.68	58.1	0.127	STIS
		1656.27	62.1	0.361	STIS
		1657.38	37.1	0.36	STIS
		1657.91	49.4	0.36	STIS
C I**		1139.76	9.54	0.0294	FUSE:LiF
		1329.34	75.8	0.29	STIS
		1657.18	149.0	0.36	STIS
N I	14.5	952.30	2.29000	0.0481	FUSE:SiC
		952.42	1.97000	0.0513	FUSE:SiC
		952.52	0.518	0.0447	FUSE:SiC
		953.42	12.9300	0.219	FUSE:SiC
		953.66	24.6900	0.21	FUSE:SiC
		953.97	33.0700	0.203	FUSE:SiC
		954.10	4.00000	0.141	FUSE:SiC
		963.99	12.4100	0.0855	FUSE:SiC
		1134.17	14.6000	0.151	FUSE:LiF
		1134.41	28.6500	0.149	FUSE:LiF
		1134.98	41.5900	0.144	FUSE:LiF
		1199.55	131.820	0.407	STIS
O I	13.6	922.20	0.245	0.00321	FUSE:SiC
		924.95	1.54500	-	FUSE:SiC
		925.45	0.354	0.0046	FUSE:SiC

Table 4.3: continued.

Species	IP [eV]	λ_0 [Å]	f-value [$\times 10^{-3}$]	γ [$\times 10^9\,\mathrm{s}^{-1}$]	Instrument
		930.26	0.537	0.0069	Fuse:SiC
		936.63	3.650	0.00047	Fuse:SiC
		971.74	11.6	0.0585	Fuse:SiC
		974.07	0.0156	0.00011	Fuse:SiC
		976.45	3.306	0.03848	Fuse:SiC
		1039.23	9.060	0.187	Fuse:LiF
		1302.17	48.0100	0.565	Stis
		1355.60	0.00116	-	Stis
Mg II	15.0	1239.93	0.6320	0.00137	Stis
		1240.39	0.3560	0.00154	Stis
Al II	18.8	935.27	2.51803	0.00641	Fuse:SiC
		1670.79	1738.12	1.39	Stis
Si II	16.3	1020.70	16.7920	0.1811	Fuse:LiF
		1190.42	291.945	0.5888	Stis
		1193.29	582.444	2.338	Stis
		1304.37	86.4170	0.5776	Stis
		1526.71	132.814	0.6591	Stis
Si IV		1393.76	513.0	0.86	Stis
		1402.77	254.0	0.862	Stis
P II	19.7	961.04	348.544	0.84	Fuse:SiC
		963.80	1458.86	3.49	Fuse:SiC
		1152.82	2.45041	0.395	Fuse:LiF
S II	23.4	1250.58	5.43112	0.04651	Stis
		1253.81	10.9086	0.04615	Stis
		1259.52	16.5881	0.04553	Stis
S III		1012.49	43.8134	0.281	Fuse:LiF
		1190.20	23.6254	0.0665	Stis
Ar I	15.8	1048.22	262.753	0.4940	Fuse:LiF
		1066.66	67.4488	0.1300	Fuse:LiF
Mn II	15.6	1197.18	217.0	0.784	Stis
Fe II	16.2	1055.26	7.500	0.05989	Fuse:LiF
		1062.15	3.802	0.02248	Fuse:LiF
		1063.18	54.7513	0.3539	Fuse:LiF
		1081.87	12.5841	0.06647	Fuse:LiF
		1096.88	32.6469	0.2217	Fuse:LiF

Table 4.3: continued.

Species	IP [eV]	λ_0 [Å]	f-value [$\times 10^{-3}$]	γ [$\times 10^9\,\mathrm{s}^{-1}$]	Instrument
		1112.05	4.46	0.04099	FUSE:LiF
		1121.97	28.9746	0.1325	FUSE:LiF
		1125.45	15.5838	0.07234	FUSE:LiF
		1127.10	2.8	0.01575	FUSE:LiF
		1133.67	4.72	0.03891	FUSE:LiF
		1142.37	4.01	0.03195	FUSE:LiF
		1143.23	19.2251	0.0679	FUSE:LiF
		1144.94	83.0268	0.445	FUSE:LiF
		1608.45	57.7553	0.274	STIS
Ni II	18.2	1370.13	76.9551	0.41	STIS
		1454.84	32.2986	0.102	STIS
Na I	5.1	5891.58	640.8	0.06157	KECK:HIRES
		5897.56	320.1	0.06139	KECK:HIRES
Ca II	11.9	3934.7750	626.7	0.1444	KECK:HIRES
		3969.5901	311.6	0.1409	KECK:HIRES

[a] Due to the varying S/N for different data and the differences in the shape of the continua, a few of the listed transitions are not used in all six sightlines. Furthermore, some of the transitions for which measurements were impossible, either for being in the spectral gap between the detector channels, or being excluded because of the high uncertainties due to e.g., blending with other strong absorptions, are not in this list. For a complete list see Morton & Dinerstein (1976); Morton (2003).

[b] From Morton (2003).

Table 4.4: List of H_2 transitions considered for one or more sightlines[a], and their rest-wavelength (λ_0)[b], f-value[b], damping constant (γ)[b], and the instrument with which they were observed.

transition	λ_0 [Å]	f-value [$\times 10^{-3}$]	γ [$\times 10^{9}\,\mathrm{s}^{-1}$]	Instrument
Ly R(0)14-0	946.16833	1.22926	0.971428	FUSE:SiC
Ly R(0)12-0	962.97626	13.1628	0.98151	FUSE:SiC
Ly R(0)10-0	981.43713	20.6905	1.07166	FUSE:SiC
Ly R(0)8-0	1001.8207	26.768	1.17674	FUSE:LiF
Ly R(0)7-0	1012.8105	29.7022	1.23598	FUSE:LiF
Ly R(0)6-0	1024.3721	28.7135	1.30058	FUSE:LiF
Ly R(0)4-0	1049.3674	23.1932	1.44841	FUSE:LiF
Ly R(0)3-0	1062.8821	17.8954	1.534	FUSE:LiF
Ly R(0)2-0	1077.1399	11.6628	1.62956	FUSE:LiF
Ly R(0)1-0	1092.1949	5.78362	1.73796	FUSE:LiF
Ly R(0)0-0	1108.1271	1.66457	1.86315	FUSE:LiF
Ly R(1)15-0	939.12170	6.55821	0.866061	FUSE:SiC
Ly R(1)13-0	955.70752	4.22714	0.940969	FUSE:SiC
Ly R(1)10-0	982.07269	13.6423	1.06992	FUSE:SiC
Ly P(1)10-0	982.83453	6.81124	1.07254	FUSE:SiC
Ly R(1)8-0	1002.4491	18.2318	1.17448	FUSE:LiF
Ly P(1)8-0	1003.2944	8.46602	1.17789	FUSE:LiF
We Q(1)0-0	1009.7709	23.8009	1.17973	FUSE:LiF
Ly P(1)7-0	1014.3256	8.98227	1.23723	FUSE:LiF
Ly R(1)5-0	1037.1489	18.1343	1.36812	FUSE:LiF
Ly P(1)5-0	1038.1569	8.66065	1.37233	FUSE:LiF
Ly R(1)4-0	1049.9598	15.5468	1.44523	FUSE:LiF
Ly P(1)4-0	1051.0332	7.6016	1.44976	FUSE:LiF
Ly P(1)3-0	1064.6061	5.94144	1.53547	FUSE:LiF
Ly R(1)2-0	1077.7002	7.69332	1.62575	FUSE:LiF
Ly P(1)2-0	1078.9272	3.92145	1.63118	FUSE:LiF
Ly R(1)1-0	1092.7323	3.78018	1.73374	FUSE:LiF
Ly P(1)1-0	1094.0521	1.96793	1.73977	FUSE:LiF
Ly R(1)0-0	1108.6329	1.0767	1.85847	FUSE:LiF
Ly R(2)15-0	940.62335	6.02792	0.864345	FUSE:SiC
We Q(2)2-0	967.27838	34.9972	1.13748	FUSE:SiC
We P(2)2-0	968.29193	7.22861	1.1381	FUSE:SiC
Ly R(2)8-0	1003.9820	16.6183	1.17141	FUSE:LiF
Ly P(2)8-0	1005.3898	9.91074	1.17674	FUSE:LiF

Table 4.4: continued.

transition	λ_0 [Å]	f-value [$\times 10^{-3}$]	γ [$\times 10^9\,\mathrm{s}^{-1}$]	Instrument
We R(2)0-0	1009.0240	15.6487	1.17759	FUSE:LiF
We Q(2)0-0	1010.9381	23.81	1.1785	FUSE:LiF
We P(2)0-0	1012.1691	5.50992	1.17999	FUSE:LiF
Ly R(2)7-0	1014.9739	18.9366	1.22952	FUSE:LiF
Ly P(2)7-0	1016.4584	10.2324	1.23598	FUSE:LiF
Ly R(2)5-0	1038.6888	16.5032	1.36375	FUSE:LiF
Ly R(2)4-0	1051.4980	14.0305	1.44048	FUSE:LiF
Ly P(2)4-0	1053.2839	9.02132	1.44841	FUSE:LiF
Ly P(2)3-0	1066.9004	7.0895	1.534	FUSE:LiF
Ly R(2)2-0	1079.2263	6.81807	1.62008	FUSE:LiF
Ly P(2)2-0	1081.2670	4.69883	1.62956	FUSE:LiF
Ly R(2)1-0	1094.2440	3.31231	1.72744	FUSE:LiF
Ly P(2)1-0	1096.4385	2.36607	1.73796	FUSE:LiF
Ly R(3)7-0	1017.4215	18.3846	1.22447	FUSE:LiF
Ly P(3)7-0	1019.4998	10.4758	1.23337	FUSE:LiF
Ly R(3)5-0	1041.1577	15.8466	1.35792	FUSE:LiF
Ly P(3)5-0	1043.5022	10.7673	1.36812	FUSE:LiF
Ly R(3)4-0	1053.9760	13.3571	1.43419	FUSE:LiF
Ly P(3)4-0	1056.4716	9.55577	1.44523	FUSE:LiF
Ly P(3)3-0	1070.1411	7.53713	1.53052	FUSE:LiF
Ly R(3)2-0	1081.7125	6.36254	1.61254	FUSE:LiF
Ly R(3)1-0	1096.7252	3.05341	1.71906	FUSE:LiF
Ly P(3)1-0	1099.7872	2.52571	1.73374	FUSE:LiF
Ly P(3)0-0	1115.8953	0.738067	1.85847	FUSE:LiF
We R(4)0-0	1011.8123	13.9548	1.17215	FUSE:LiF
We P(4)0-0	1017.3846	9.94639	1.17759	FUSE:LiF
Ly R(4)7-0	1020.7638	18.1378	1.21831	FUSE:LiF
Ly P(4)7-0	1023.4338	10.4925	1.22952	FUSE:LiF
Ly P(4)6-0	1035.1807	11.2658	1.29396	FUSE:LiF
Ly R(4)5-0	1044.5424	15.484	1.35079	FUSE:LiF
Ly P(4)5-0	1047.5504	10.9902	1.36375	FUSE:LiF
Ly R(4)4-0	1057.3800	12.9373	1.42642	FUSE:LiF
Ly P(4)4-0	1060.5806	9.79374	1.44048	FUSE:LiF

[a] For the same reasons as in Table 4.3[a] a few of the listed transitions are not used in all six sightlines.

[b] From Abgrall et al. (1993a,b).

Chapter 5

Small-scale density variations in Milky Way disc gas towards the LMC

Despite the large number of detections, the nature of the small-scale structures and their ubiquity is yet poorly understood. It is not always clear whether the observations reflect the variation in H I *column density, or whether they are caused by changes in the physical conditions of the gas over small scales. In this Chapter, we use UV absorption data mainly from* FUSE, *and partly from* STIS, *of six LMC stars (Sk -67° 111, LH 54-425, Sk -67° 107, Sk -67° 106, Sk -67° 104, and Sk -67° 101) that are all located within* $5'$ *of each other, and analyse the physical properties of the Galactic disc gas in front of the LMC on sub-parsec scales. The results suggest that the detected* H_2 *structures in these six lines of sight are not necessarily physically connected, but that we are sampling partly molecular structures with sizes* $< 0.1 - 1.8\,pc$ *and possibly different gas densities. This Chapter is based on Nasoudi-Shoar et al. (2010).*

5.1 Introduction

Observations show that the interstellar medium contains substructure on scales less than 1 pc, detected in the form of spatial and temporal variations in column densities or optical depth. Despite the number of detections, the nature and ubiquity of the small-scale structure in the ISM is not yet fully understood. In absorption-line spectroscopy most cases of temporal or spatial small-scale structures are observed in optical high-resolution spectra which often provide little information on the physical conditions in the gas. Using UV spectra, valuable information can be gained about the physical properties of the gas (e.g., Welty 2007; Richter et al. 2003a,b), in particular from observed absorption of molecular hydrogen in the Lyman and Werner bands (Chapter 3), and of fine-structure levels of neutral carbon (Sect. 2.6).

The Large Magellanic Cloud (LMC) has many bright stars with small angular separation on the sky, and provides a good background for studying the gas in the disc and the halo of the Milky Way at small spatial scales. Here we have chosen data from the

Far Ultraviolet Spectroscopic Explorer (FUSE) and from the Space Telescope Imaging Spectrograph (STIS) of the six LMC stars Sk-67°111, LH 54-425, Sk-67°107, Sk-67°106, Sk-67°104, and Sk-67°101, with small angular separations to study the structure and the physical properties of the foreground gas on small spatial scales.

5.2 The data and the approach

We used FUV absorption-line data from FUSE with relatively high S/N (Table 4.2) to analyse the spectral structure in six lines of sight with small angular separations. For four of our sightlines (Sk-67°107, Sk-67°106, Sk-67°104, and Sk-67°101) high-resolution STIS observations were also available. In total we cover the wavelength range 905-1730 Å (with some gaps due to the diversity of the instruments and detectors), where we can find most electronic transitions of many atomic species and molecular hydrogen. For more details about the data see Chapter 4.

In the order of right ascension our target stars are: Sk-67°111, LH 54-425, Sk-67°107, Sk-67°106, Sk-67°104, and Sk-67°101 (see Fig. 5.1). These are all bright stars of spectral types O and B, lying on an almost straight line at constant declination, and spread over 5′ in RA (see Table 4.1). Because the stars are separated mainly in their RA, we have considered the projected separations in that coordinate. The smallest separation is however between LH 54-425 and Sk-67°107, both having almost the same RA, which means that we have to take into account the true separation of 17″ (essentially in the declination), when comparing these two sightlines.

In this Chapter we analyse the Milky Way disc component at the velocity $v_{\rm LSR} \simeq 0$ to 8 $\rm km\,s^{-1}$ (with the H_2 absorption lines typically having a higher velocity compared to the metal lines), where the absorptions by molecular hydrogen and metals enable a detailed study of the properties of the gas along each line of sight. We selected primarily absorption lines of H_2 to study the fine structure of the gas. This allows us to derive the physical properties in the coolest regions, such as the temperature and the density. Moreover, in the FUV range many absorption lines from the same lower electronic level are available, thus allowing the relatively accurate determination of the respective COG (see, e.g., de Boer et al. 1998; Richter et al. 1998; Richter 2000). We also included available metal lines in the study, which are the lines of C I, C I*, C I**, N I, O I , Al II, Si II, P II, S III, Ar I, and Fe II. For the four sightlines with available STIS observations (Sk-67°107, Sk-67°106, Sk-67°104, and Sk-67°101), the lines of Mg II, Si IV, S II, Mn II, and Ni II were also detected, as well as additional absorption lines by some of the species already detected with FUSE (see Table 4.3 for a list of analysed metal absorption lines). Some of the metal absorption further reveal an additional weak component at $v_{\rm LSR} \approx -30$ $\rm km\,s^{-1}$, which we describe briefly, while we concentrate on the analysis of the strong disc component[1].

For each velocity component the equivalent width of the absorption was measured either by integrating the pixel to pixel area up to the continuum level, or by Gaussian fits with

---

[1] We refer to the absorptions with similar LSR velocity as parts of the same cloud. This can include more than one gas component, not resolved in the spectra due to the limited spectral resolution.

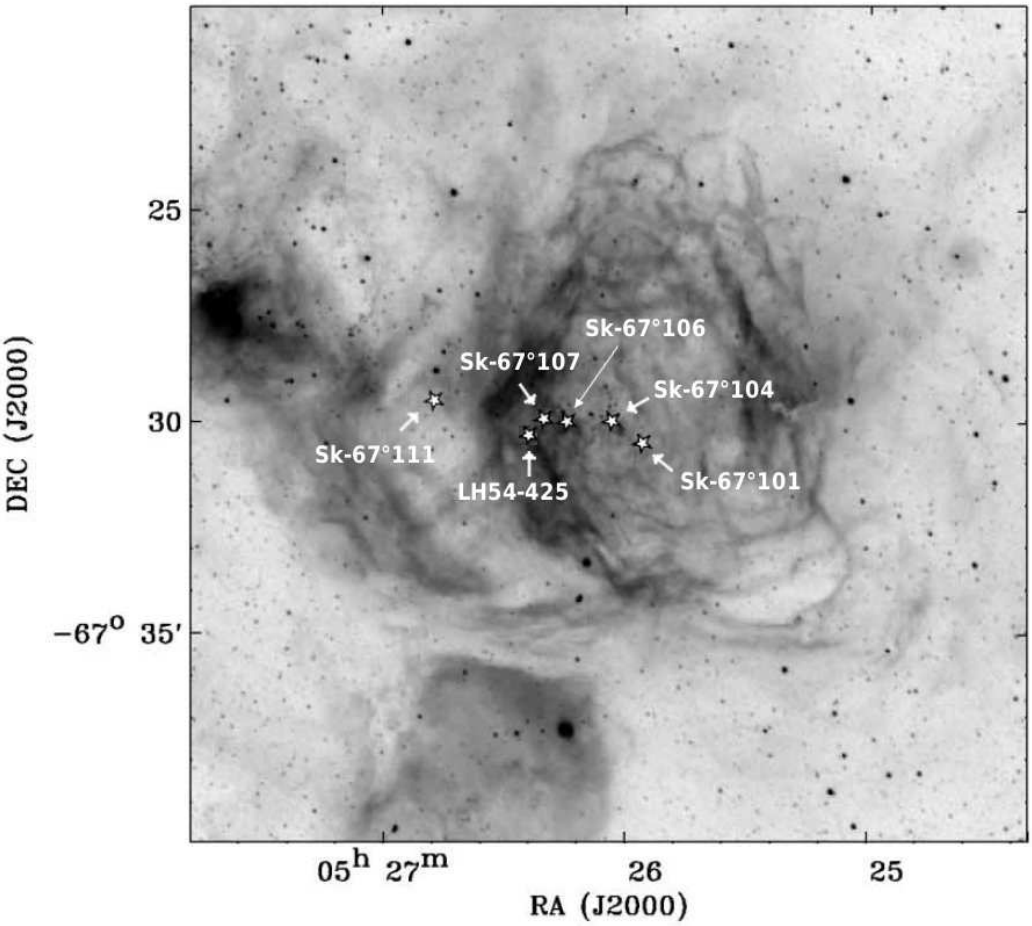

Figure 5.1: Hα image of six background stars (star symbols) in their LMC environment with their Dec (in degrees) and RA (in hours) coordinates. Note that the luminous gas around the stars is warm ionised gas of the LMC, which is not relevant for our study. Figure was taken from Danforth et al. (2002), and slightly modified.

Midas alice (only for weak lines). Owing to the large number of spectral lines within the Fuse wavelength range and the wide velocity absorption range for each transition, there is considerable blending in the interstellar lines. For the absorption lines that needed deblending, a multi-component Gaussian fit was used, except for the clearly saturated lines, where the former method was more suitable. For the final results we only took those lines into consideration where we found no blending or which could easily be decomposed by a multi-component Gaussian fit. For the O I line at 1302Å however, which is heavily saturated and also blended with its also saturated component at $v_{\rm LSR} \approx -30\,{\rm km\,s^{-1}}$, we used a different approach. We used profile fitting (with Spectralyzor) in addition to the CoG technique, with the derived column density and b-value from the other O I lines (based on the CoG method) given as the initial guess, to separate the equivalent widths of the two components.

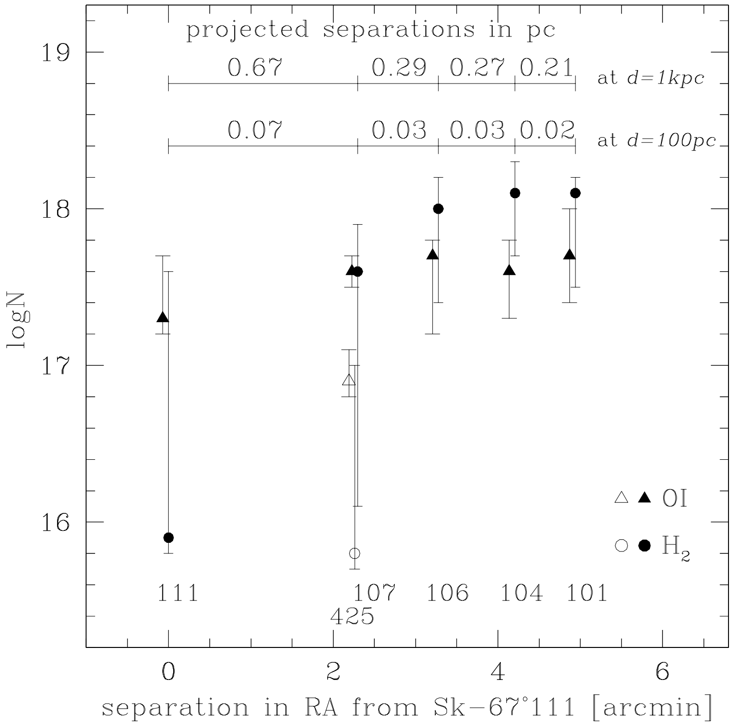

Figure 5.2: Logarithmic column densities of H_2 and O I towards Sk-67°111, LH 54-425, Sk-67°107, Sk-67°106, Sk-67°104 and Sk-67°101 (from left to right; for the identification see the numbers in the lower part of the plot), plotted against the angular separation of each star with respect to Sk-67°111 (only in RA). The data for all sightlines are presented as filled symbols (circles for H_2, and triangles for O I), except for LH 54-425, where they are given as empty symbols. The O I data were slightly shifted to the left for a better visualisation. Data for LH 54-425 were shifted slightly more to the left for clarity. On top of the plot the projected linear separation in pc between each pair of stars is marked for the assumed distances of $d = 100$ pc and $d = 1$ kpc. The increase of the H_2 column density from Sk-67°111 to Sk-67°101 is not seen in the O I column density.

A standard CoG method (Sect. 4.2.2) was used to derive the column density $N\,[\mathrm{cm}^{-2}]$ and the Doppler parameter $b\,[\mathrm{km\,s}^{-1}]$ for each species. These values are presented in Table 5.1 together with the 1σ errors. Note that the uncertainties in the column densities are based on the errors in the equivalent-width measurements and the uncertainties in the b-values (see Sect. 4.2.2).

5.3 Molecular hydrogen in Galactic disc gas

We determined the column densities of the molecular hydrogen for the different rotational states $J = 0 - 4$. These are given as logarithmic values in Table 5.1 together with the corresponding b-values. The b-values for various rotational states of molecular hydrogen are estimated separately in each CoG analysis and vary over the range of 2 to 6 $\mathrm{km\,s^{-1}}$ for the low J for all sightlines. Thus, the various J-levels might differ slightly in their b-values, because they may sample different physical regions of the Galactic disc gas.

In our FUSE spectra we did not detect any level higher than $J = 4$ along any of our sightlines. Moreover the $J = 4$ detection was not always certain. For sightlines with no measured absorption above the $3\,\sigma$ level, we used a derived $W_{\lambda,3\sigma}$ (Eq. 4.2 in Chapter 4) for the strongest unblended transition in a fit to the linear part of the CoG for estimating an upper limit for the column density[2].

In order to visualise the various regions of the foreground cloud that we are looking at, these column densities are plotted in Fig. 5.2 against the angular separation of the background stars. Assuming that the gas exists in the disc at distances up to 1 kpc (Sect. 1.2.1), we have marked in that figure the projected separations between our sightlines. The H_2 absorption shows a clear decline in column density towards Sk -67°111, with a significant drop towards LH 54-425.

5.3.1 Note on the errors

There are different sources of errors contributing to our measured column densities. We included the errors due mainly to the continuum placement and the local S/N in the equivalent-width measurements (see Sect. 4.2.2). However, the different detectors seem to have different responses, sometimes causing slightly lower or higher equivalent widths of the same absorption. This in itself should be included in our errors in the column densities, but combining the measurements from different detectors might influence the fit to the CoG, because they include different transitions in a wide range on the CoG. For the $J = 1$ lines, a crucial role is played by one line at 1108 Å. If that line is for some reason an outlier on the CoG, $N(J = 1)$ could be overestimated for the Sk -67°101 to Sk -67°107 sightlines. On the other hand, a direct comparison of the absorption profiles clearly shows that the components towards LH 54-425 are much weaker than on the other sightlines, particularly for $J = 0$ and $J = 1$ (see Fig. 5.3 for some examples). Furthermore, it is also obvious that the $J = 0$ lines towards Sk -67°111 are much weaker than the $J = 1$ lines in comparison to the other sightlines. Thus, the differences in the $N(J = 0)/N(J = 1)$ ratios between the different sightlines are real.

The large errors in the derived column densities for some of the $N(J = 0)$ and $N(J = 1)$ are mostly due to a degeneracy of the N-b combinations, rather than covering the whole range of possible column densities; i.e., given that our best fit represents the “true” N-b combination, the errors should be much smaller than the indicated errors.

5.3.2 Physical properties of the gas from H_2

The various rotational levels of molecular hydrogen reveal the physical state of the gas. While lower J-levels are mostly populated by collisional excitations, higher J-levels are

---

[2] The fit has been including all possible $b > 2$ $\mathrm{km\,s^{-1}}$.

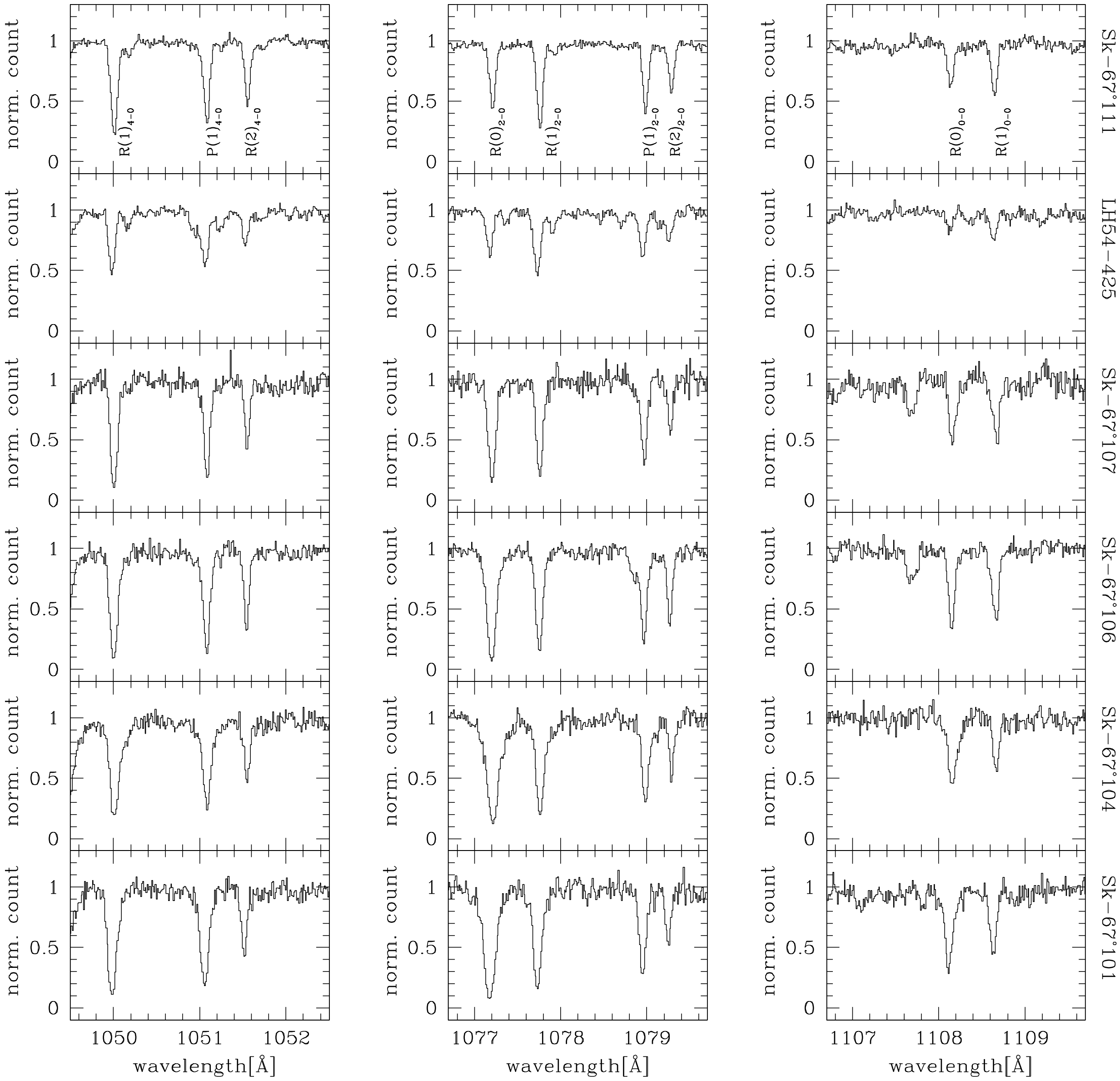

Figure 5.3: Sample of H_2 absorption lines from different excited levels shown for the different sightlines. The sightlines are labelled on the right, from top to bottom: Sk-67°111, LH 54-425, Sk-67°107, Sk-67°106, Sk-67°104, and Sk-67°101. The spectra are normalised to unity in all cases. The corresponding transitions are labelled on the upper plots of Sk-67°111, the same portion of the spectrum is plotted in each panel for the other sightlines. Note the difference in the relative strength of the absorption lines for different sightlines.

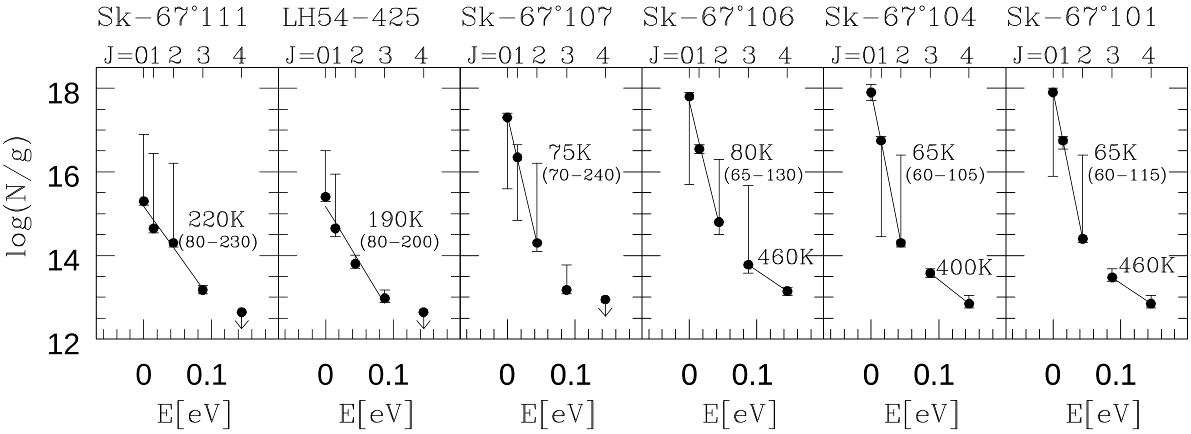

Figure 5.4: Rotational excitation of H_2 in foreground Galactic disc gas. For each sightline the column density [cm^{-2}] of H_2 in level J is divided by the statistical weight g_J and plotted on a logarithmic scale against the excitation energy E_J. The corresponding Boltzmann temperatures are given with the fitted lines. This temperature is represented by a straight line through the three lowest rotational states $J = 0$, 1, and 2. The higher J-levels indicate the level of UV-pumping. For Sk-67°111 and LH 54-425, $T_{0,3}$ is determined because the higher J-levels as well as the lower ones may be populated by UV-pumping. The values within parenthesis are the upper/lower limits for the temperature based on the extremes of the errorbars (see Sect. 5.3.1).

excited by photons through UV-pumping (Spitzer & Zweibel 1974). The population of the lowest levels can be fitted to a Boltzmann distribution resulting in the Boltzmann excitation temperature, $T_{\rm exc}$ for the gas, the population of higher levels can be fitted in a similar way leading to an "equivalent UV-pumping temperature", $T_{\rm UV-pump}$ (Sect. 3.2.1).

In Fig. 5.4 we plotted the column density of H_2 in level J, divided by the statistical weight, g_J, against the rotational excitation energy, E_J. For most of our sightlines the rotational excitation can be represented by a two-component fit. A Boltzmann distribution can be fitted to the three lower levels $J = 0$, $J = 1$, and $J = 2$ to find the excitation temperature $T_{0,2}$ of the gas. We get the equivalent UV-pumping temperature $T_{3,4}$ through a fit to the $J = 3$ and $J = 4$ levels. The Boltzmann excitation temperature ranges from 65 K towards Sk-67°101 and Sk-67°104, to about 80 K in the directions of Sk-67°106 and Sk-67°107. This is in the typical temperatures range found for the cold neutral medium, CNM.

Towards LH 54-425 and Sk-67°111, on the other hand, a fit to the $J = 0 - 3$ levels would give a $T_{0,3}$ similar to $T_{0,1}$ and $T_{0,2}$, indicating that the $J = 2$ level is already excited by UV-pumping. Given that the derived column densities for $J = 4$ are upper limits, the gas in these two lines of sight may be fully thermalised, and a single Boltzmann fit through all points might be sufficient. In this case we have derived the excitation temperature $T_{0,3} \sim 200$ K.

Furthermore, the temperature plot supports the estimated column densities, as the indicated errors by the CoG-fit would lead to unrealistic ratios of the column densities and the statistical weight between the different J-levels. This steep drop of $N(J)$ from $J = 0$ to $J = 2$ is also generally seen in the ISM for sightlines with $\log N(J = 0) > 17$ (Spitzer & Cochran 1973).

Molecular hydrogen in the interstellar medium forms in cores of clouds where the gas is self-shielded from the ultraviolet radiation. The two-component fit to four of our sightlines with low $T_{\rm exc}$ can be interpreted as a core-envelope structure of the partly molecular gas, where the inner parts are self-shielded from the UV radiation. Detecting less H_2 towards Sk-67°111 and LH 54-425, together with the higher $T_{\rm exc}$ in these two directions, can be understood as looking towards the edge of the H_2 patch in those sightlines, where the H_2 self-shielding is less efficient. However, Sk-67°107, with a true separation of only 17.2″ from LH 54-425, shows a significantly higher column density of H_2 and a much lower temperature. Assuming that the disc gas exists at a distance between 100 pc to 1 kpc, the projected linear separation between LH 54-425 and Sk-67°107 corresponds to a spatial scale of 0.01 to 0.08 pc (essentially only in declination). This suggests that the observed H_2 patch has a dense core and a steep transition to the edge.

5.4 Metal absorption and abundances

We determined the column densities for the species C I, C I*, C I**, N I, O I, Al II, Si II, P II, S III, Ar I, and Fe II from the FUSE (and when available also from the STIS) spectra. In addition, the column densities of Mg II, Si IV, S II, Mn II, and Ni II were obtained for Sk-67°101, Sk-67°104, Sk-67°106, and Sk-67°107 using STIS data. These metal column densities are presented in Table 5.1. For a list of absorption lines used for the column density determination, see Table 4.3. Some of the species in the FUSE spectral range have additional transitions in STIS spectra, which made a more accurate determination of their column densities possible. This, together with the location of the data points on the CoG, results in uncertainties in the column densities that are smaller along some sightlines compared to others.

The better resolution of the STIS data allows us to separate the velocity component at $v_{\rm LSR} \approx -30\,{\rm km\,s^{-1}}$ that otherwise appears as an unresolved substructure in, e.g., P II and O I absorption in the FUSE spectra. This component is strongest in the metal lines of O I, Mg II, and Si II. We do not consider this component any further, as it may be part of an infalling low-velocity cloud, not connected to the gas for which we study the small-scale structure in this Chapter. Only for strong saturated lines does this component affect our measurements, as we mentioned in Sect. 5.2.

Within our spectral range Fe II appears in a number of transitions with a wide range in f-values, making an accurate fit to the CoG possible. Some of the other species, on the other hand, have only few transitions in our spectra within a small $\log f\lambda$ range, and therefore can be fit to a wide range of b-values. Owing to the lack of more information about the Doppler widths of these species, we adopted the b-value of Fe II for each line of sight, and we determined the column densities of other ions from the Fe II-CoG. There are some exceptions discussed below for O I, N I, and Ar I (and C I, discussed in the next

Section).

For O I we find a number of transitions within the FUSE spectral range, and two additional lines within the STIS spectral range (see Table 4.3). The derived Doppler parameters of O I are very similar to those of Fe II. This can be expected because turbulent broadening dominates thermal broadening in the LISM. We have derived them separately, however. With both saturated and very weak O I lines, we are able to make a relatively accurate fit to the CoG (see Fig. 5.5) and do not need to rely on the accuracy of the Fe II-CoG. Adopting the Fe II-CoG would furthermore lead to unsatisfying fits in most cases. We plotted in Fig. 5.2 the measured O I column densities together with those of H_2. The N(O I) stays constant within the errors between the lines of sight, except for the decrease towards LH 54-425.

N I is also detected in a number of transitions. These lines also yield $b = 7\,\mathrm{km\,s^{-1}}$, even though they are mainly on the flat part of the CoG, which makes the determination of the CoG less certain. N I probably originates from the same physical region of the neutral gas as O I. We therefore adopted the O I-CoG to determine the column densities of N I. Assuming that also Ar I mainly exists with the O I in the neutral gas, we fitted the two detected Ar I absorptions to the O I-CoG as well.

Si II has only one moderately strong line in the FUSE spectra (see Table 4.3) and some very strong absorptions in STIS. The absorption at 1020.7 Å possibly is an outlier though when adopting the Fe II-CoG, because it appears too low on the CoG. Hence the reduction of the N(Si II) towards Sk -67°111 and LH 54-425, compared to the rest of the sightlines, is mainly due to the lack of further available data, rather than reflecting the differences in the equivalent width of the λ1020.7 line. We therefore represent the N(Si II) towards Sk-67°111 and LH 54-425 as lower limits in Table 5.1. It is possible that this problem occurs because of the sampling of different gas components. This would appear more strongly in the stronger absorptions compared to the weaker ones, which would explain why the λ1020.7 line appears too low on the CoG, compared to the much stronger lines of the STIS spectra.

The metal column densities show mostly insignificant variations between our lines of sights, but are generally the lowest towards LH 54-425. Below we investigate the variations in form of abundance ratios. Due to the lack of information about H I column densities with a spatial resolution that corresponds to our particular sightlines, we derive the abundances as the ratio $[\mathrm{X/O}] = \log(\mathrm{X^i/O}) - \log(\mathrm{X/O})_\odot$, with the solar abundances taken from Asplund et al. (2005), and the assumption that the detected X^i is the dominant ion of the element X. O I is an ideal tracer for H I since, unlike iron and silicon, only small fractions are depleted into dust grains, it has the same ionisation potential as hydrogen, and both atoms are coupled by a strong charge-exchange reaction in the neutral ISM. Some of the derived metal abundances are plotted in Fig. 5.6 against the angular separation of the sightlines.

N I, with an ionisation potential of 14.1 eV, acts as another tracer for the neutral gas. Our derived [N I/O I] abundances are in general close to solar, except towards Sk -67°106 and Sk -67°104, where they are somewhat lower. The ionisation balance of N I is more sensitive to local conditions of the ISM, as N I is not as strongly coupled to H I as O I (Jenkins et al. 2000; Moos et al. 2002). We therefore can expect the [N I/H I] to vary within a spatial scale, while [O I/H I] remains constant. Thus, the variation of [N I/O I] could suggest a lower shielding towards the sightlines with observed lower [N I/O I]. Jenkins et al. (2000) have modelled the deficiency of local N I with decreased H I column density. It is thus possible that the variation of [N I/O I] between our sightlines are caused by the actual variations in the density. The N I absorptions are, however, not easily measured due to the multiplicity of the transition, which can lead to high uncertainties in the N I column densities.

Fe, Mn, and Ni are generally depleted into dust grains in the Galactic disc, which can explain their low relative abundances (Fig. 5.6).[3] The underabundance of Ar can, however, be explained by the large photoionisation cross-section of Ar I (Sofia & Jenkins 1998). The slightly higher [Ar/O] towards LH 54-425 and Sk -67°111 would then suggest a higher shielding in these sightlines compared to the others, provided that the derived column densities are precise. [Si II/O I], on the other hand, is close to solar in the lines of sight Sk -67°107 to Sk -67°101 (with available weak and strong absorption lines). As Si II is the dominant ion in both warm neutral medium (WNM), and warm ionised medium (WIM), these ratios might indicate that part of the Si II absorption originates from the ionised gas. If silicon is partly depleted into dust grains, these ratios could be even higher. Furthermore, the detection of Si III (not included in Table 4.3 due to heavy saturation), and Si IV strongly suggests the presence of gas that is partially or predominantly ionised.

While the metal absorptions show no change in the ionisation structure in the gas on the lines of sight Sk -67°107 to Sk -67°101, the lines of sight to Sk -67°111 and LH 54-425 distinguish themselves from the other sightlines. Every line of sight samples a mix of CNM, WNM, and WIM, of which the fraction of ionised gas appears to be higher in the lines of sight Sk -67°107 to Sk -67°101.

It would have been favourable if the H I column densities would have been known from 21-cm data. Such high spatial resolution data do not exist. The Galactic All Sky Survey, GASS (McClure-Griffiths et al. 2009; Kalberla et al. 2010), has a resolution of only 16′, which does not help for our investigation. Yet, the GASS 21-cm profiles show over 30′ a slight trend. The high velocity resolution of the GASS 21-cm data reveals a two-component profile at velocities of +4 and −4 $\mathrm{km\,s^{-1}}$. The intensity of the two components increases/decreases to opposite east/west directions overall in favour of a stronger H I emission to lower RA. These velocity components are not resolved in our FUSE, or STIS spectra. Considering the changes in the N(O I), however, it is likely that our pencil beam spectra could be going through the cloud boundary, where the column density summed over the two components is less towards e.g., LH 54-425 compared to the other sightlines.

---

[3] It is also worth noting that uncertainties in the f-values are not included in the measurements. The f-values for transitions listed in this thesis have, in general, proven relatively unproblematic by previous absorption-line measurements. However, errors in the f-values contribute to possible systematic errors, which could for example cause systematically low relative abundances.

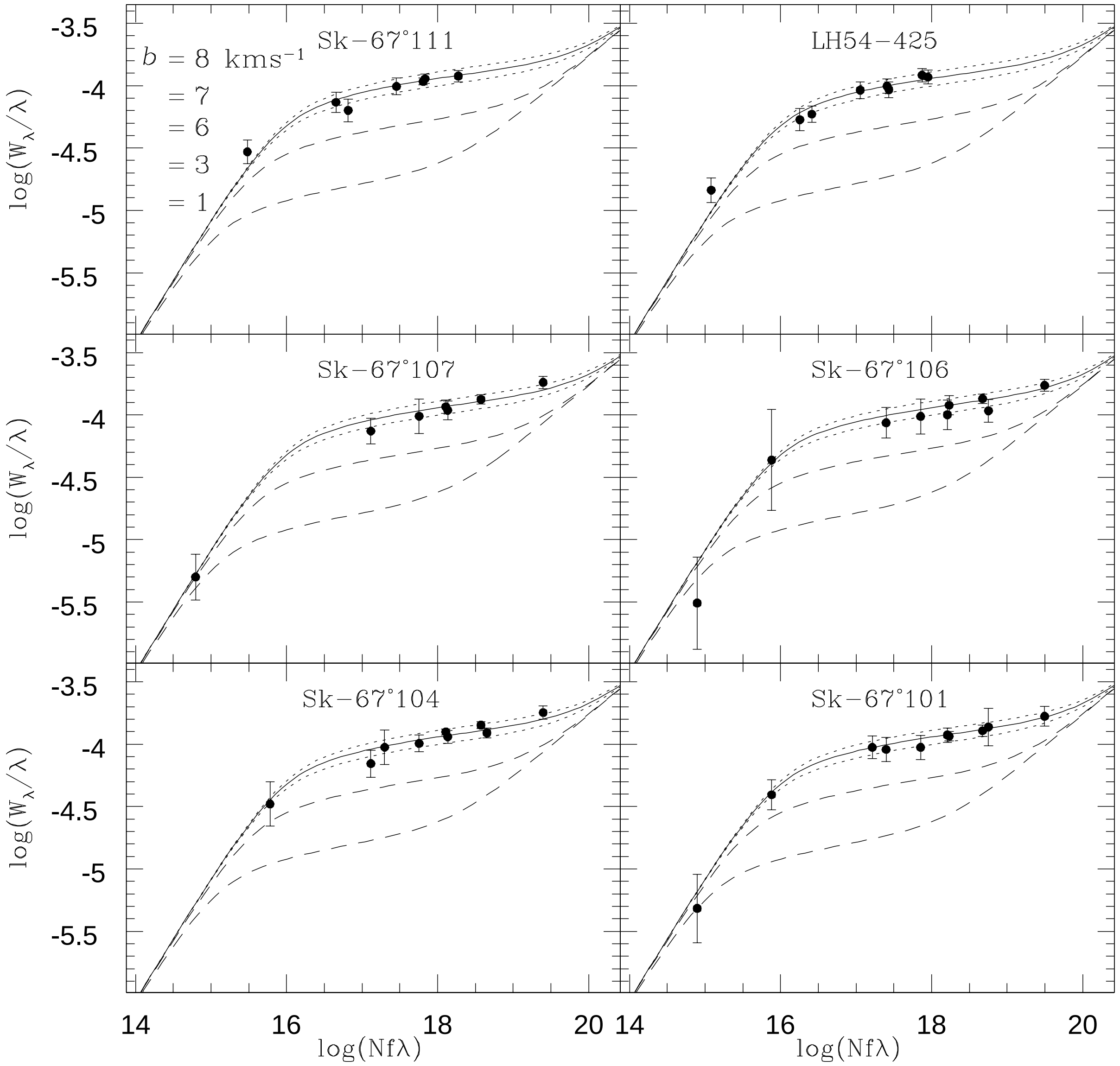

Figure 5.5: Sample of CoGs of O I for the six sightlines (the star name on top of each figure). Each plot shows CoGs for $b = 1, 3, 6, 7, 8\,\mathrm{km\,s^{-1}}$. The solid line is the resulting CoG from the best fit ($b = 7\,\mathrm{km\,s^{-1}}$), and the dotted lines ($b = 6$ and $b = 8\,\mathrm{km\,s^{-1}}$) correspond to approximately 1σ errors.

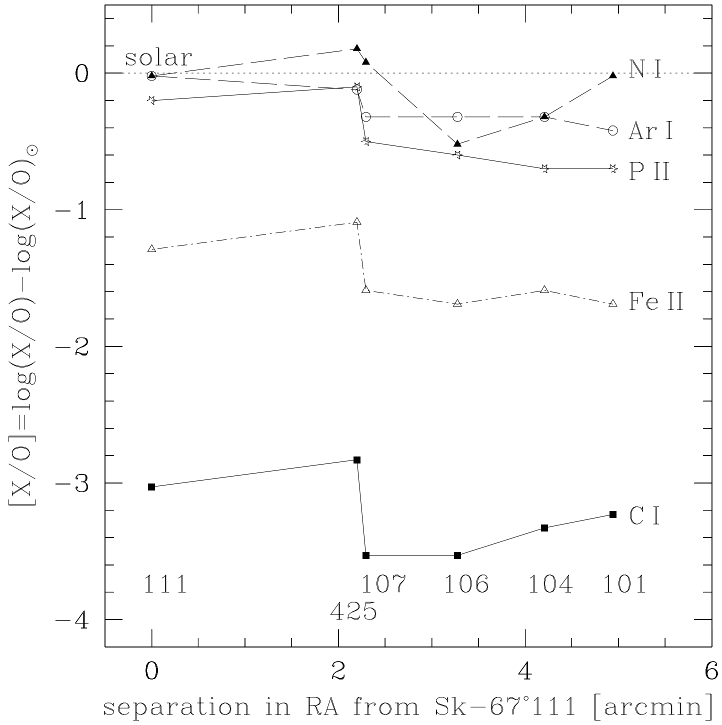

Figure 5.6: Metal abundances plotted against the angular separation. The abundances are expressed as the ratio [X/O] = log(X^i/O) − log(X/O)$_\odot$, assuming that the X^i is the dominant ion of X. X^i is given on the right side of the figure.

5.5 Gas densities

The available data allow us to derive the gas densities in two ways. One possibility is based on the H_2/O abundance and models for the self-shielding of the gas. The other uses the level of collisional excitation of C I as derived from the absorption lines (see Sect. 2.6 for the theoretical background). In the latter case the result is not only limited by the accuracy of column densities of the fine-structure levels of neutral carbon, but also by the derived $T_{\rm exc}$ from H_2.

5.5.1 Density variations derived from H_2

The observed column density variations along our sightlines observed for the various ions and H_2 suggest a change in the physical conditions in the foreground gas at relatively small spatial scales. For the metal ions, the observed column densities depend on three physical parameters: the volume density of the respective element in the gas, the fractional abundance of the observed ionisation state of that element (reflecting the ionisation conditions in the gas), and the thickness of the absorbing gas layer. These three quantities may vary between adjacent sightlines, so that the ion column densities and their variations alone

Table 5.1: Logarithmic column densities log N (N in cm^{-2}) of Galactic foreground gas, 1 σ errors, and Doppler parameter b [km s^{-1}] measured from the CoG.[a]

	Sk -67°111		LH 54-425		Sk -67°107		Sk -67°106		Sk -67°104		Sk -67°101	
Species	b	log N	b	log N	b	log N	b	log N	b	log N	b	log N
$H_2(J=0)^{F}$	4^{+1}_{-3}	$15.3^{+1.6}_{-0.1}$	2^{+1}_{-1}	$15.4^{+1.1}_{-0.1}$	3^{+4}_{-1}	$17.3^{+0.1\mathrm{c}}_{-1.7}$	3^{+8}_{-1}	$17.8^{+0.1}_{-2.1}$	2^{+1}_{-1}	$17.9^{+0.2\mathrm{c}}_{-0.2}$	4^{+9}_{-1}	$17.9^{+0.1}_{-2.0}$
$H_2(J=1)^{F}$	6^{+1}_{-4}	$15.6^{+1.8}_{-0.1}$	4^{+1}_{-2}	$15.6^{+1.3}_{-0.2}$	3^{+3}_{-1}	$17.3^{+0.3}_{-1.5}$	3^{+1}_{-1}	$17.5^{+0.1}_{-0.1}$	2^{+9}_{-1}	$17.7^{+0.1}_{-2.3}$	2^{+1}_{-1}	$17.7^{+0.1}_{-0.2}$
$H_2(J=2)^{F}$	4^{+1}_{-3}	$15.0^{+1.9}_{-0.1}$	5^{+3}_{-2}	$14.5^{+0.2}_{-0.1}$	4^{+2}_{-3}	$15.0^{+1.9}_{-0.2}$	4^{+1}_{-2}	$15.5^{+1.5}_{-0.3}$	5^{+1}_{-4}	$15.0^{+2.1}_{-0.1}$	4^{+1}_{-3}	$15.1^{+2.0}_{-0.1}$
$H_2(J=3)^{F}$	8^{+6}_{-2}	$14.5^{+0.1}_{-0.1}$	6^{+4}_{-3}	$14.3^{+0.2}_{-0.1}$	5^{+9}_{-3}	$14.5^{+0.6}_{-0.1}$	4^{+1}_{-3}	$15.1^{+1.9}_{-0.2}$	4^{+1}_{-1}	$14.9^{+0.1}_{-0.1}$	5^{+4}_{-1}	$14.8^{+0.2}_{-0.1}$
$H_2(J=4)^{F}$	> 2	< 13.6	> 2	< 13.6	> 2	< 13.9	5^{+9}_{-3}	$14.1^{+0.1}_{-0.1}$	4^{+1}_{-2}	$13.8^{+0.2}_{-0.1}$	2^{+12}_{-1}	$13.8^{+0.2}_{-0.1}$
H_2(total)		$15.9^{+1.7}_{-0.1}$		$15.8^{+1.2}_{-0.1}$		$17.6^{+0.3}_{-1.5}$		$18.0^{+0.2}_{-0.6}$		$18.1^{+0.2}_{-0.4}$		$18.1^{+0.1}_{-0.6}$
C I^{FS}	3^{+1}_{-1}	$14.0^{+0.1}_{-0.1}$	3^{+1}_{-1}	$13.8^{+0.1}_{-0.1}$	3^{+1}_{-1}	$13.8^{+0.3}_{-0.1}$	3^{+1}_{-1}	$13.9^{+0.3}_{-0.1}$	3^{+1}_{-1}	$14.0^{+0.1}_{-0.1}$	3^{+1}_{-1}	$14.2^{+0.1}_{-0.1}$
C I*^{FS}		< 13.8		< 13.8		$13.5^{+0.2}_{-0.1}$		$13.5^{+0.3}_{-0.1}$		$13.6^{+0.2}_{-0.1}$		$13.6^{+0.2}_{-0.1}$
C I**^{FS}		< 13.8		< 12.9		< 12.8		< 12.9		< 12.8		< 12.8
O I^{FS}	7^{+1}_{-1}	$17.3^{+0.4}_{-0.1}$	7^{+1}_{-1}	$16.9^{+0.2}_{-0.1}$	7^{+1}_{-1}	$17.6^{+0.1}_{-0.1}$	7^{+1}_{-1}	$17.7^{+0.1}_{-0.5}$	7^{+1}_{-1}	$17.6^{+0.2}_{-0.3}$	7^{+1}_{-1}	$17.7^{+0.3}_{-0.3}$
N I^{FS}		$16.4^{+0.1}_{-0.1}$		$16.2^{+0.4}_{-0.1}$		$16.8^{+0.1}_{-0.7}$		$16.3^{+0.4}_{-0.4}$		$16.4^{+0.1}_{-0.3}$		$16.8^{+0.4}_{-0.7}$
Ar I^{F}		$14.8^{+0.6}_{-0.1}$		$14.3^{+0.2}_{-0.1}$		$14.8^{+0.8}_{-0.3}$		$14.9^{+0.8}_{-0.3}$		$14.8^{+1.0}_{-0.3}$		$14.8^{+0.9}_{-0.3}$
Fe II^{F}	8^{+1}_{-1}	$14.8^{+0.1}_{-0.1}$	7^{+1}_{-1}	$14.6^{+0.1}_{-0.1}$	8^{+1}_{-1}	$14.8^{+0.1}_{-0.1}$	8^{+1}_{-1}	$14.8^{+0.1}_{-0.1}$	9^{+1}_{-1}	$14.8^{+0.1}_{-0.1}$	8^{+1}_{-1}	$14.8^{+0.1}_{-0.1}$
Mg II^{S}						$15.7^{+0.1}_{-0.1}$		$15.9^{+0.1}_{-0.1}$		$15.8^{+0.1}_{-0.1}$		$15.8^{+0.1}_{-0.1}$
Al II^{FS}		< 14.5		< 14.8		$15.0^{+0.2}_{-0.9}$		$15.0^{+0.3}_{-0.9}$		$14.2^{+0.8}_{-0.7}$		$14.8^{+0.3}_{-0.8}$
Si II^{FS}		$> 15.1^{\mathrm{b}}$		$> 14.9^{\mathrm{b}}$		$16.5^{+0.3\mathrm{c}}_{-0.6}$		$16.5^{+0.3\mathrm{c}}_{-0.6}$		$16.3^{+0.2}_{-0.6}$		$16.4^{+0.1\mathrm{c}}_{-0.7}$
Si IV^{S}						$13.0^{+0.1}_{-0.1}$		$13.1^{+0.1}_{-0.1}$		$13.1^{+0.1}_{-0.1}$		$13.3^{+0.1}_{-0.2}$
P II^{FS}		$13.8^{+0.2}_{-0.2}$		$13.5^{+0.1}_{-0.2}$		$13.8^{+0.2}_{-0.1}$		$13.8^{+0.2}_{-0.2}$		$13.6^{+0.2}_{-0.1}$		$13.7^{+0.3}_{-0.1}$
S II^{S}						$15.5^{+0.4}_{-0.2}$		$15.5^{+0.5}_{-0.1}$		$15.4^{+0.4}_{-0.1}$		$15.5^{+0.5}_{-0.1}$
S III^{FS}		$14.4^{+0.2\mathrm{b}}_{-0.1}$		$14.4^{+0.2\mathrm{b}}_{-0.2}$		$14.7^{+0.2}_{-0.1}$		$14.6^{+0.2}_{-0.1}$		$14.5^{+0.1}_{-0.1}$		$14.7^{+0.2}_{-0.1}$
Mn II^{S}						$13.0^{+0.1\mathrm{b}}_{-0.1}$		$13.0^{+0.1\mathrm{b}}_{-0.1}$		$13.0^{+0.2\mathrm{b}}_{-0.1}$		$13.1^{+0.1\mathrm{b}}_{-0.1}$
Ni II^{S}						$13.5^{+0.1}_{-0.1}$		$13.6^{+0.1}_{-0.1}$		$13.5^{+0.1}_{-0.1}$		$13.7^{+0.1}_{-0.1}$

[a] Most of the metal column densities are based on the adopted b from Fe II in each line of sight. N I, and Ar I are derived from the CoG of O I, and the fine-structure levels of carbon from the CoG of C I.

[b] Based on one absorption line

[c] The best fit includes outliers (less than 32% of the data points). For the H_2 data, these outliers are all the absorptions from FUSE:SiC (see Sect. 4.1). For the Si II data, the outlier is the weak line at 1020.7 Å (see Sect. 5).

[F] Based on FUSE data only

[S] Based on STIS data only

[FS] Based on both FUSE and STIS for Sk -67°107 to Sk -67°101 tells us very little about the actual (total) particle-density variations $\Delta n_{\rm H}$ in the gas. Yet it is these density variations that we wish to know in order to study the density structure of the ISM at small scales. As we show below, it is possible to reconstruct the particle density distribution in the gas by *combining* our ion column-density measurements with the H_2 measurements in our data sample, and assuming that the molecular abundance is governed by an H_2 formation-dissociation equilibrium (FDE).

In FDE, the neutral to molecular hydrogen column density ratio is governed by the Eq. (3.5) in Chapter 3. Unfortunately, the local H I column density cannot be obtained directly from our absorption measurements because the damped H I Ly β absorption in our FUSE data represents a blended composite of all absorption components in the Milky Way and LMC along the line of sight. However, as mentioned in the previous Section, neutral oxygen has the same ionisation potential as neutral hydrogen, and both atoms are coupled by a strong charge-exchange reaction in the neutral ISM, so that O I serves as an ideal tracer for H I. If we now solve the previous equation for $n_{\rm H}$ and assume that $N(\text{H I}) = z_{\rm O}\, N(\text{O I})$ with $z_{\rm O}$ as the local hydrogen-to-oxygen ratio, we obtain

$$n_{\rm H} = \frac{N({\rm H}_2)}{N(\text{O I})}\,\frac{\langle k\rangle\,\beta}{z_{\rm O}\,R}\,, \tag{5.1}$$

where $\langle k\rangle \approx 0.11$ is the probability that the molecule is dissociated after photoabsorption, β is the photoabsorption rate per second within the cloud, and R is the H_2 formation coefficient on dust grains in units $\rm cm^3\,s^{-1}$.

For interstellar clouds that are optically thick in H_2 (i.e., log $N({\rm H}_2) \gg 14$) H_2 line self-shielding has to be taken into account. The self-shielding reduces the photoabsorption rate in the cloud interior and depends on the total H_2 column density in the cloud. Draine & Bertoldi (1996) find that the H_2 self-shielding can be characterised by the relation $\beta = S\,\beta_0$, where $S = (N_{{\rm H}_2}/10^{14}{\rm cm}^{-2})^{-0.75} < 1$ is the self-shielding factor and β_0 is the photoabsorption rate at the edge of the cloud (which is directly related to the intensity of the ambient UV radiation field).

Because all our sightlines are passing with small separation through the same local interstellar gas cloud, the respective parameters β_0, R, and $z_{\rm O}$ should be identical along these sightlines. The observed quantities $N(\text{H I})$ and $N(\text{O I})$ instead vary from sightline to sightline due to the local density variations $\Delta n_{\rm H}$ and different self-shielding factors in the gas. If we now consider Eq. (5.1) and assume $\beta = S(N({\rm H}_2))\,\beta_0$, for two adjacent lines of sight (LOS1 and LOS2) through the same cloud, we obtain for the local *density ratio* ξ between LOS1 and LOS2

$$\xi = \frac{n_{\rm H,LOS1}}{n_{\rm H,LOS2}} = \frac{N(\text{O I})_{\rm LOS2}}{N(\text{O I})_{\rm LOS1}}\left(\frac{N({\rm H}_2)_{\rm LOS1}}{N({\rm H}_2)_{\rm LOS2}}\right)^{0.25}\,. \tag{5.2}$$

A small rise in $n_{\rm H}$ only slightly increases the H_2 grain formation $Rn_{\rm H}$, but it substantially reduces the photodissociation rate $\langle k\rangle\beta_0 S$ due to the increased H_2 self-shielding, so that in the end $\Delta N({\rm H}_2) \propto \Delta {n_{\rm H}}^4$ while $\Delta N(\text{O I}) \propto n_{\rm H}$. Therefore, the H_2/O I column density ratio represents a very sensitive tracer for density variations in the gas.

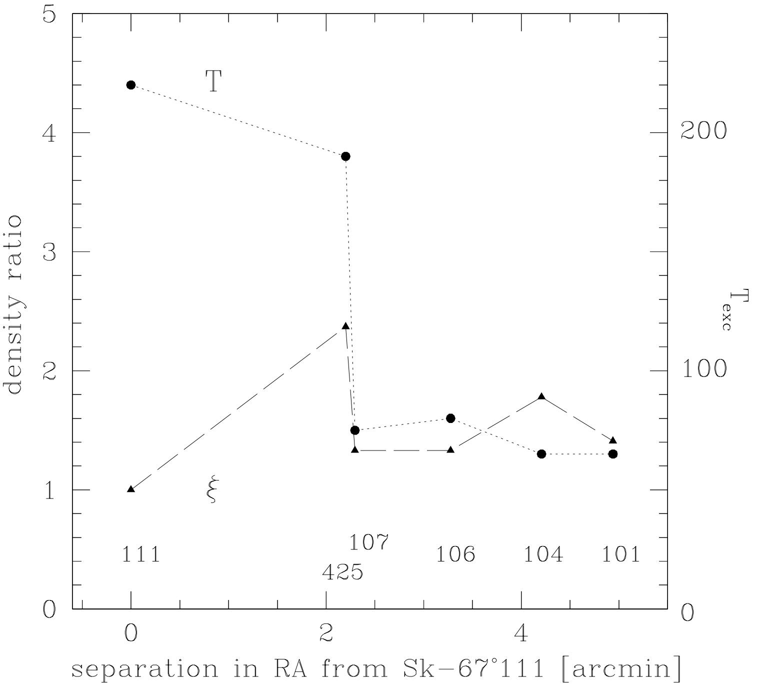

Figure 5.7: Density ratio, ξ, and the excitation temperature, T_{exc}, with angular separation from Sk-67°111 (for separation in pc see Fig. 5.2). The parameter ξ (filled triangles) is calculated according to Eq. (5.2) based on Sk-67°111 (hence $\xi = 1$ at separation 0). T_{exc} (filled circles) is taken from Fig. 5.4. The sightlines are marked with the three last numbers of the star name.

We now use Eq. (5.2) to study the density variations in the local gas towards our six lines of sight. In Fig. 5.7 we plot the relative density to Sk-67°111 together with the derived T_{exc} versus the separations in RA coordinates. While the excitation temperature suggests a cold core in the sightlines Sk-67°101, Sk-67°104, Sk-67°106, and Sk-67°107, the total mean density appears to be lower by a factor of almost 2 compared to LH 54-425.

While the column density variations of different excitational levels of H_2 suggest that we are observing a high density core of the H_2 between the sightlines Sk-67°101 to Sk-67°106, the result from the relative abundances together with the derived total density variation point to a higher mean density to LH 54-425. This might be due to a smaller total absorber pathlength in the direction of LH 54-425, which can include a slightly more confined region, for which the mean density averaged over the pathlength is higher compared to the other sightlines, or due to the higher fraction of neutral gas towards LH 54-425, on which we base ξ.

If we analyse the density n_{H} directly from Eq. (5.2) by using the typical values observed for $R = 3 \times 10^{-17}\,\mathrm{cm}^3\,\mathrm{s}^{-1}$ and $\beta_0 = 5 \times 10^{-10}\,\mathrm{s}^{-1}$ (Spitzer 1978), and the total neutral hydrogen column density $N(\mathrm{H\,I})$ derived from $N(\mathrm{O\,I})$ assuming solar oxygen abundance, we obtain $n_{\mathrm{H}} \simeq 2\,\mathrm{cm}^{-3}$ on average. This represents the lower limit required for the H_2 to exist in the FDE. The observed $N(\mathrm{O\,I})$ represents the indirect measure of the total

N(H I) along a line of sight. It is likely that only a fraction of this H I is available for the H_2 formation, and that the H_2 self-shielding is less efficient than assumed because of a complex geometry of the H_2 structures.

5.5.2 Density from C I excitation

The ground electronic state of C I is split into three fine-structure levels. The two upper levels C I* and C I** are populated through collisional excitation and some UV-pumping (de Boer & Morton 1974). We can therefore use the fine-structure levels of neutral carbon together with the excitation temperature derived from H_2, to derive the density $n_{\rm H}$ of the gas.

Using the population of the fine-structure levels as a function of $n_{\rm H}$ and T (calculated by de Boer & Morton (1974), see Fig. 2.5 in Chapter 2), we find the densities in the range of $\sim 40-60$ cm^{-3} on the lines of sight Sk -67°101 to Sk -67°106, and a higher density of ~ 80 cm^{-3} towards Sk -67°107 (see Table 5.2). The densities derived in this way are dependent on the accuracy in the temperature, as well as the C I column densities. For LH 54-425 and Sk -67°111 we are only able to derive an upper limit for C I*, and hence upper limits of < 126 and < 65 cm^{-3}, respectievly for $n_{\rm H}$ in these sightlines. Note that these upper limits are not comparable. While the upper limit of C I* towards LH 54-425 was based on an absorption with f-value similar to the ones used towards Sk -67°107 to Sk -67°101, the C I* upper limit for the Sk -67°111 sightline was based on a weaker line, since the same spectral region was occupied by an absorption of a different velocity component.

The column densities of C I also allow us to calculate the ionisation balance, assuming that the abundance ratio of C to O is solar. Using Eq. (2.29) in Chapter 2, we obtain

$$\frac{N(\mathrm{C\,II})}{N(\mathrm{C\,I})} = \frac{\Gamma}{\alpha(T)\;n_e}\,, \tag{5.3}$$

and assuming $N(\mathrm{C})=(\mathrm{C/O})_\odot \cdot N(\mathrm{O})$ this can be written as

$$\frac{N(\mathrm{C\,I})}{N(\mathrm{O\,I})} = \frac{(\mathrm{C/O})_\odot\;\alpha(T)\;n_e}{\Gamma}\,. \tag{5.4}$$

Using $(\mathrm{C/O})_\odot \simeq 0.6$ (Asplund et al. 2005), $\alpha(T \simeq 70\,\mathrm{K}) \simeq 12\cdot 10^{-12}\,\mathrm{cm^3\,s^{-1}}$ (Péquignot & Aldrovandi 1986) and $\Gamma(\mathrm{C}) = 310 \cdot 10^{-12}\,\mathrm{s^{-1}}$ (de Boer et al. 1973), one arrives at

$$\frac{N(\mathrm{C\,I})}{N(\mathrm{O\,I})} = 0.025\;n_e\,. \tag{5.5}$$

Note that for $T \simeq 210\,\mathrm{K}$ α would be smaller by a factor of 1.7. And for strong shielding of UV radiation, Γ would be up to a factor of 2 smaller (see de Boer et al. 1973). The column density ratios of C I to O I lead to values of n_e as given in Table 5.2. We used the value of $\alpha(T \simeq 70\,\mathrm{K}) \simeq 12 \cdot 10^{-12}$ for the sightlines Sk -67°107 to Sk -67°101 and for the other two sightlines the 1.7 times smaller value.

These values, in combination with n(C I), indicate a larger ionisation fraction towards Sk -67°111 and LH 54-425.

Table 5.2: Physical conditions in the Milky Way foreground gas as derived from the data.

star	Sk -67°111	LH 54-425	Sk -67°107	Sk -67°106	Sk -67°104	Sk -67°101	Sect.
$\log N(\mathrm{H\,I})$	20.6	20.2	20.9	21.0	20.9	21.0	5.5.1[a]
$\log N(\mathrm{H_2})$	15.9	15.8	17.6	18.0	18.1	18.1	5.3
T_{exc} (H_2) [K]	220	190	75	80	65	65	5.3.2
ξ	1.0	2.4	1.3	1.3	1.8	1.4	5.5.1
$n_{\mathrm{H}}(\mathrm{C\,I})$ [$\mathrm{cm^{-3}}$]	<65	<125	80	55	65	40	5.5.2
n_e [$\mathrm{cm^{-3}}$]	0.045	0.072	0.007	0.007	0.005	0.014	5.5.2
D_{tot} [pc]			3.5	6.5	4.5	9	6.5
D_{mol} [pc]	0.6[b]	0.1[b]	0.5	1.1	0.8	1.8	6.5
Shielding (from H_2):							
	low	low					5.3.2
Depletion							
Fe,Mn,Ni			high	high	high	high	5.4

[a] Derived from O I and $(\mathrm{O/H})_\odot = -3.34$ (Asplund et al. 2005).
[b] Based on ξ and a reference LOS averaged over the values for Sk -67°101 to Sk -67°107.

5.6 Conclusions

The H_2 absorptions show considerable variation between our sightlines. The lines of sight to Sk -67°101 and Sk -67°104 contain a significantly higher amount of H_2, about 2 dex in their column densities, compared to Sk -67°111. The rotational excitation of H_2 towards Sk -67°101 to Sk -67°107 agrees with a core-envelope structure of the H_2 gas with an average temperature of $T_{\mathrm{exc}} \sim 70\,\mathrm{K}$, typical for CNM. This, and the low Doppler parameter of the lower J-levels, indicates that the molecular hydrogen probably arises in confined dense regions in these sightlines, where it is self-shielded from UV-radiation. The gas to LH 54-425 and Sk -67°111, on the other hand, appears to be fully thermalised, with $T_{\mathrm{exc}} \sim 200\,\mathrm{K}$. This could suggest that within the $< 5'$, we sample a core of a molecular hydrogen cloud, and reach the edge between Sk -67°107 and Sk -67°111. After including the LH 54-425 sightline in our study, however, the spatial variation is not a smooth change from Sk -67°101 to Sk -67°111 (Fig. 5.7), and density fluctuation on scales smaller than the extent of $5'$ cannot be excluded.

The density derived based on the fine-structure levels of neutral carbon[4] (assuming that C I and H_2 exist in the same physical region) of $n_{\mathrm{H}} \simeq 40 - 80\,\mathrm{cm^{-3}}$ is well above the one derived based on a formation-dissociation equilibrium of H_2, of $n_{\mathrm{H}} \simeq 2\,\mathrm{cm^{-3}}$. This is most likely because the available hydrogen for molecular formation is less than the total Galactic $N(\mathrm{H\,I})$ derived from $N(\mathrm{O\,I})$ along a line of sight. Moreover, the H_2 self-shielding could be overestimated (and thus n_{H} underestimated) because of a complex absorber geometry. Thus that value for n_{H} gives a minimum density required for the existence of the H_2.

---

[4] towards Sk -67°101 to Sk -67°107, for which we have relatively accurate measurements for column densities of C I and C I*, as well as T_{exc}.

On all sightlines $N(\mathrm{H}_2) \ll \mathrm{N(H\,I)}$. If we assume that $[N_\mathrm{H}]_\mathrm{tot}$ is proportional to n_H (from C I) in the same way as for the inner region of a molecular cloud (meaning $[n_\mathrm{H}/N(\mathrm{H\,I})]_\mathrm{tot} = [n_\mathrm{H}/N(\mathrm{H\,I})]_\mathrm{mol}$), we can derive from Eq. (5.1) the column density of H I that coexists with H_2 in FDE. We so find that this is 18% of the total $N(\mathrm{H\,I})$ (averaged over the sightlines Sk-67°101 to Sk-67°107). It is of course likely that the partly molecular core is more dense because it is confined, and n_H not linearly related to the $N(\mathrm{H\,I})$ as assumed above. Furthermore, $[n_\mathrm{H}]_\mathrm{tot}$ as derived from C I is the averaged density of the molecular part of the gas, where C I exists, and again not related to all the H I gas along a line of sight as assumed above. Thus, the $N(\mathrm{H\,I})_\mathrm{tot}$ together with the $n_\mathrm{H} = 40 - 80\,\mathrm{cm}^{-3}$ give only an upper limit for the pathlength of the partly molecular cloud to be $D_\mathrm{mol} = 0.5 - 1.8\,\mathrm{pc}$ (included in Table 5.2). These derived pathlengths are of the same size as (or smaller than) our lateral extent of the sightlines ($\leq 1.5\,\mathrm{pc}$, the linear separation between Sk-67°111 and Sk-67°101, assuming that the absorbing gas is located at a distance of $\leq 1\,\mathrm{kpc}$). This derived upper limit for D_mol also agrees with the higher density ratio for the LH 54-425 sightline, derived in Sect. 5.5.1, which otherwise is difficult to explain if we consider this sightline to sample the edge of the same cloud with the core on the Sk-67°101 to Sk-67°107 sightlines. Based on ξ and an average density of $n_\mathrm{H} = 60\,\mathrm{cm}^{-3}$, D_mol in the direction of LH 54-425 and Sk-67°111 is estimated to be 0.1 and 0.6 pc, respectively. Given these small sizes, the H_2 patches observed on these six lines of sight are not necessarily connected. The small pathlength is further important for the shielding of the molecular gas, given the small amount of H I that is possibly available in FDE with H_2.

We thus conclude that the H_2 observed along these six lines of sight exists in rather small cloudlets with an upper size $D_\mathrm{mol} = 0.5 - 1.8$, and possibly even less, $< 0.1\,\mathrm{pc}$, as implied by the LH 54-425 sightline. Sub-pc structure of molecular clouds have been detected in previous studies by e.g., Pan et al. (2001), Lauroesch et al. (2000), Richter et al. (2003a,b), and Marggraf et al. (2004).

The absorber pathlength through the disc has previously been found to be divided into smaller cloudlets of H I-absorbers (Welty et al. 1999), which are not necessarily physically connected to the cloud with the observed H_2. While the clumpy nature of H_2 is verified by different studies, the Galactic H I gas, when sampled over a line of sight, normally does not show variations on small scales, since such effects statistically cancel out and smooth the total observed H I (or O I in our case). If such cloudlets exist in the Galactic disc component, their LSR velocity should be similar, and therefore would not be resolved in our spectra. Our derived density ratio ξ, as well as the relative abundances, suggest that the number of these absorbers might differ along the sightlines, being less towards LH 54-425 and Sk-67°111. This interpretation also agrees with the higher electron density derived for these lines of sight.

We summarised in Chapter 1 the detection of small-scale structure by different independent methods. This Chapter presents yet another approach to identify the structure of the gas on small scales. FUV and UV spectral data, with the large range of transitions particularly of H_2 and O I together with the fine-structure of C I, provide a sensitive approach to study the physical properties of the gas on small scales. However, our spatial resolution is limited to the separation of our background sources, and does not allow us to directly detect the fine structure that might exist on even smaller scales. Our findings are consistent with the small-scale structure found earlier in the interstellar medium, and suggest inhomogeneity in the interstellar Galactic gas down to, and possibly below, scales of 0.1 pc.

Chapter 6

H_2 in the halo gas and indications for small-scale structure

Molecular hydrogen has previously been detected in a number of intermediate and a few high-velocity clouds. The presence of this molecule in diffuse gas in particular, is interesting for studying sub-parsec structures. Using data from the FUSE *we analyse interstellar absorptions by molecular hydrogen and by metals in the intermediate-velocity cloud (IVC) and the high-velocity cloud (HVC) towards the LMC stars Sk -67° 111, LH 54-425, Sk -67° 107, Sk -67° 106, Sk -67° 104 and Sk -67° 101, among which Sk -67° 111 and LH 54-425 show clear detection of* H_2 *in the IVC. Assuming standard formation and destruction mechanisms of* H_2 *we estimate the gas densities in these structures to be* $n_{\mathrm{H}} \simeq 600$ *cm*$^{-3}$*. Our results suggest the existence of substantial substructure in diffuse Galactic halo gas with* $N(\mathrm{H\,I}) \leq 3.5 \times 10^{18}$ *cm*$^{-2}$*, the formation and maintenance of which is under debate. This Chapter is based on Nasoudi-Shoar et al. (2010, submitted).*

6.1 Introduction

Because the H_2 measurements provide important information on temperature and density of the gas, the detection of H_2 in the halo opened new insight into Galactic halo structure. H_2 was first detected in the high-velocity clouds with ORFEUS by Richter et al. (1999). Subsequent measurements with FUSE showed that H_2 is present on several lines of sight through the Milky Way halo, with in general low column densities (see Richter et al. (2003b); Richter & de Boer (2004), and references therein). In a few cases H_2 was detected in IV gas at a radial velocity $v_{\mathrm{LSR}} \approx +50$ to $+60$ km s^{-1} in front of the LMC (Gringel et al. 2000; Richter et al. 2001, 2003a; Bluhm et al. 2001). Particularly interesting is the presence of H_2 in diffuse halo clouds, with H I column densities $\leq 10^{20}$ cm^{-2}. The detected H_2 in the IV gas towards the LMC star SK -68 80 stands out for this reason. With the detection of H_2 in that diffuse IV gas, Richter et al. (2003a) discussed the existence of small-scale structure in form of dense filaments possibly related to the "tiny-scale atomic structure", TSAS (Heiles (1997), see Sect. 1.3.4).

In this Chapter we look into other LMC sightlines in which H_2 halo absorption may be present in the FUSE spectra. We emphasise the importance of the detection of molecular hydrogen in at least two cases in the IV gas, based on which we discuss the physical conditions and indications to small-scale structure at sub-pc scales in the H_2 IV gas.

6.2 The data

We used far-ultraviolet absorption-line data from the FUSE, of the background stars Sk-67°111, LH 54-425, Sk-67°107, Sk-67°106, Sk-67°104, and Sk-67°101 (see Fig. 5.1) to analyse the properties of the IVC and the HVC, found at the velocities $v_{\rm LSR} \simeq +57$ km s^{-1} and $v_{\rm LSR} \simeq +110$ km s^{-1}, respectively. For the stars Sk-67°107, Sk-67°106, Sk-67°104, and Sk-67°101 high-resolution STIS observations were also available. In total we cover the wavelength range 905-1730 Å (with some gaps due to the diversity of the instruments and detectors), where we can find most electronic transitions of many atomic species and molecular hydrogen. The typical S/N of the data varies for different detector channels and sightlines, being in general lower for the data from SiC channels (see Table 4.2 in Chapter 4). The data quality is significantly higher for all the FUSE detectors for the Sk-67°111 and LH 54-425 sightlines, because several observations were co-added. For detailed information about the data see Chapter 4.

The spectra was normalised by manually placing a continuum level in the surrounding of each absorption line. In the final analysis we paid special caution to the lines from part of the spectra where the continuum placement was less certain. The equivalent width of each absorption line was measured either by integrating the pixel to pixel area up to the continuum level, or by Gaussian fits with MIDAS ALICE (only for weak lines). A standard CoG method (Sect. 4.2.2) was used to derive the column densities $N\,[{\rm cm}^{-2}]$, and the Doppler parameter $b\,[{\rm km\,s}^{-1}]$ of the absorption by the different species. The uncertainties in the column densities include the errors in the equivalent-width measurements and the uncertainties in the b-values.

6.3 H_2 absorption in diffuse IV gas

6.3.1 H_2 absorption

We find a clear detection of H_2 at $v_{\rm LSR} \simeq +57$ km s^{-1} in the lines of sight towards Sk-67°111 and LH 54-425. Some of the H_2 absorption lines are shown in Fig. 6.1. The good data quality for these two stars make the equivalent-width measurements relatively unproblematic. In all cases with more than two data points, and when the data were not only located on the linear part of the CoG without any further information about the b-value, the values for $b = 1$ to 2 km s^{-1} were suitable. The many detected transitions of the $J = 1$ fit best to $b = 1.5$ km s^{-1}, which we adopted for all rotational levels (see Fig. 6.2 for the CoG of the various J-levels). This very low b-value implies that the H_2 probably arises in confined

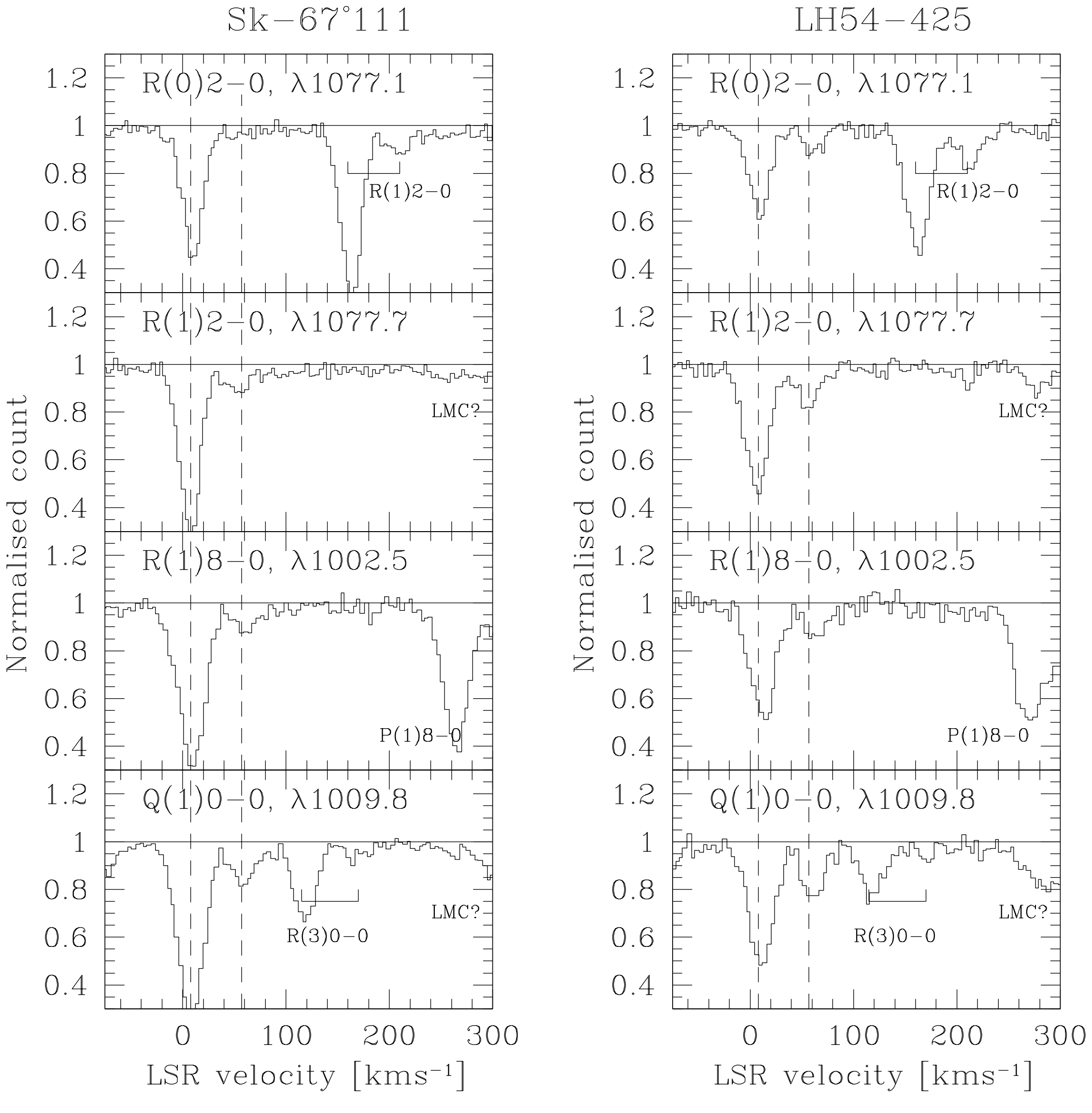

Figure 6.1: Selection of H_2 absorption lines in the sightlines Sk-67°111 (the left column) and LH 54-425 (the right column). The two dashed lines indicate the Galactic disc gas at $v_{\rm LSR} \simeq +8$ km s^{-1} and the IVC at $v_{\rm LSR} \simeq +57$ km s^{-1}. The H_2 transitions are named on top of each plot. Other absorption lines and their components are also labelled.

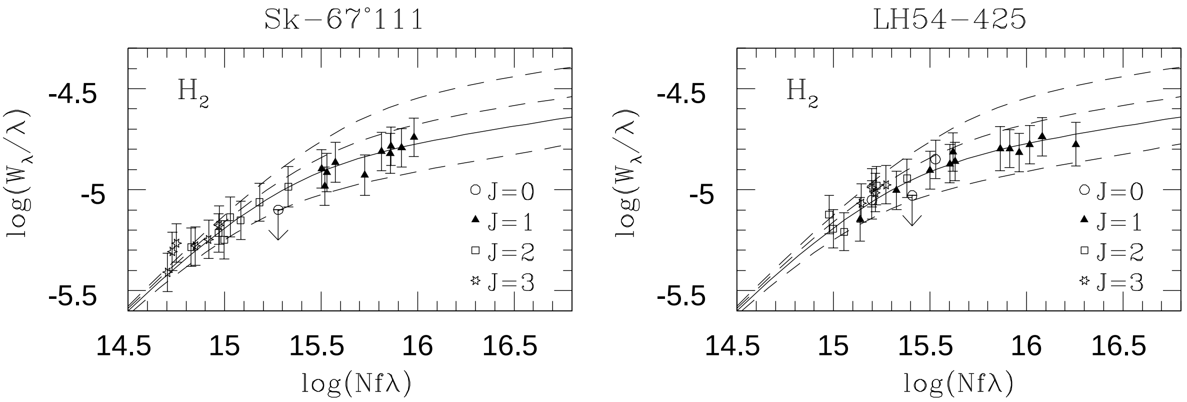

Figure 6.2: CoG for absorption by molecular hydrogen in the IVC towards Sk-67°111 (on the left) and LH 54-425 (on the right). The data from different J-levels (identified in the lower right corner) fit best on a CoG with b-value of 1.5 $\mathrm{km\,s^{-1}}$ (solid curve). The additional CoGs (dashed curves) are for $b = 1, 2,$ and 3 $\mathrm{km\,s^{-1}}$.

regions without strong interstellar turbulence, where it is self-shielded from the UV radiation field. The errors in the b-values (and thereby in the column densities) were derived individually for each level. The determination of the b-value of the higher rotational levels, in particular $J = 3$, has in all cases a large uncertainty. This is however not critical since the data points are on the linear part of the CoG, hence the errors in the derived column densities are small. All column densities and b-values derived are presented in Table 6.1.

Molecular hydrogen is possibly detected also in some of the other sightlines. There are a few features for absorption lines from lower J-levels with an equivalent width between $2\,\sigma$ to $3\,\sigma$ above the detection limit, but due to the weak profile of the line, together with the lower S/N of the spectra in these sightlines, it is difficult to confirm if all of these features actually are due to the H_2 absorption in the IVC. We have therefore derived upper limits in all these cases assuming $b \geq 1$ $\mathrm{km\,s^{-1}}$ (see Table 6.1).

6.3.2 H I column densities

To determine the fraction of molecules in the IV gas one needs to know the H I column densities along each line of sight. H I 21-cm data is available from the Parkes Galactic All-Sky Survey (GASS) (McClure-Griffiths et al. 2009; Kalberla et al. 2010), with a spatial resolution of $\sim 16'$. Fig. 6.3 shows the computed column density map (computed with CASA) for the IV gas in front of the LMC in the velocity range of 40 to 70 $\mathrm{km\,s^{-1}}$. The position of the stars towards which H_2 has been detected is marked in that figure. The column density map, as well as a Gaussian fit with $\Delta v_{\mathrm{FWHM}} \simeq 15$ $\mathrm{km\,s^{-1}}$ to the IVC emission line at $v_{\mathrm{LSR}} \simeq +50$ $\mathrm{km\,s^{-1}}$ in the extracted spectra, indicate $N(\mathrm{H\,I}) \simeq 3 \times 10^{18}$ $\mathrm{cm^{-2}}$.

However, in single-dish measurements emission from gas structures with limited spatial extent (less than the beam size) is averaged out over the telescope beam so that the 21-cm column density derived is only an approximation in comparison with column densities

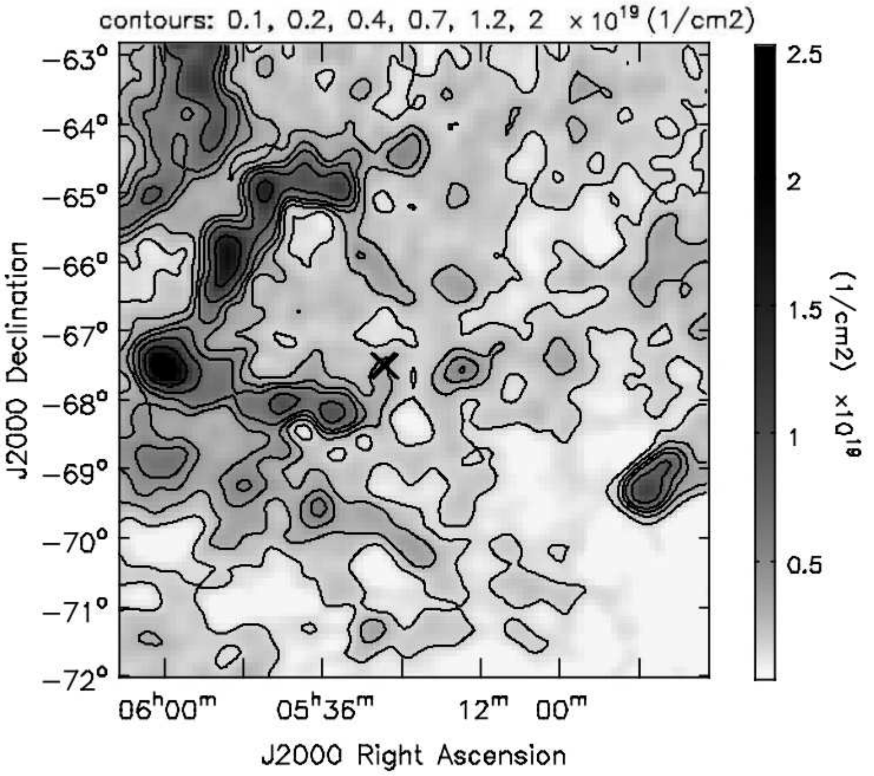

Figure 6.3: GASS H I 21-cm map for $v_{\rm LSR}$ = +40 to +70 km s^{-1} (on a rectangular grid). The map shows the IV gas present in front of the LMC. The contour levels refer to steps in column densities, indicated on top of the plot, with the first level starting at 3σ. The two overlapping crosses mark the position of Sk -67°111 and LH 54-425 at the coordinates RA: 05 26 48.00 Dec: −67 29 33.0, and RA: 05 26 24.25 Dec: −67 30 17.2 respectively.

from absorption-line data. Thus, the column density derived in this way does not give precise information on the N(H I) in our particular sightlines, and the possible deviation that might exist between these sightlines.

Another method to derive the H I column density is to use the absorption of O I. Because the H I and O I are coupled by charge exchange reactions, they have the same ionisation potential, and O I is not significantly depleted into dust, N(O I) is a reliable measure for the H I column densities. Assuming that this IV gas has a solar oxygen abundance[1], we derive the total neutral hydrogen column density along each line of sight, based on the respective column density of O I. This suggests N(H I) $\simeq 1.4$ to 3.5×10^{18} cm^{-2} (see Table 6.1), which is comparable with the GASS H I 21-cm data. Whether this small fluctuation in N(H I) is real or not is however dependent on the accuracy in the measured N(O I).

---

[1] $\log({\rm O/H})_\odot = -3.34$ (Asplund et al. 2005)

6.3.3 Metal absorption

There are absorption lines of N I, O I, Si II, P II, S II, Ar I, and Fe II detected in our FUSE and STIS spectra. Within our spectral range, there are more than five absorption lines of Fe II, and Si II detected in each line of sight. Fe II lines fit all on the linear part of the CoG, making the derivation of an accurate column density possible, but they do not give direct information of the Doppler parameter of the gas. On the other hand we detected both weak and strong Si II lines in our spectral range which fit on a CoG with $b = 11^{+2}_{-2}$ km s^{-1} towards Sk-67°101 and Sk-67°104, and $b = 10^{+2}_{-1}$ km s^{-1} towards Sk-67°106 and Sk-67°107. For LH 54-425 and Sk-67°111 we have no STIS data available, and therefore only one detected Si II absorption. For each of these two lines of sight we adopt the b-value of the nearest sightline, for which the b-value is known (i.e., the line of sight towards Sk-67°107). The column densities of N I, O I, P II, S II, Ar I, and Fe II were derived based on the corresponding Si II-CoG. All column densities and b-values are listed in Table 6.1. It is possible that the b-values of the neutral species are slightly lower than the one derived from Si II, depending on the ionisation structure of the gas. This is in fact implied by the N I data points towards Sk-67°106 and Sk-67°107, which make a better fit on a CoG of $b \approx 5$ km s^{-1}. This b-value would lead to an increase of $\log N(\mathrm{O\,I})$ by ~ 0.3 dex (with the strong λ1302.2-line as an outlier). However, we do not have enough information to fix a b-value from the N I, or O I-lines, and therefore adopted the Si II-CoG for all sightlines.

The possible C I absorption in the IVC is, unfortunately blended by the local Galactic C I* gas. There is no convincing way to establish detection of the C I in the IVC, as the equivalent widths of these blended lines are in good agreement with the the rest of the Galactic foreground C I* absorption lines in the CoG analysis.

The relative abundances[2] suggest a partly photoionised gas. O I and H I have the same ionisation potential, lower than the ionisation potential of e.g., Si II, P II, and S II. While silicon is probably partly depleted into dust grains, the phosphor and oxygen, and sulfur and oxygen abundance ratio is expected to be mainly affected by the ionisation structure of the gas. For all these ions we observe high abundances relative to solar, with a slight variation between our six lines of sight: $+0.7 \leq$ [P II/O I] $\leq +1.1$, $+0.35 \leq$ [Si II/O I] $\leq +0.75$, and $+0.6 \leq$ [S II/O I] $\leq +0.9$ (only in sightlines with measured $N(\mathrm{S\,II})$). These ratios are furthermore slightly higher in the direction of Sk-67°104, and partly towards Sk-67°101. This abundance pattern suggests that a substantial amount of the oxygen (and thus of the hydrogen) in the IV gas is in the ionised form, possibly with a higher ionisation fraction towards Sk-67°104 (and Sk-67°101).

6.3.4 The physical properties of the H_2 IV gas

The column densities of the different rotational levels of molecular hydrogen reveal the kinetic temperature of the gas, as well as the nature of the UV radiation field. In Fig. 6.4 we have plotted the column density of H_2 in level J, divided by the statistical weight g_J,

---

[2] [X/O I] = log(X/O I) − $\log(\mathrm{X/O})_\odot$, with X being the detected ion, and the solar abundances taken from Asplund et al. (2005).

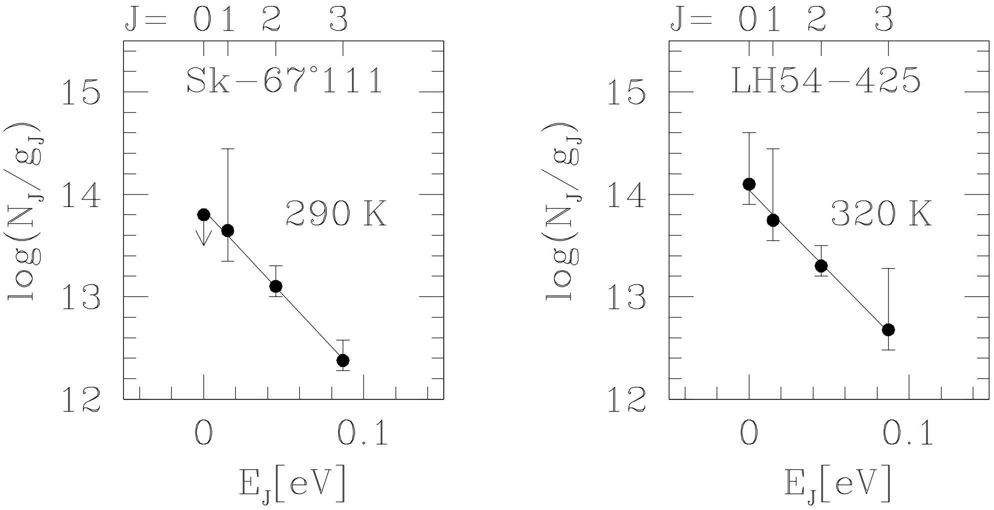

Figure 6.4: Rotational excitation of the H$_2$ gas in the IVC towards Sk -67°111 (on the left) and LH 54-425 (on the right). The Boltzmann excitation temperature is represented by a single line with $T_{\rm exc} = 290\,$K for the IV gas towards Sk -67°111, and $T_{01} = 320\,$K towards LH 54-425.

against the rotational excitation energy E_J. These data can be fitted with a single line, representing a Boltzmann distribution with the temperature $T_{0,3} \simeq 300\,$K. Given the low column densities the lower J-levels might be partly excited by UV-pumping from the UV-radiation field, or by the UV photons emitted in the formation process of H$_2$. Therefore this $T_{0,3}$ does not necessarily represent the kinetic temperature of the gas, but rather is an upper limit for it. Furthermore, considering the low b-value, the kinetic temperature of the gas should be lower than 270 K, if also turbulence contributes to the Doppler broadening of the H$_2$-lines.

Based on the indirect measure of N(H I) in the previous Section we estimate the hydrogen in molecular form: $f = 2N(\mathrm{H_2})/(N(\mathrm{H\,I}{+}2N(\mathrm{H_2}))$ to be 0.6×10^{-3} in the direction of Sk -67°111, and 0.7×10^{-3} in the direction of LH 54-425. This fraction of hydrogen in molecular form is similar to the fractions found in most of the other diffuse H$_2$ clouds in IVCs (Richter et al. 2003b).

The low fraction of molecular hydrogen, the low column density of the gas, and the derived excitation temperature mentioned above, all indicate inefficient line self-shielding. Given the short timescale for the H$_2$ destruction ($\sim$ 1000 years), it is reasonable to assume that the molecular hydrogen forms on dust grains in the halo, or else the diffuse H$_2$ gas would have been dissociated and not observed, as it often has been in the IVCs (Richter et al. 2003a,b). Thus, we here on assume that the H$_2$ is in formation-dissociation equilibrium. Instead of using the Eq. (3.5) in Chapter 3, for relating the H$_2$ volume density, $n(\mathrm{H_2})$, to the one of H I, n(H I), we follow below the approximations by Richter et al. (2003b) (see that paper for more details). This is because the parameters assumed for the Galactic disc gas may differ from the ones expected from the halo. The photoabsorption rate at the edge of the cloud, $\beta_{0,\mathrm{halo}}$, for one, depends on the FUV radiation field, which is expected to decrease with the scale height z above the Galactic plane (Wolfire et al. 1995), thus be lower in the halo of the Milky Way compared to the disc. Using the scaling relations for the radiation field in the halo as a function of the z height by Wolfire et al. (1995), Richter et al. (2003b) estimated the FUV radiation field to be reduced by a factor of 2 at $z \sim 1$ kpc, and not change significantly for the lower Galactic halo, because of the large solid angle of the Galactic plane. Consequently, the photoabsorption rate at the edge of the cloud is assumed to be reduced to $\beta_{0,\mathrm{halo}} \approx 0.5\,\beta_{0,\mathrm{disc}} = 2.5 \times 10^{-10}$ s^{-1} ($\beta_{0,\mathrm{disc}}$ is the typical value for photoabsorption rate at the edge of the cloud in Galactic disc environment, from Draine & Bertoldi 1996). Assuming that all of the H_2 in the halo IV gas forms on the surface of dust grains, we also adopt $R_{\mathrm{halo}} \approx R_{\mathrm{disc}} = 3 \times 10^{-17}$ cm^3 s^{-1} (Draine & Bertoldi 1996). This is however, an assumption due to the lack of further knowledge on the dust properties in the halo, which may or may not be similar to the ones in the Galactic disc. One other unknown property which heavily affects the relation in Eq. (3.5), is the unknown relation between the volume densities and the measured column densities. As also discussed in Chapter 5, there is an uncertainty in assuming that the volume densities are linearly related to the measured column densities, and that the total $N(\mathrm{H\,I})$ measured along a line of sight is physically connected with the $N(\mathrm{H_2})$. The Galactic halo gas in particular, consists of a complex multi-phase structure, with the CNM likely embedded in a large low-density gaseous envelope of both ionised and neutral gas. While the $N(\mathrm{H\,I})$ is the sum of H I atoms along a line of sight from all neutral gas phases, the H_2 likely resides only in the cooler and more confined regions, where only a fraction of the observed $N(\mathrm{H\,I})$ is available. Therefore, Richter et al. (2003b) define a scaling factor ϕ (with a value ≤ 1), in order to relate the volume density of partly molecular gas to the total column densities observed. With that, and the approximations above, they reformulate the Eq. (3.5) to describe the density of the confined region, $n_{\mathrm{H,\,mol}}$ (here we use the subscript mol for the molecular structure), where the H_2 is located

$$n_{\mathrm{H,\,mol}} \approx 9.2 \times 10^5 N(\mathrm{H_2}) N(\mathrm{H\,I})^{-1} \phi^{-1} \,. \tag{6.1}$$

Due to the unknown physical structure of the IVC, it is difficult to estimate an accurate value for ϕ. However, given the fact that the $b = 11$ km s^{-1} derived for metals is much higher than the $b = 1.5$ km s^{-1} derived for the H_2, we believe that it is appropriate also here to assume that the H_2 gas resides in a more confined region associated with the cold neutral medium (CNM), surrounded by a more extended lower density envelope of warm neutral medium (WNM), of which we observe the metal absorption with the high b-values, and the total $N(\mathrm{H\,I})$. Due to the lack of further information, we adopt the $\phi = 0.5$ from Richter et al. (2003b). This gives us the derived volume densities $n_{\mathrm{H,\,mol}} = 530$ cm^{-3} towards Sk-67°111, and $n_{\mathrm{H,\,mol}} = 670$ cm^{-3} towards LH 54-425, for the structure containing molecular hydrogen, and the pathlengths of $D_{\mathrm{mol}} = \phi\, N(\mathrm{H\,I})/n_{\mathrm{H,\,mol}} \simeq 100$ AU in both cases. If we need to take into account the self-shielding, these $n_{\mathrm{H,\,mol}}$ would be reduced by a factor of 3-5. Considering the low column densities however, this is unlikely.

Table 6.1: Logarithmic column densities log N (N in cm^{-2}) and b-values [km s^{-1}] for IVC towards six LMC stars.

	Sk -67°111		LH 54-425		Sk -67°107		Sk -67°106		Sk -67°104		Sk -67°101	
Species	b	log N	b	log N	b	log N	b	log N	b	log N	b	log N
$H_2(J=0)^{\rm F}$	≥ 1	≤ 13.8	$1.5^{\rm a}_{-0.5}$	$14.1^{+0.5}_{-0.2}$	≥ 1	≤ 14.6	≥ 1	≤ 14.7	≥ 1	≤ 14.4	≥ 1	≤ 14.6
$H_2(J=1)^{\rm F}$	$1.5^{+1.5}_{-0.5}$	$14.6^{+0.8}_{-0.3}$	$1.5^{+0.5}_{-0.5}$	$14.7^{+0.7}_{-0.2}$		≤ 14.8		≤ 14.3		≤ 15.3		≤ 14.4
$H_2(J=2)^{\rm F}$	$1.5^{\rm a}_{-0.5}$	$13.8^{+0.2}_{-0.1}$	$1.5^{+2.5}_{-0.5}$	$14.0^{+0.2}_{-0.1}$		≤ 14.5		≤ 14.2		≤ 14.0		≤ 14.5
$H_2(J=3)^{\rm F}$	$1.5^{\rm a}_{-0.5}$	$13.7^{+0.2}_{-0.1}$	$1.5^{\rm a}_{-0.5}$	$14.0^{+0.6}_{-0.2}$		≤ 14.3		≤ 14.3		≤ 14.0		≤ 14.1
H_2(total)		$14.7^{+0.2}_{-0.2}$		$14.9^{+0.6}_{-0.2}$		≤ 15.2		≤ 15.0		≤ 15.4		≤ 15.0
Si II$^{\rm FS}$	10^{+2}_{-1}	$14.2^{+0.1\rm b}_{-0.1}$	10^{+2}_{-1}	$14.2^{+0.1\rm b}_{-0.1}$	10^{+2}_{-1}	$14.5^{+0.1}_{-0.2}$	10^{+2}_{-1}	$14.5^{+0.1}_{-0.1}$	11^{+2}_{-2}	$14.4^{+0.5}_{-0.2}$	11^{+2}_{-2}	$14.3^{+0.1}_{-0.1}$
N I$^{\rm FS}$		$14.2^{+0.1}_{-0.1}$		$14.2^{+0.1}_{-0.1}$		$14.0^{+0.1}_{-0.1}$		$14.0^{+0.1}_{-0.1}$		$13.6^{+0.1}_{-0.1}$		$13.6^{+0.1}_{-0.1}$
O I$^{\rm FS}$		$14.9^{+0.1}_{-0.1}$		$15.0^{+0.1}_{-0.1}$		$15.2^{+0.2}_{-0.1}$		$15.2^{+0.2}_{-0.1}$		$14.8^{+0.2}_{-0.1}$		$14.9^{+0.2}_{-0.1}$
P II$^{\rm F}$		$12.6^{+0.1\rm b}_{-0.1}$		$12.7^{+0.1\rm b}_{-0.1}$		$12.6^{+0.2\rm b}_{-0.1}$		$12.6^{+0.1\rm b}_{-0.1}$		$12.6^{+0.1\rm b}_{-0.2}$		$12.6^{+0.1\rm b}_{-0.2}$
S II$^{\rm S}$		-		-		$14.3^{+0.1}_{-0.1}$		$14.3^{+0.1}_{-0.1}$		$14.2^{+0.1}_{-0.1}$		$14.0^{+0.1}_{-0.1}$
Ar I$^{\rm F}$		$12.7^{+0.1\rm b}_{-0.1}$		$13.0^{+0.1\rm b}_{-0.1}$		$12.7^{+0.1\rm b}_{-0.1}$		$12.7^{+0.1\rm b}_{-0.1}$		$< 12.5^{\rm c}$		$< 12.6^{\rm c}$
Fe II$^{\rm FS}$		$13.8^{+0.1}_{-0.1}$		$13.8^{+0.1}_{-0.1}$		$13.5^{+0.1}_{-0.1}$		$13.6^{+0.1}_{-0.1}$		$13.7^{+0.1}_{-0.1}$		$13.5^{+0.1}_{-0.1}$
H I$^{\rm d}$	-	18.2	-	18.3	-	18.5	-	18.5	-	18.1	-	18.2

Table 6.2: Logarithmic column densities log N (N in cm^{-2}) and b-values [km s^{-1}] for HVC towards six LMC stars.

	Sk -67°111		LH 54-425		Sk -67°107		Sk -67°106		Sk -67°104		Sk -67°101	
Species	b	log N	b	log N	b	log N	b	log N	b	log N	b	log N
O I$^{\rm FS}$	14^{+3}_{-6}	$15.2^{+0.1}_{-0.1}$	14^{+3}_{-6}	$15.1^{+0.2}_{-0.1}$	14^{+3}_{-2}	$15.3^{+0.2}_{-0.1}$	14^{+3}_{-2}	$15.3^{+0.1}_{-0.1}$	14^{+3}_{-2}	$15.4^{+0.1}_{-0.1}$	14^{+3}_{-2}	$15.3^{+0.1}_{-0.2}$
Si II$^{\rm FS}$		$14.3^{+0.1}_{-0.1}$		$14.2^{+0.1}_{-0.1}$		$14.5^{+0.2}_{-0.2}$		$14.5^{+0.2}_{-0.2}$		$14.9^{+0.7}_{-0.4}$		$14.7^{+0.2}_{-0.4}$
Fe II$^{\rm FS}$		$14.1^{+0.1}_{-0.1}$		$14.0^{+0.1}_{-0.1}$		$14.2^{+0.1}_{-0.2}$		$14.2^{+0.1}_{-0.1}$		$14.3^{+0.1}_{-0.1}$		$14.1^{+0.1}_{-0.1}$

[a] The upper error is high, but does not influence the uncertainty in derived N.
[b] Based on one absorption line.
[c] The 3σ upper limit for $b > 2$ km s^{-1}.
[d] Derived from O I and $(\mathrm{O/H})_\odot = -3.34$ (Asplund et al. 2005) (see Sect. 6.3.2).
[F] Based on FUSE data only.
[S] Based on STIS data only.
[FS] Based on both FUSE and STIS for Sk -67°107 to Sk -67°101.

6.4 The HVC

HV gas at velocities > 100 km s^{-1} towards LMC has been known for many years (Savage & de Boer 1979). We detect also a HV component at $v_{\rm LSR} \simeq +110$ km s^{-1} in all of our sightlines. Molecular hydrogen has occasionally been detected in HVCs in other directions (Richter et al. 1999; Richter et al. 2001; Sembach et al. 2001). In the HV gas in our studied lines of sight however, we do not detect any molecular hydrogen. H_2, if it exists should have a column density below the detection limit. An estimated 3σ upper limit[3] is $\log N(H_2) < 13.7$ towards LH 54-425 and Sk-67°111 with a higher S/N, and $\log N(H_2) < 14.2$ on average, for the rest of the sightlines.

In the STIS spectra some of the Si II and Fe II lines are resolved into two components at $v_{\rm LSR} \simeq +95$ and $v_{\rm LSR} \simeq +120$ km s^{-1}. Most of the absorptions in the FUSE, or the STIS spectra however, are impossible to deblend in an accurate manner. Therefore, we have measured the equivalent widths as a sum of both of the components. This might lead to a higher derived b-value for the species that have both of the components present, as the stronger components sample more gas than the weak ones, but it does not have a significant effect on the derived total column densities. This might for example be the case for Si II-lines. Si II has some strong (almost saturated) absorption lines in STIS, and only one weaker absorption in FUSE spectra. The weaker absorption (at 1020.7 Å) is much lower on the CoG than the rest of the Si II-lines, which leads to unsatisfying fits to the CoG.

The b-value is best derived from the O I lines, even though most of the O I data points are located on the linear part of the CoG. The strong 1302-line is located on the flat part, which makes the derivation of a b-value straightforward. This line is however not available for LH 54-425 and Sk-67°111. Therefore, the errors in b are larger in these lines of sight.

Fe II is also detected in a number of transitions, but these are mainly on the linear part of the CoG of $b > 11$ km s^{-1}. We have thus, in the lack of further information on the Doppler parameter of the individual species, derived all the column densities presented in Table 6.2 based on the corresponding O I-CoG ($b = 14$ km s^{-1}).

Our derived column densities agree well (within the errors) with the ones derived by Lehner et al. (2009), who have studied the HVCs towards 139 LMC stars, including the ones studied in this work. They find on average $[{\rm O/H}] \simeq -0.51$, with no significant variations between the sightlines. This value is close to the present-day oxygen abundance of the LMC. Lehner et al. (2009), conclude that the HVCs in their studied LMC lines of sight are highly ionised, have multi-phase structures, and likely are part of the same complex, with properties that can be explained by an energetic outflow from the LMC. We refer the interested reader to that paper for a detailed analysis.

---

[3] by fitting $W_{\lambda,3\sigma}$ for the strongest transitions to the CoG of 1 km s^{-1}.

6.5 Discussion

The relatively high densities derived for the IVC, $n_{\rm H} = 530$ cm^{-3} towards Sk -67°111, and $n_{\rm H} = 670$ cm^{-3} towards LH 54-425, and small pathlengths of $D_{\rm mol} \simeq 100$ AU, suggest that the H_2 is situated in small dense structures embedded in a diffuse halo gas. This is similar to what has been found towards Sk -68 80 (~1.3 degrees away from our sightlines, at RA: 05 26 30.3 Dec: -68 50 25.4) by Richter et al. (2003a).

While H_2 absorption now has been detected in a number of IVCs in the Milky Way halo (Gringel et al. 2000; Richter et al. 2003a,b), the H_2 absorbing clumps in the IVC towards LMC stand out, as these structures are embedded in diffuse gas with H I column density ($N(\text{H I}) \approx 10^{18}$ cm^{-2}) about 1 to 2 orders of magnitude lower than what is typically found in H_2 absorbing regions in IVCs (see Richter et al. 2003b). Our study in this Chapter further demonstrates the existence of substantial small-scale structure and density contrasts in the Galactic halo gas even at very low neutral gas column densities.

The excitation temperatures of $T = 290$ and 300 K that we have derived for the H_2 absorbing gas represent upper limits for actual kinetic gas temperature. Consequently, the estimates of the thermal pressure in the gas represent upper limits as well. However, even if we assume that the H_2 gas in the IVC has a temperature of just 50 K, as derived for the SK -68 80 sightline by Richter et al. (2003a), the thermal pressures are $p/k = 2.7 \times 10^4$ and 3.4×10^4 K cm^{-3} and thus a factor of ~ 5 above what is most likely the mean pressure ($p/k \simeq 3000$ to 10^4 K cm^{-3}, Wolfire et al. 1995) in the disc. Assuming that the IV gas is located at a z-height of 2 to 5 kpc and in pressure equilibrium (Schwarz & de Boer 2004), this expected pressure could be even smaller by a factor of 2. Such small, dense overpressured structures thus should not be able to survive over longer timescales.

Turbulent pressure in the gas, however, could dominate the pressure balance in those tiny structures (see, e.g., Heiles 1997) and may stabilise them against immediate evaporation. As has been shown by numerical simulations of Galactic fountain flows (e.g., de Avillez & Breitschwerdt 2007) the simplified assumption of an H I IVC being a cool fountain cloud residing in pressure equilibrium with a surrounding hot medium may be invalid after all, as strong turbulence produced by supernova-driven outflows from the disc obviously favours the formation of short-lived small, dense structures in the gas. High-density gas clumps in the disc-halo interface thus may represent transient structures rather than stable clouds. However, the timescale for H_2 formation of $t_{\rm form} = (R\, n_{\rm H})^{-1} \geq 10^6$ yr (with $R \leq 3 \times 10^{-17}$ cm^3 s^{-1} being the H_2 formation coefficient in the IVC), is possibly much longer than the characteristic life time of such transient turbulence-driven structures. Thus, it is plausible that the observed H_2 absorbing clumps in the IVC towards the LMC were formed in an originally larger IVC, and may represent high-density fragments left over from a recent breakup, possibly caused by ram-pressure stripping and other instabilities. As can be seen in the H I 21-cm map, the overall region in this field shows a number of scattered H I 21-cm clouds that are located only a few arcminutes away from our LMC sightlines. The close match in both radial velocity and sky position suggests that these 21-cm features are physically connected with the intermediate-velocity absorption towards the LMC presented here and that all these small clumps may have been part of a more coherent gas structure in earlier times.

To better understand the physical conditions in this and other IVCs in the disc-halo interface of the Milky Way it would be of great importance to implement the grain formation and photodissociation of H_2 in numerical simulations of Galactic fountain flows and Galactic winds. In addition, optical spectra at very high spectral resolution for the LMC sightlines in which IVC H_2 absorption have been detected would be very useful to further constrain gas temperatures and turbulence in the gas from the measured line widths of low-ionisation species such as Ca II and Na I (see also Welty et al. 1999).

Chapter 7

Halo Na I and Ca II absorbers, and small-scale structures in the Milky Way

In this Chapter, Galactic halo absorption by Na I, *and, if available,* Ca II, *is analysed in optical spectra of QSOs recorded with the* KECK *high-resolution spectrograph. From the original sample of 42 QSO spectra only 6 showed to be suitable for the search of the Galactic* Na I *lines (and 2 for supplementary* Ca II*), in all of which halo* Na I (Ca II) *absorbers (with low and/or high LSR velocities) were detected. Comparison between the* Na I (Ca II) *absorbers and the* H I *21-cm emission from the EBHIS or LAB surveys unveils the presence of substructures in the diffuse halo gas. An estimate of the physical properties of these absorbers with the current information is, however, not possible. Instead, we compare these structures to the ones detected by* H_2 *absorption in this work and other studies, and study the constraints on small-scale structure through the distribution of* Na I *and* H_2 *in disc and halo of the Milky Way.*

7.1 Introduction

There has been major progress in the last decades in revealing the complex, multi-phase gaseous halo surrounding the Milky Way. While large H I surveys map the overall distribution of the neutral gas in the inner and outer halo of the Galaxy, absorption-line spectroscopy provides a sensitive method to study the neutral and partly ionised gas down to column densities that are far below the detection limit of the current H I single-dish 21-cm surveys. As it is clear from the previous Chapters, the FUV and UV spectral range is profitable for studying the physical properties of the gas through the absorption by a large number of species, including molecular hydrogen. Such absorption-line studies are, however, limited by the number of sufficiently bright background sources in that wavelength range, mostly being nearby bright stars. Ground-based optical high-resolution data of distant QSOs in addition are widely available, and used for different purposes of studying the gas in the disc and the halo of the Milky Way, as well as the halo of other Galaxies, the IGM, and the QSO itself. Among the most important transitions that can be found within the optical spectral range are the doublets of Na I (at 5891.6 and 5897.6 Å) and Ca II (at 3934.8 and 3969.6 Å). With ionisation potentials of 5.1 respective 11.9 eV, both of these species are sensitive tracers of neutral gas in the interstellar medium, with Na I serving as a tracer of mainly cold gas, and Ca II of both cold and warm regions.

In previous studies with high-resolution optical telescopes with high S/N, a large number of halo Ca II and Na I systems have been detected in various lines of sight towards QSO background sources. These are likely to arise from neutral and partly ionised gas in the halo of the Milky Way. The detection frequency of these absorbers indicates that the Milky Way halo contains a large number of low-column density absorbers (Richter et al. 2005, 2009; Ben Bekhti et al. 2008; Wakker et al. 2008).

Combined with follow-up H I observations, Ca II and Na I absorption lines provide an additional tool to study the properties and small-scale structure of neutral and weakly ionised gas in the inner and outer halo of the Milky Way. In this Chapter we analyse some additional QSO sightlines that are not yet discussed in the literature, for which we search for these low-column density absorbers, and discuss the overall gas structure, based on the available information.

At the end of this Chapter, we compare these structures to the ones detected by H_2 absorption and discuss the distribution of the Na I and H_2 absorbers in the disc and the halo of the Milky Way, including previous results in the literature. Based on the column-density distribution of these absorbers, we study the possible constraints on small-scale structure.

7.2 Na I and Ca II halo absorbers and H I 21-cm counterparts

In this Section we analyse the Galactic halo absorption by Na I, and, if available, by Ca II in QSO spectra from the High Resolution Echelle Spectrometer (HIRES) at KECK Observatory. For those lines of sight with detected Na I and/or Ca II halo absorbers, we also search for emission in H I 21-cm in the Effelsberg-Bonn H I survey (EBHIS) (Winkel et al. 2010; Kerp et al. 2011), or the Leiden-Argentine-Bonn (LAB) survey (Kalberla et al. 2005). See Chapter 4 for detailed information on the data.

A sample of 42 pre-reduced and normalised QSO spectra, observed with the KECK HIRES, were originally available (from Prochaska et al. 2007), spread over different Galactic directions. Due to limitations by the instrument (see Sect. 4.1.2), only 6 QSOs from the original sample were useful for the study of Galactic Na I doublets ($\lambda 5891.6, \lambda 5897.6$), and only 3 of them for Ca II ($\lambda 3934.8, \lambda 3969.6$). In the 6 QSO spectra that were selected, we found Na I absorbers. Among the 3 QSO spectra with spectral range in the location of Ca II lines, only one was suitable for analysis of the Ca II absorption, in which we found Ca II counterparts for the detected Na I absorbers.

Galactic IVC and HVC components were identified by the $v_{\rm LSR}$ of the Na I and/or Ca II doublets (see Chapter 1 for distinction between IVCs and HVCs) in the range of $-200 < v_{\rm LSR} < +200$ km s^{-1}. The spectra of the 6 QSOs are plotted in a LSR velocity scale for Na I (and Ca II) lines in Fig. 7.1, and Fig. 7.3 - 7.7. For those sightlines with both suitable Na I and Ca II, the velocities of these absorbers could be compared. It is not always straightforward to distinguish between the absorption from the halo gas and absorption due to the local disc gas, as these can both have low LSR velocities. Therefore, we used a kinematic model for the Milky Way from Kalberla (2003) and Kalberla et al. (2007), which determines for given Galactic coordinates the velocities that are expected from interstellar gas following the Galactic disc rotation. These velocity ranges are marked in Fig. 7.1, and Fig. 7.3 - 7.7 with solid lines. Based on these velocity ranges, we distinguished between Na I and Ca II absorbers that belong to the disc of the Milky Way and those in the halo IVCs and HVCs. For a positive detection, a significance of 5σ for the equivalent width of the stronger line of the doublets, and 3σ for the weaker one was required (1σ equivalent width, $W_{\lambda,1\sigma}$, being defined in Sect. 4.2.4). The column densities and b-values of the selected absorbers were determined by simultaneously fitting Voigt profiles to each of the Na I (Ca II) doublets using the software package FITLYMAN (the method is described in Chapter 4). The results are presented in Table 7.1. When it was necessary, local re-normalisation of the spectra was done with SPECTRALYSOR before the column density was derived. Such cases are marked in Table 7.1. There are furthermore a number of weak absorption features that may be Na I and Ca II absorptions, for which the weaker doublet line is too weak or even is not detected in some cases. We have also considered these weaker lines as possible detections, with the requirement that the stronger line has an equivalent width above $W_{\lambda,4\sigma}$. These possible Na I and Ca II candidates are presented as upper limits in Table 7.1, based on the equivalent width of the stronger line and assuming $b = 1$ km s^{-1}.

For all 6 sightlines with detected Na I and/or Ca II halo absorbers we searched for associated H I emission. The data from EBHIS were considered in first hand, being observed with a smaller beam size and having a better sensitivity. For those sightlines where Effelsberg observations were not yet available, the H I 21-cm data from the LAB survey (Kalberla et al. 2005) have been used to search for H I emission associated with the detected Na I (Ca II) features in those lines of sight. The H I column densities were obtained using Eq. (2.24), and by fitting Gaussian profiles to the emission lines with the MIDAS package ALICE. For available data cubes (from EBHIS), the column densities could also be obtained directly from the column density maps (computed with CASA), integrated for the velocity range in which the gas was visible. As a detection criteria, we have only considered features above the 3σ noise level, with 1σ noise level varying between 50 mk to 100 mk for the different EBHIS and LAB data. Assuming the noise to be Gaussian for a line width of 10 km s^{-1}, this corresponds to a 3σ column density limit of 3 to 6×10^{18} cm^{-2}. Based on the 1σ noise statistics, we estimate the typical errors in N(H I) to be about 1 to 2×10^{18} cm^{-2}.

The IV and HV Na I (Ca II) components and their H I 21-cm counterparts are presented for the different QSO sightlines in the following Subsections.

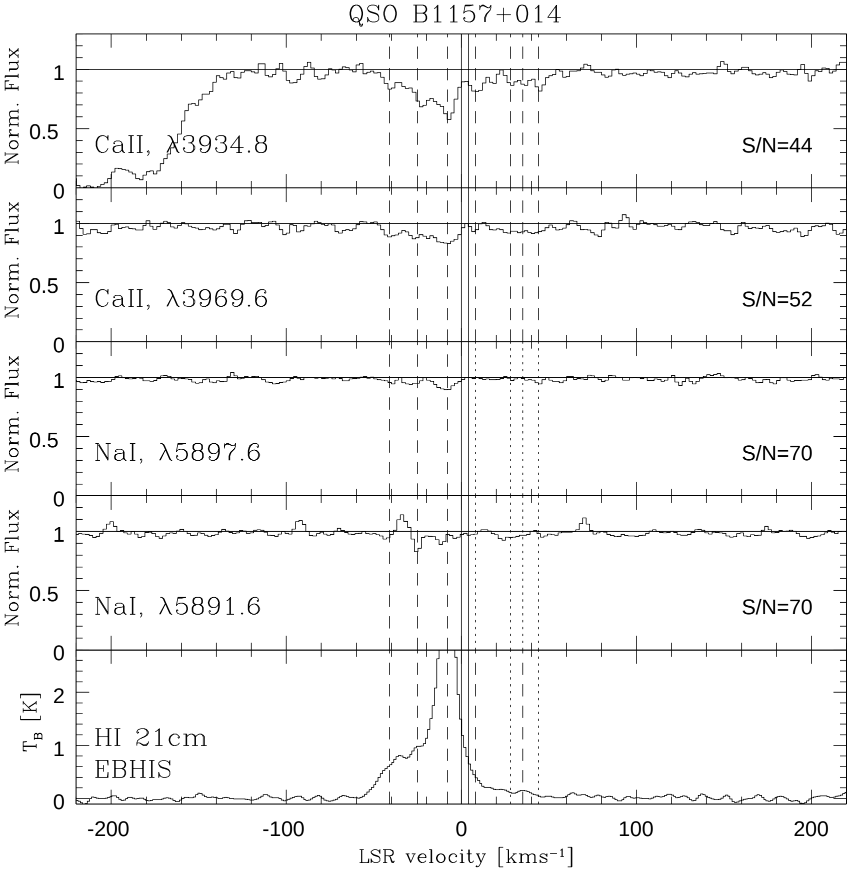

Figure 7.1: Ca II (at 3934.8, and 3969.6 Å) and Na I (at 5897.6 and 5891.6 Å) absorptions in the KECK HIRES spectrum and H I 21-cm emission obtained from EBHIS, towards QSO B1157+014, plotted on a LSR velocity scale. The absorbers are marked with dashed lines for clear detections, and dotted lines for possible detections. The solid lines mark the velocity range which is expected from the local disc gas, according to the model by Kalberla (2003) and Kalberla et al. (2007) (see Sect. 7.2). The average S/N for the relevant part of the spectrum is also indicated in the figure.

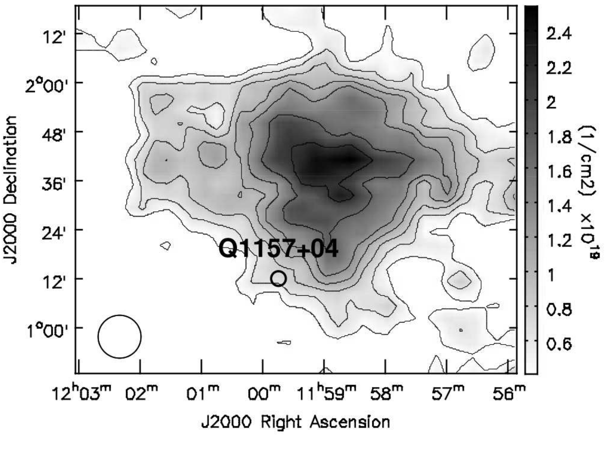

Figure 7.2: EBHIS H I 21-cm column density map, integrated for $v_{\rm LSR}$ = +20 to +60 km s^{-1}. The contour levels (starting at 3σ) refer to $N = 0.4, 0.6, 0.8, 1.1, 1.3, 1.7, 2.1 \times 10^{19}\,{\rm cm}^{-2}$. The line of sight towards QSO B1157+014 is marked with open circle, passing through the outer envelope of a low column density gas clump. The beam size of $9'$ is indicated (open circle) in the lower left corner.

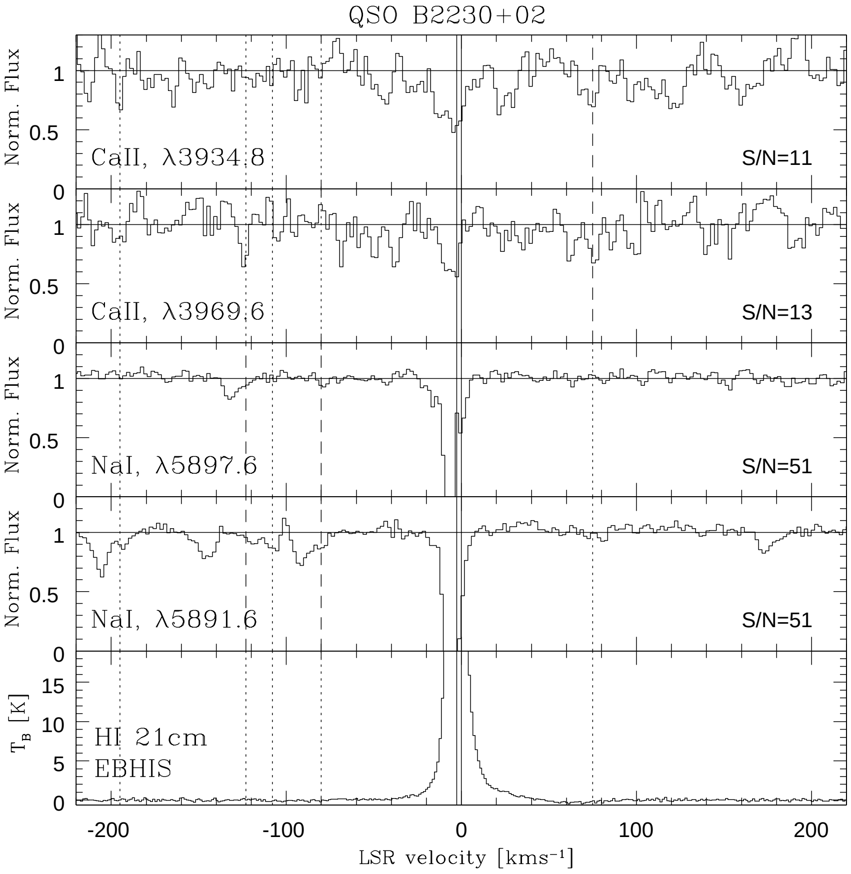

Figure 7.3: As Fig. 7.1, but towards QSO B2230+02.

7.2.1 QSO B1157+014

In Fig. 7.1 the spectrum of QSO B1157+014 is shown on a velocity scale for the absorption by interstellar Na I and Ca II, together with the corresponding H I 21-cm emission towards that line of sight, from the Effelsberg-Bonn H I Survey (EBHIS).

Both Na I and Ca II show multi-component structure at low and intermediate velocities, $-50 < v_{\rm LSR} < +50$ km s^{-1}. The Na I and Ca II absorbers at $v_{\rm LSR} \simeq -25$ and $v_{\rm LSR} \simeq -41$ km s^{-1} have associated H I emission in the EBHIS data, which can be decomposed into two components by fitting a multi-component Gaussian fit to the H I spectra, i.e., considering the emission at $v_{\rm LSR} \simeq -7$ and $v_{\rm LSR} \simeq +5$ km s^{-1} in addition (associated with the Na I and Ca II at $v_{\rm LSR} = -8$ and $v_{\rm LSR} = +8$ km s^{-1}, respectively). The associated H I IV components peak[1] at $v_{\rm LSR} \simeq -19$ and $v_{\rm LSR} \simeq -39$ km s^{-1}, and have column densities of $\log N(\text{H I}) = 19.67$, and $\log N(\text{H I}) = 19.22$, respectively. Based on the coordinates and velocities, the latter two components may be associated with the IV-Spur. The components at $v_{\rm LSR} = -8$

---

[1] The velocities of the H I components are given based on the peak of the fitted Gaussian profile, and slightly differ from the velocity of Na I and Ca II counterparts.

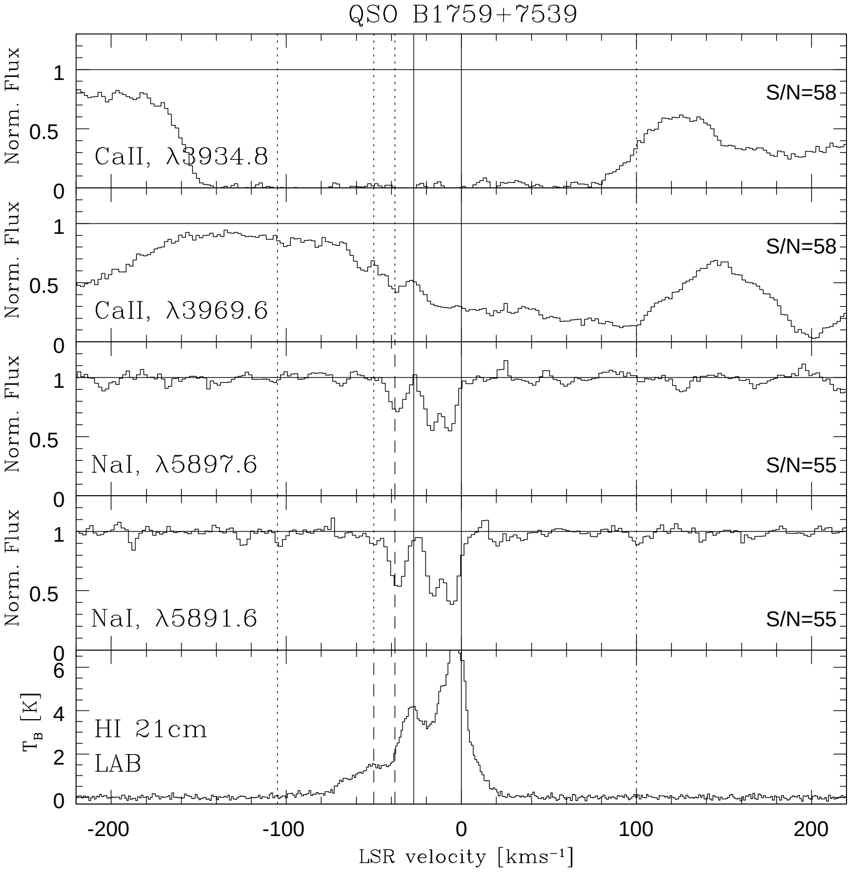

Figure 7.4: As Fig. 7.1, but towards QSO B1759+7539. The H I emission spectrum was retrieved from the LAB survey.

and $v_{\rm LSR} = +8$ have both low LSR and low deviation velocities, based on which they can be low velocity clouds, connected to the Galactic disc gas, or in the disc-halo interface.

While the Ca II lines show multi-components in the range of $v_{\rm LSR} \simeq +28$ to $+44$ km s^{-1}, the diffuse intermediate velocity wings of the strong H I emission can not be separated into different IVC components. Having access to the data cube from EBHIS, we computed with CASA the column density map for the velocity range for which the corresponding H I gas can be seen. This integrated map is shown in Fig. 7.2, for the velocity range of $v_{\rm LSR} \simeq +20$ to $+60$ km s^{-1}, and for a larger area on the sky. The line of sight towards QSO B1157+014 is marked in that figure; it passes through what appears to be the outer envelope of a low column density gas clump. We obtain $\log N(\text{H I}) = 18.81$ for the position of the QSO. The clump itself has a peak logarithmic column density of $\log N(\text{H I}) = 19.04$.

7.2.2 QSO B2230+02

Fig. 7.3 shows Na I and Ca II absorption lines towards QSO B2230+02, and the corresponding H I 21-cm emission from EBHIS. Note that the S/N of the spectrum in the range where Ca II could be found is relatively low. It is furthermore difficult to obtain a proper estimate for the S/N in this part of the spectrum, due to the possible absorption lines that might be located in this range. Thus, the assessment of the significance of the Ca II absorption lines in this regime is difficult. However, based on the local average S/N, a relatively high 5σ upper limit of $\log N(\mathrm{Ca\,II}) < 11.7$ is estimated.

In this line of sight, all possible detections of Na I and Ca II are weak and there is no indication for corresponding H I emission detected with the beam resolution and the sensitivity of the Effelsberg telescope.

7.2.3 QSO B1759+7539

Fig. 7.4 shows the spectrum of QSO B1759+7539 for the absorption by interstellar Na I and Ca II, together with the corresponding H I 21-cm emission retrieved from the LAB survey.

The heavy blending and saturation makes it extremely difficult to interpret Ca II lines. Na I absorptions however are mainly detected in gas with low LSR velocities, showing a multi-component structure of two stronger absorption components due to the disc gas, and a weaker IVC at $v_{\mathrm{LSR}} \simeq -38$ and possibly one at $v_{\mathrm{LSR}} \simeq -50$. The velocity range of the IV gas shows in the LAB 21-cm data a broad ($\Delta v_{\mathrm{FWHM}} = 39$ km s^{-1}) component at $v_{\mathrm{LSR}} \simeq -48$ km s^{-1}, with $\log N(\mathrm{H\,I}) = 20.01$.

Other possible Na I detections at $v_{\mathrm{LSR}} \simeq -105$ and $v_{\mathrm{LSR}} \simeq +100$ km s^{-1} remain undetected in the LAB data.

7.2.4 QSO J0812+32

Fig. 7.5 shows the spectrum of QSO J0812+32 for the absorption by Galactic Na I and Ca II, together with the corresponding H I 21-cm emission retrieved from the LAB survey.

Na I at $v_{\mathrm{LSR}} \simeq +195$ km s^{-1} is only detected above the 4σ significance level in one of the doublets, and does not seem to have any H I counterpart in the LAB data. The only firm halo Na I detection in this line of sight is at $v_{\mathrm{LSR}} \simeq -19$ km s^{-1}, which is possibly associated with LLIV-Arch. There is a corresponding broad H I emission in the LAB data, which peaks at $v_{\mathrm{LSR}} \simeq -10$ km s^{-1}, as indicated by a multi-component Gaussian fit, taking into account the strong H I disc emission at $v_{\mathrm{LSR}} \simeq -1$ and $v_{\mathrm{LSR}} \simeq +11$ km s^{-1}. This possible IV component has a line width of $\Delta v_{\mathrm{FWHM}} = 30$ km s^{-1}, and a column density of $\log N(\mathrm{H\,I}) = 20.13$. This broad emission line might have further subcomponents which are not resolved in the LAB data.

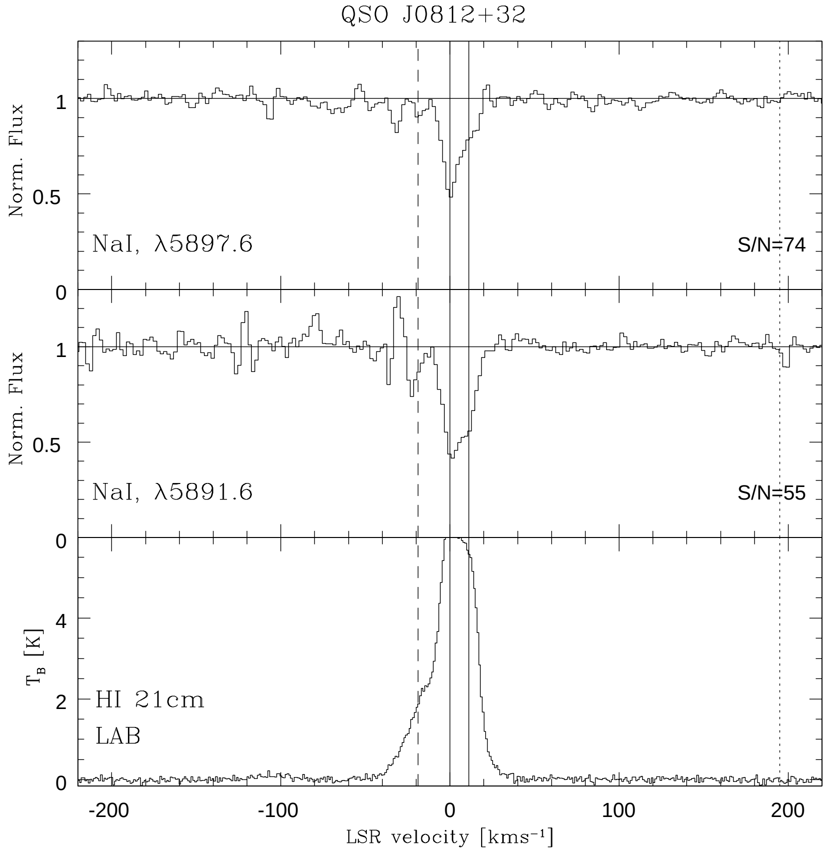

Figure 7.5: As Fig. 7.1, but towards QSO J0812+32, and the Ca II spectrum not recorded. The H I emission spectrum was retrieved from the LAB survey.

7.2.5 QSO B0836+1122

Fig. 7.6 shows the spectrum of QSO B0836+1122 for the absorption by interstellar Na I and Ca II, together with the corresponding H I 21-cm emission retrieved from the LAB survey. Three (possibly four) Na I absorbers were detected in this line of sight, without any H I counterparts in the LAB data. Among these the component at $v_{\mathrm{LSR}} \simeq -49$ km s^{-1} is possibly associated with the IV-Arch. Note the Na I at $v_{\mathrm{LSR}} \simeq -28$ km s^{-1} is an artifact and thus has not been analysed. This velocity component, however, has an H I counterpart at $v_{\mathrm{LSR}} \simeq -20$ km s^{-1} with a line width of $\Delta v_{\mathrm{FWHM}} = 16$ km s^{-1} and $\log N(\mathrm{H\,I}) = 19.79$.

7.2.6 QSO B0841+129

Fig. 7.7 shows the spectrum of QSO B0841+129 for the absorption by interstellar Na I and Ca II, together with the corresponding H I 21-cm emission retrieved from the LAB survey.

This line of sight shows some possible HV Na I absorption lines in the velocity range $v_{\mathrm{LSR}} \simeq +110$ to $+158$ km s^{-1}, and possibly one absorber at $v_{\mathrm{LSR}} \simeq -125$ km s^{-1}, none of

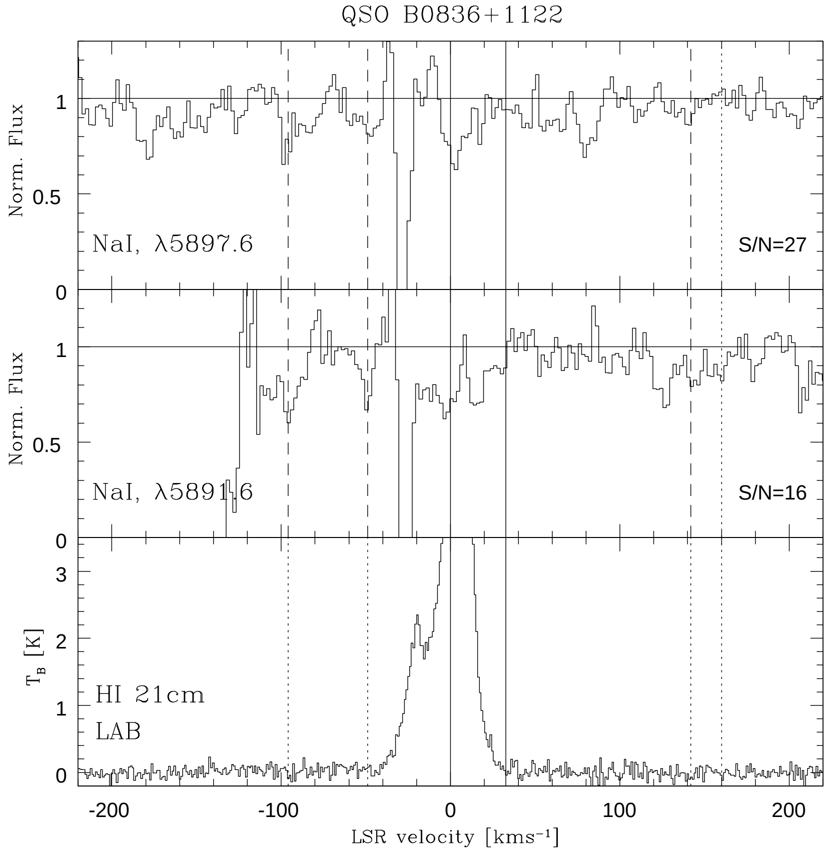

Figure 7.6: As Fig. 7.1, but towards QSO B0836+1122, and the Ca II not recorded. The H I emission spectrum was retrieved from the LAB survey.

which are detected in the LAB H I data. The stronger IV Na I absorber at $v_{\rm LSR} \simeq -28$ km s^{-1}, however, has a corresponding narrow H I emission, with $\Delta v_{\rm FWHM} = 9$ km s^{-1}, and $\log N$(H I)= 19.64. A multi-component Gaussian fit to the H I emission also implies the existence of a very weak HVC component at $v_{\rm LSR} \simeq -38$ km s^{-1}, with $\Delta v_{\rm FWHM} = 11$ km s^{-1}, and $\log N$(H I)= 18.69 which corresponds to the weak Na I absorber at $v_{\rm LSR} \simeq -40$ km s^{-1}. Based on the coordinates and the velocity, these latter two components appear to be associated with IV-Arch or LLIV-Arch.

7.3 On the overall gas structure

Previous systematic studies have shown that the halo of the Milky Way contains a number of weak Ca II and Na I absorbers, detected in high-resolution optical data with high S/N, which in some cases do not have a 21-cm emission counterpart in the H I surveys (Richter et al. 2005; Ben Bekhti et al. 2008). In this Chapter, we have presented further sightlines with detected halo Na I (and Ca II in some cases), some of which remain unseen or are not

Table 7.1: Logarithmic column densities[a] $\log N$ [N in cm^{-2}], and b-values[a] [km s^{-1}] of Na I and Ca II absorbers, and their possible associations to known IVC/HVC complexes.

QSO	RA	Dec	v_{LSR}	$\log N$(Na I)	b(Na I)	$\log N$(Ca II)	b(Ca II)	IVC/HVC
QSO B1157+014	11 59 44.8	+01 12 07.0	−41	10.60±0.14	0.7±0.3	11.39±0.02	1.6±0.2	IV Spur
(Fig. 7.1)			−25	11.24±0.13	0.7±0.1	11.90±0.03	8.9±0.7	IV Spur?
			−8	$< 11.6^{\mathrm{d}}$		11.92±0.02	5.8±0.3	
			+8	-	-	11.61±0.04	0.5±0.0	
			+28	< 11.1		11.31±0.02	0.9±0.0	IV-WA?
			+35	-	-	11.23±0.04	1.4±0.2	IV-WA
			+44	-	-	11.36±0.03	3.4±0.6	IV-WA?
QSO B2230+02	22 32 35.2	+02 47 55.8	−195	< 11.1		-	-	EN?
(Fig. 7.3)			−123	10.89±0.03	2.6±0.7	-	-	
			−108	< 11.2		-	-	
			−80	11.08±0.37	0.4±0.2	-	-	PP-Arch
			+75	-	-	12.67±0.05	0.5±0.0	
QSO B1759+7539	17 57 46.4	+75 39 16.2	−105	< 10.9		x$^{\mathrm{b}}$	x$^{\mathrm{b}}$	
(Fig. 7.4)			−50	< 11.0		x$^{\mathrm{b}}$	x$^{\mathrm{b}}$	LLIV-Arch
			−38	11.86±0.01	3.8±0.1	x$^{\mathrm{b}}$	x$^{\mathrm{b}}$	LLIV-Arch?
			+100	< 11.1		x$^{\mathrm{b}}$	x$^{\mathrm{b}}$	
QSO J0812+32	08 12 40.7	+32 08 08.6	−19	11.00±0.03	0.4±0.1	x	x	LLIV-Arch?
(Fig. 7.5)			+195	< 10.7		x	x	
QSO B0836+1122[c]	08 39 33.0	+11 12 03.8	−96	11.81±0.01	7.0±0.2	x	x	
(Fig. 7.6)			−49	11.52±0.01	2.0±0.3	x	x	IV-Arch
			+142	11.37±0.03	4.9±0.8	x	x	
			+160	< 11.4		x	x	
QSO B0841+129[c]	08 44 24.2	+12 45 48.9	−125	< 11.4		x	x	
(Fig. 7.7)			−40	11.13±0.02	3.5±0.5	x	x	IV-Arch
			−28	11.86±0.01	2.9±0.1	x	x	IV/LLIV-Arch
			+110	< 11.4		x	x	
			+128	11.15 ± 0.02	3.6 ± 0.6	x	x	
			+158	< 11.2		x	x	

[a] The errors given are due to the quality of the fit, and do not include the uncertainties in the noise statistics and continuum placement. See Sect. 4.2.3 for a thorough discussion.

[b] heavily blended.

[c] The spectrum was locally re-normalised.

[d] The upper limit was based on the weaker line of the doublet.

x Out of the recorded spectral range, or interpretation not possible due to defect spectrum, or heavy blending.

\- Not detected.

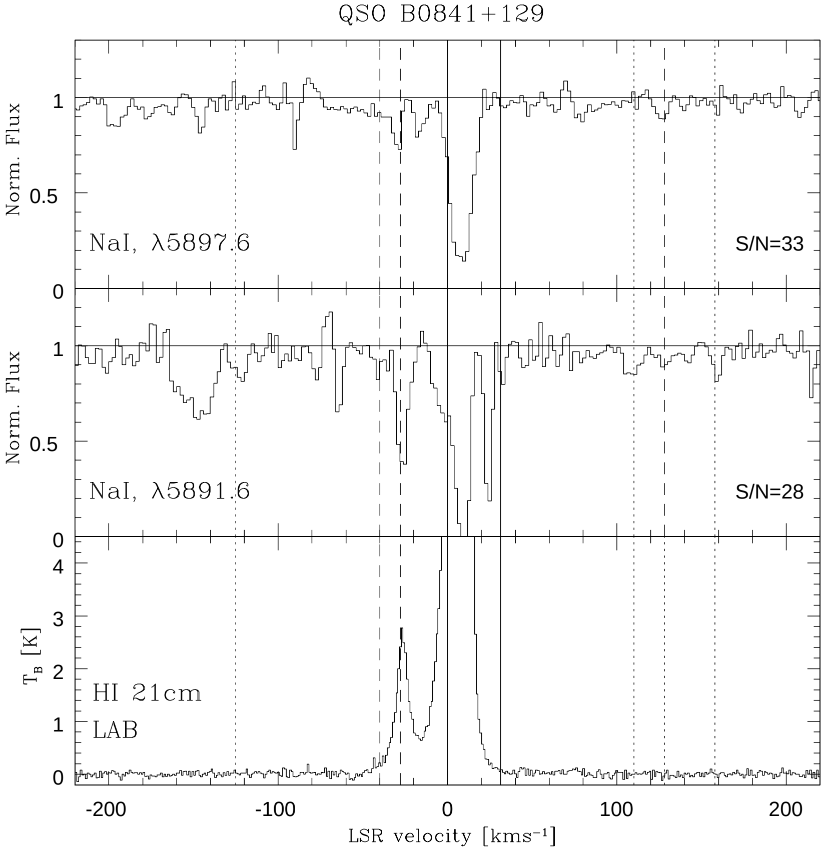

Figure 7.7: As Fig. 7.1, but towards QSO B0841+129, and the Ca II not recorded. The H I emission spectrum was retrieved from the LAB survey.

resolved in single-dish H I 21-cm observations. The fact that also here, in our limited number of sightlines, we detect Na I (Ca II) at low and/or high LSR velocities, and mostly with low column densities, verifies the previous statements on the ubiquity of these low-column density absorbers in the halo of the Milky Way. Our detection includes 18 halo IVC and HVC components (with additional 10 possible components), most of which are weak.

Unfortunately, the angular separations between the background QSOs are not small enough for studies of small scale spatial variations between the sightlines. Such studies are in general less practical towards QSO background sources due to the fact that one seldom finds several of these objects spread over a small area of the sky. The smallest angular separation in our sample is between the lines of sight towards QSO B0841+129 and QSO B0836+1122 of ∼ 1.5 deg, clearly sampling gas of different properties. Nevertheless, a detailed comparison of the absorptions from Na I, to the corresponding components in Ca II and H I along each line of sight, allows us to draw conclusions about the neutral gas structures for the individual components, which we discuss below.

Comparison between the results from absorption-line data to the results from single-dish radio telescopes is particularly interesting for studying the different gas phases. While the absorption-line spectroscopy of Na I (and Ca II) gives sensitive pencil beam information of the neutral cool gas, the single-dish radio telescopes with a large beam area sample the more extended H I gas, and average out possible small structures. The fact that we, in some cases, observe weak Na I and/or Ca II absorbers without H I counterparts suggests that the H I column density of these structures are below the detection limit, and/or these are small-scale structures in the gas well below the angular size of the radio telescope's beam, that get smeared out and *then* fall below the detection limit of the H I 21-cm data. We take as an example of a Na I absorber without an H I counterpart, the component at $v_{\rm LSR} = -49$ km s^{-1} towards QSO B0836+1122. Wakker & Mathis (2000) found a correlation between the gas-phase abundances and the column densities, describing a relation between the observed Na I and H I column densities. We use that relation to obtain the expected H I column density associated with this $v_{\rm LSR} = -49$ km s^{-1} component (note that this is only a rough estimate): $\log N({\rm H\,I}) = (\log N({\rm Na\,I}) + 5)/0.84 = 19.7$. Even when assuming a line width as broad as 40 km s^{-1}, such features should have a significance about 6σ in the LAB 21-cm data. The fact that no H I is detected here indicates sufficient substructure in the gas, well below $35'$ (the angular resolution), that has been averaged out .

Furthermore, some of the detected Na I (and Ca II) absorbers show multiple components with a velocity difference of about 7 to 12 km s^{-1}. Most of these are not obvious in the H I 21-cm EBHIS, or LAB data.[2] These multiple absorptions indicate substructures on small scales that can not be detected by the large H I surveys due to the beam smearing effects. Thus, the angular diameter of such clumps must be way below the beam size of the radio telescope, i.e., below $9'$ in the case of Effelsberg observations. Interferometric data with higher spatial resolution (typically about few arcseconds) might be able to separate these components, provided that these structures are not below the resolving power of the interferometers. Richter et al. (2005); Ben Bekhti et al. (2009), for example, present QSO sightlines for which, some (but not all) of the indicated substructures in Ca II (and Na I), previously absent or not resolved in LAB survey or Effelsberg observations, have been resolved in follow-up interferometric observations.

Comparing the b-values of the Na I and Ca II lines is useful for analysing the contributions of the thermal and turbulent broadening for each component, and for comparing the different gas components (recalling Eq. (2.12) and (2.13) in Sect. 2.2.4), and thereby, to better understand the distribution of the different gas phases. If both species would be evenly distributed in space, one would expect $b({\rm Na\,I})/b({\rm Ca\,II})=A({\rm Ca\,II})/A({\rm Na\,I})=1.32$ (A is the atomic weight, see Eq. (2.13)) for purely thermal Doppler broadening, and $b({\rm Na\,I})/b({\rm Ca\,II})=1$ for turbulent dominated broadening. Most of our analysed Na I lines appeared to have very low b-values ($b < 1\,{\rm km\,s^{-1}}$) according to the fitting programme. This was usually not the case for the Ca II lines. However, our data is too poor for a direct

---

[2] Note that the H I 21-cm surveys have much higher velocity resolution than the spectrographs used here. The reason for such multi-components not being resolved in EBHIS, or LAB data is due to their small sizes rather than their separation in velocity.

comparison, as we have only two cases where both Na I and Ca II are detected in the same gas component. Furthermore, as discussed in Sect. 4.2.3, the errors in the b-values are much larger than the ones provided in Table 7.1. Given the indicated b-values to be accurate, $b(\mathrm{Na\,I}) \ll b(\mathrm{Ca\,II})$ would imply that the Na I is located in more confined or cooler and denser regions than the Ca II counterpart in the IV gas in the direction of QSO B1157+014.

Despite the large uncertainties in the b-values (Sect. 4.2.3), the fact that such low values are needed to explain the line strength for most of the detected absorbers suggest that the actual b-values generally are below the instrumental resolution, $b < 7\,\mathrm{km\,s^{-1}}$. If ones assumes $b = 7$ $\mathrm{km\,s^{-1}}$ an upper temperature of $T < 6.8 \times 10^4$ K can be constrained from the Na I absorption (Eq. (2.13), assuming purely thermal broadening). This is much higher than the typical temperature for the cold neutral gas where the Na I (with an ionisation potential of 5.1 eV) is expected to be located. This upper temperature is higher than the upper temperature limit of $T_{\mathrm{max}} \approx 1.4 \times 10^3$ to 3.3×10^4 K (Eq. (2.25)) indicated by the corresponding H I emission lines with line widths in the range of $\Delta v_{\mathrm{FWHM}} = 8$ to 39 $\mathrm{km\,s^{-1}}$. As the H I 21-cm data samples the more extended region, where the gas may also be partially ionised, this upper limit is a valid limit also for the colder neutral gas which give rise to the Na I absorption lines. Based on $T_{\mathrm{max}} \approx 1.4 \times 10^3$ to 3.3×10^4 K, equivalent upper limit for the Doppler parameters of the Na I counterparts would be $b(\mathrm{Na\,I}) \approx 1$ to 5 $\mathrm{km\,s^{-1}}$, clearly lower than the spectral resolution, and in line with the low b-values from our analysis. Given such low b-values of $\lesssim 1$ to 5 $\mathrm{km\,s^{-1}}$, also the turbulent motions in the gas are relatively small.

By comparing the results from sensitive absorption-line data with the single-dish H I 21-cm data we find indications to the presence of small substructure, which likely give rise to the observed IV and HV Na I (and Ca II) absorptions, but get smeared out in the H I data. The Na I and Ca II absorptions are sensitive tracers of the neutral gas at low column densities, which can remain undetected in the large H I surveys due to beam smearing effects, as has also been shown by previous studies (Richter et al. 2005; Ben Bekhti et al. 2008, 2009). Deriving the physical properties and the sizes of these halo absorbers based on the available observations is beyond the scope of this work. Furthermore, some of these absorbers are near the detection limit, and require higher quality data for a more accurate analysis. Optical spectra with higher spectral resolution, and interferometric observations would help us to better understand the gas-phase distribution traced by these species and to obtain the physical properties of these absorbers.

7.4 Comparison with other Na I and H_2 absorbers and constraints on the small-scale structure

Molecular hydrogen and Na I both require dense confined regions where they are shielded from strong UV radiation field, or else they would be dissociated (H_2) or ionised (Na I). As pointed out earlier, and shown in Chapters 5 and 6, the detection of H_2 and other ele-

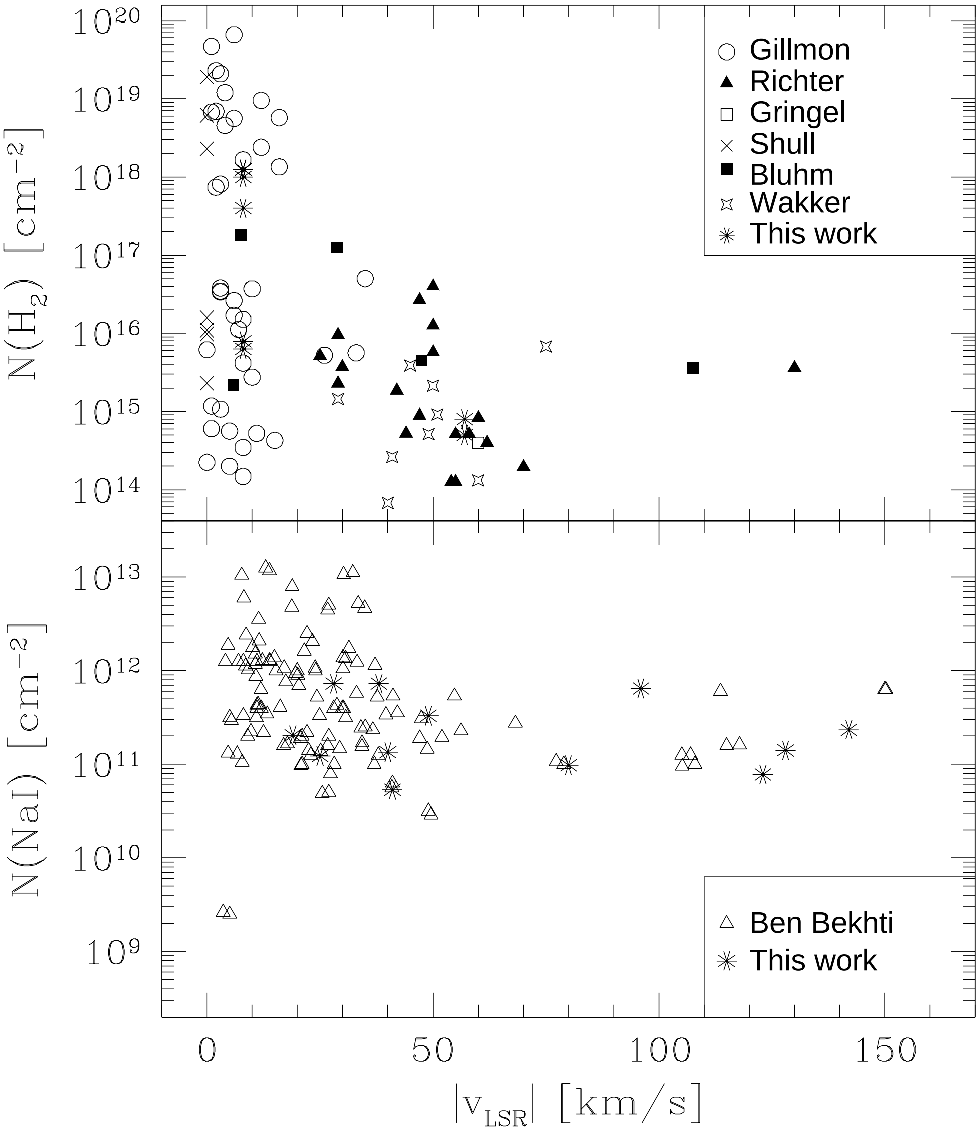

Figure 7.8: The column-density distribution of H_2 (upper plot) and Na I (lower plot) absorbers as a function of their LSR velocities, $|v_{\rm LSR}|$. The result is taken from this work (Chapter 5, 6, 7) as well as other lines of sight (Gringel et al. (2000); Shull et al. (2000); Bluhm et al. (2001); Richter et al. (2001, 2003a,b); Gillmon et al. (2006); Wakker (2006); Ben Bekhti et al. (2008); Ben Bekhti et al. (in preparation)). Note that the Na I detections presented in this plot were selected for the halo studies and thus lack the higher column density disc gas at $v_{\rm LSR} \approx 0$. As it is clear from both plots, the high-column density absorbers are mainly found at low $|v_{\rm LSR}|$, and the number and column densities decreases towards higher $|v_{\rm LSR}|$, with some exceptions (note the three H_2 absorbers at $|v_{\rm LSR}| > 70$ km s^{-1} with $\log N(H_2) > 15$).

ments in the FUV range has the advantage of providing us with the informations necessary to interpret the physical properties of the gas. Such a study is, however, limited to the number of bright UV background sources. Furthermore, because of the typically low S/N of the FUV data in combination with the medium resolution of the FUV spectrographs, we may be missing populations of low-column density halo H_2 structures that fall below the detection limits of the available data. As it was discussed in Chapter 6, the IV H_2 was detected in the two lines of sight, with data of high S/N, bearing column densities of $\log N(H_2) \leq 14.9$, slightly below the detection limit of the other studied lines of sight in that Chapter which had poorer data quality. On the other hand, absorption-line studies of the many QSO background sources, observed typically with high-resolution echelle spectrographs, have revealed a number of Na I absorbers in the halo of the Milky Way (Richter et al. 2005, 2009; Ben Bekhti et al. 2008). Given the very low ionisation potential of Na I, these absorbers are likely residing in similar regions as the H_2. Thus, in this Section we look at the distribution of the detected H_2 in parallel with the detected Na I absorbers throughout the Milky Way, to better understand the cold discrete regions connected with these absorbers.

We plot in Fig. 7.8 the column densities of H_2 and Na I absorbers against their LSR velocities. We have included in that figure the results of other authors who have surveyed different Galactic directions for H_2 (Gringel et al. 2000; Shull et al. 2000; Bluhm et al. 2001; Richter et al. 2001, 2003a,b; Gillmon et al. 2006; Wakker 2006) and for Na I absorption (Ben Bekhti et al. 2008, Ben Bekhti et al., in preparation). Note that there are more detected H_2 and Na I absorptions than the ones included here, but those mainly overlap with other low-velocity absorbers. In particular, the presented Na I results lack the higher column density disc absorbers. This is because the results included here were taken from studies aiming at studying halo properties; they thus excluded the disc Na I components.

It should be pointed out that the column-density distribution as a function of v_{LSR} does not give the direct proportionality to the distances to these absorbers. Accurate distances to most IVCs and HVCs are difficult to obtain, thus no direct proportionality is assessed between LSR velocities and distances. Furthermore, halo clouds may exist that are confused with the local disc gas due to their low radial velocities (LVHCs, Sect. 1.2.4). However, the approximate distances are known to many IVCs and HVCs (see Sect. 1.2.2 and 1.2.3). It is understood that IVCs are in general located closer to the Galactic disc, while HVCs are located at higher scale heights. Thus, even though the v_{LSR} is not directly proportional to the distance, the Fig. 7.8 demonstrates the overall distribution of these absorbers in the Galactic disc (with low $|v_{\mathrm{LSR}}|$), inner halo (with low to intermediate $|v_{\mathrm{LSR}}|$) and outer halo (with high $|v_{\mathrm{LSR}}|$).

As it can be seen in the figure, the “high” column density absorbers (here meaning $\log N(H_2) \geq 18$) are only found at low LSR velocities; they are probably related to the Galactic disc or the disc-halo interface. There is a clear decline in column densities as we move away from the low-velocity components to higher LSR velocities. This decline is more obvious for $0 \leq |v_{\mathrm{LSR}}| \leq 70$ km s^{-1}, and almost linear when neglecting the low velocity absorbers[3], with $|v_{\rm LSR}| < 20$ km s^{-1} and $\log N(\mathrm{H_2}) < 17$. Following this line, the three halo components with $|v_{\rm LSR}| > 70$ km s^{-1} appear to have column densities higher than what would be expected from this trend.

Also Na I absorbers show a decline in column densities with the increase of $|v_{\rm LSR}|$, although this decline seems more spread out than the H_2 distribution. Note, however, that the disc Na I absorbers were excluded here, thus the large number of detections of Na I at low velocities are mainly due to gas with velocities not following the Milky Way rotation. As it is clear from the figure, Na I absorbers are most common at low LSR velocities, the number of which drops significantly for $|v_{\rm LSR}| > 50$ km s^{-1}.

As it is demonstrated in Fig. 7.8, the number of detected H_2 and Na I, and thus the cold dense structures bearing them, decreases with $|v_{\rm LSR}|$, as well as the column densities of these absorbers. Judging from the results, it is more likely to observe patchy structures and discrete clouds that are possibly connected with the H_2 and Na I absorbing regions in low and intermediate velocity clouds. Some of these absorbers at low velocities could possibly be cold clouds in transition regions between the Galactic disc and halo. As previously demonstrated by observations (Lockman 2002; Stanimirović et al. 2006; Begum et al. 2010), and expected by models, the disc-halo interface region includes a number of discrete H I clouds, on scales of a few parsecs. Follow-up interferometric observations in the directions where low-velocity H_2 and Na I absorbers are found are necessary to resolve the possibly existing H I clumps in these regions.

The fact that the H_2 and Na I absorbers are more common at low and intermediate LSR velocities, and often with higher column densities, may not be surprising. The turbulences and dynamical compression in the disc and disc-halo interface probably result in higher density regions which allow for a more efficient H_2 formation and preservation. Regions of similar densities may also preserve the Na I and keep it from becoming ionised. Thus, it is more likely to observe patchy structure and discrete clouds connected with the H_2 and Na I absorbing regions closer to the disc of the Milky Way. The decline in the H_2 distribution may partly be intrigued by the decrease of dust-to-gas ratio with the scale height. The decrease of dust abundance is often observed as smaller ratio for Na I/Ca II at higher scale heights (Routly-Spitzer effect, Routly & Spitzer 1952).

Whether all the presented absorbers in Fig. 7.8 represent small high-density clumps out of pressure equilibrium with the surrounding medium, or semi-stable clouds, can not be judged without knowing details on their physical properties. Given the many low-column density H_2 absorbers at $|v_{\rm LSR}| > 20$ km s^{-1}, which indicate low line self-shielding, it is likely that the observed H_2 also in those lines of sight is preserved in small-sized confined structures, where it is protected from the ambient UV-radiation. Thus, many of these absorbers could be associated with transient clumps or fragmented shells driven by a highly turbulent medium.

There are however, H_2 absorbers, and small-scale structures associated with them,

---

[3] The low-velocity H_2 absorbers with $\log N(\mathrm{H_2}) \leq 15$ are from regions in the northern Galactic hemisphere and some of these may be related to the "Northern Chimney" and "Lockman Hole" (see Gillmon et al. 2006).

detected at higher velocities ($|v_{\rm LSR}| > 70\ {\rm km\,s^{-1}}$) (see also, Richter et al. 1999; Bluhm et al. 2001; Wakker 2006), the existence of which is more puzzling. While the H_2 detections in these HVCs are believed to have a Galactic origin, the larger number of Na I absorbers in the HVCs in the outer halo as well as other H_2 HV absorptions (e.g., H_2 detected in the Leading Arm of the Magellanic Stream, Sembach et al. 2001) may originate from infalling cool gas through tidal interactions, winds and outflows from other galaxies and from intergalactic medium. The detailed analysis on the scale heights and distances to these absorbers, as well as numerical simulations re-producing these structures given local as well as Galactic dynamical processes, will be important for a better understanding of the origin and nature of these absorbers.

Chapter 8

Summary, conclusions and outlook

This Chapter provides the summary and conclusions from the Chapters 5, 6, and 7 and addresses some of the remaining issues as well as possible future approaches that can be taken towards a better understanding on the subject.

8.1 Summary & conclusions

8.1.1 Chapter 5

In Chapter 5, we have studied the small-scale structure in the Galactic disc gas towards the LMC. We presented FUV and UV absorption-line measurements of Galactic H_2, C I, C I*, C I**, N I, O I, Al II, Si II, P II, S III, Ar I, and Fe II towards the six LMC stars Sk-67°111, LH 54-425, Sk-67°107, Sk-67°106, Sk-67°104, and Sk-67°101, and analysed the properties of the Galactic disc gas in these lines of sight. Our sightlines were chosen within $5'$ in RA, with an almost constant Dec, to allow us to investigate the small-scale structures of the interstellar gas within the spatial scales of ≤ 1.5 pc (given the angular extent between Sk-67°111 and Sk-67°101, and assuming that the observed gas exists at a maximum distance of 1 kpc). The smallest separation is between LH 54-425 and Sk-67°107 lines of sight of about $17''$ (corresponding to a projected scale of ≤ 0.08 pc). For four of the sightlines, Sk-67°101, Sk-67°104, Sk-67°106, and Sk-67°107, we also analysed STIS spectral data, from which we have further determined the column densities of Mg II, Si IV, S II, Mn II, and Ni II. The STIS data provide additional absorption lines for some of the species already available in the FUSE spectra, allowing us to have a more reliable determination of the column densities.

In the spectral range of FUSE we are able to gain information from the different rotational excitation levels of H_2, which provides us with valuable information about the physical properties of the gas. The H_2 absorption lines show considerable variation between our sightlines. The lines of sight towards Sk-67°101 and Sk-67°104 contain a significantly higher amount of H_2 (about 2 orders of magnitude higher column density) compared to Sk-67°111. This spatial variation is, however, not uniform and density fluctuation on scales smaller than the extent of $5'$ cannot be excluded.

The derived rotational excitation temperature of $T_{\rm exc} \sim 70\,{\rm K}$ towards Sk -67°101 to Sk -67°107, together with the low b-values emerging from absorption by the lower J-levels, indicate that the molecular hydrogen probably arises in confined dense regions in these lines of sight, where it is self-shielded from UV-radiation, and not exposed to any strong interstellar turbulences. The gas in the direction of LH 54-425 and Sk -67°111, on the other hand, appears to be fully thermalised, with $T_{\rm exc} \sim 200\,{\rm K}$ over all J-levels detected, representing an upper limit for actual kinetic temperature.

In order to trace these variations back to the actual density variations and changes in the physical properties of the gas, we used two different approaches. First, instead of deriving the actual values for the volume densities $n_{\rm H}$, we derived density ratios, ξ, between each two adjacent lines of sight, based on the H_2 and O I column densities, and assuming a formation-dissociation equilibrium of molecular hydrogen. This approach suggests variations in densities along these lines of sight. Second, we derived $n_{\rm H}$ based on the excitation of the fine-structure levels of neutral carbon. For this, we also used the derived $T_{\rm exc}(H_2)$, assuming that C I and H_2 exist in the same physical region. This latter approach result in densities $n_{\rm H} \simeq 40 - 80\,{\rm cm}^{-3}$ towards Sk -67°101 to Sk -67°107, the lines of sight for which we have relatively accurate measurements for column densities of C I and C I* as well as $T_{\rm exc}$. Based on these densities and $N({\rm H\,I})_{\rm tot}$, as obtained from the total observed $N({\rm O\,I})$ along each line of sight, we derived the pathlength of the partly molecular cloud to be $D_{\rm mol} = 0.5$ to 1.8 pc. In the direction of LH 54-425 and Sk -67°111, where we only had upper limits for the densities, we made use of the derived density ratios using the former method and an average density of $n_{\rm H} = 60\,{\rm cm}^{-3}$ as reference value, and estimated $D_{\rm mol}$ in the direction of LH 54-425 and Sk -67°111 to be 0.1 and 0.6 pc, respectively. The $n_{\rm H}$ derived in this way may be underestimated, and $D_{\rm mol}$ consequently overestimated, because $n_{\rm H}$, as derived from C I, is the averaged density of the molecular part of the gas where C I exists. Furthermore, the partly molecular cloud is more dense and confined than the extended neutral and partly ionised gas, thus only an unknown fraction of the observed $N({\rm H\,I})$ coexists with the observed H_2.

The derived pathlengths of the partly molecular gas observed here in the six LMC lines of sight are all of a similar linear scale as (or smaller than) the lateral extent of the sightlines of $\leq 1.5\,{\rm pc}$ (note that the absorbing gas can be located at a distance closer than the 1 kpc assumed thus far, resulting in a smaller spatial scale). Thus, the H_2 structures observed in these six lines of sight are not necessarily connected, but indicate sub-pc structures. While the clumpy nature of H_2 is verified by different studies (e.g., Pan et al. 2001; Lauroesch et al. 2000; Richter et al. 2003a,b; Marggraf et al. 2004), the Galactic H I gas, when sampled over a line of sight, normally does not show variations on small scales, since the unresolved substructures statistically cancel out and appear smooth over the total observed disc H I (or O I in our case) gas. Our derived density ratios, ξ, however, as well as the relative abundances, suggest that the number of such possible discrete absorbing cloudlets or patches should differ along the different sightlines, being less towards LH 54-425 and Sk -67°111. This interpretation also agrees with the higher electron density derived for these lines of sight.

8.1.2 Chapter 6

In this Chapter we reported on the detection of molecular hydrogen in the IV gas towards the LMC stars Sk -67°111 and LH 54-425, and emphasised the implications for the small-scale structure in the lower halo H_2 gas. The column densities of the detected H_2 are very low ($\log N(H_2) = 14.7$ towards Sk -67°111 and $\log N(H_2) = 14.9$ towards LH 54-425). Our other sightlines (Sk -67°107, Sk -67°106, Sk -67°104, Sk -67°101, all within $5'$ in RA) have a poorer data quality and therefore only allow us to estimate upper limits for the molecular hydrogen column densities, which are close to the $N(H_2)$ derived for the Sk -67°111 and LH 54-425 directions. We have further investigated the HV gas in these six lines of sight, in which we found no H_2 above the detection limit of $\log N(H_2) < 13.7$ towards Sk -67°111 and LH 54-425, and $\log N(H_2) < 14.2$ on average for the rest of the sightlines.

Assuming that H_2 forms in the IVC on the surface of dust grains, we derive densities of $n_{\mathrm{H}} = 530$ cm^{-3} towards Sk -67°111, and $n_{\mathrm{H}} = 670$ cm^{-3} towards LH 54-425, and small pathlengths of $D_{\mathrm{mol}} \simeq 100$ AU. Our findings suggest that the H_2 is situated in small dense structures embedded in diffuse halo gas, with properties similar to what has been found in the IV gas towards the LMC star Sk -68 80 (~ 1.3 degrees away from our sightlines, by Richter et al. 2003a). Among the H_2 detections in IVCs (Gringel et al. 2000; Richter et al. 2003a,b), these particular H_2 absorbing clumps (this work, and Richter et al. 2003a) stand out, as these structures are embedded in diffuse gas with H I column density ($N(\text{H I}) \approx 10^{18}$ cm^{-2}) about 1 to 2 orders of magnitude lower than what is typically found in H_2 absorbing regions in IVCs (see Richter et al. 2003b). Our derived excitation temperatures, $T \simeq 300$ K, represent only upper limits for the actual kinetic temperature of the gas where H_2 is located, resulting in high upper limits for the thermal pressure, $p/k = n \cdot T$, in the gas. Yet, even by adopting $T = 50$ K, similar to what was derived for the SK -68 80 sightline by Richter et al. (2003a), the thermal pressures are derived to be $p/k = 2.7 \times 10^4$ (towards Sk -67°111) and 3.4×10^4 K cm^{-3} (towards LH 54-425), thus a factor of ~ 5 higher than the expected pressure in the disc ($p/k \simeq 3000$ to 10^4 K cm^{-3}, Wolfire et al. 1995), and a factor of ~ 7 higher if the IVC is located at a z-height of 2 to 5 kpc and in pressure equilibrium (Schwarz & de Boer 2004). It is debatable, how such small dense overpressured structures are able to form and survive over longer timescales.

As strong turbulence produced by supernova-driven outflows from the disc in the Galactic fountain model favours the formation of short-lived small, dense structures in the gas, these high-density gas clumps in the disc-halo interface may represent transient structures rather than stable clouds. Given the formation timescale of the hydrogen molecule, $t_{\mathrm{form}} \geq 10^6$ yr, however, the H_2 in the IV gas may have formed in an originally larger IVC. Thus, these observed H_2 clumps towards the LMC, may represent high-density fragments left over from a recent breakup of a larger IVC, possibly caused by ram-pressure stripping and other instabilities. Furthermore, the H I 21-cm map of the IV gas in front of the LMC shows a number of scattered H I clouds that are likely physically connected with the intermediate-velocity absorption presented here. All these small clumps may have been part of a more coherent gas structure in earlier times. A better understanding of the physical and dynamical processes that may be responsible for these phenomena is essential to comprehend the origin of such overpressured small-scale structures.

8.1.3 Chapter 7

As it is evident from the previous Chapters, the detection of H_2 and other species in the FUV range has the advantage of providing us with information necessary to interpret the physical properties of the gas. Such study is, however, limited to the number of bright UV background sources and also to the quality of the data, in the lack of which we might be missing a population of cold gas clumps bearing H_2 with low column densities. In addition, absorption-line studies of many QSO background sources in the optical have revealed a large number of Na I absorbers in the halo of the Milky Way. Molecular hydrogen and Na I both require dense confined regions where they are shielded from strong UV radiation field, or else they would be dissociated (H_2) or ionised (Na I). Thus, in this Chapter we studied absorption by Na I (and Ca II when possible) in the spectra of QSOs, and at the end of the Chapter, we analysed the distribution of Na I absorbers in parallel with the detected H_2 throughout the Milky Way, to better understand the small-scale structures that are likely connected with these absorbers.

From the original sample of 42 QSOs observed with Keck HIRES with high spectral resolution, only 6 were suitable for the search of Na I doublets (and essentially only 2 for Ca II), in all of which we found Na I (Ca II) absorbers at halo velocities (halo velocities were defined using a kinematic model by Kalberla 2003; Kalberla et al. 2007). Our detection includes 18 halo IVC and HVC components (with additional 10 possible components), most of which are weak. The fact that also here, in our limited number of sightlines, we detect Na I (Ca II) at low and/or high LSR velocities, and mostly with low column densities, verifies the previous statements (Richter et al. 2005; Ben Bekhti et al. 2008) on the ubiquity of these low-column density absorbers in the halo of the Milky Way. In each line of sight, we searched for H I 21-cm emission associated with the detected Na I and/or Ca II absorbers. We used data from the EBHIS in first hand, and the LAB survey in second hand, when EBHIS data were not yet available. While the absorption-line spectroscopy of Na I (and Ca II) provides sensitive pencil beam information of the neutral cool gas, the single-dish radio telescopes with large beam area sample the more extended H I gas and average out the possible small structures. Therefore, not all Na I (and Ca II) absorbers have associated H I counterparts in the EBHIS or the LAB data. The multiple components detected in Na I, which are not separable in the H I 21-cm EBHIS or LAB data, again indicate substructures on small scales that can not be detected by the large H I surveys due to the beam smearing effects. Thus, the angular diameter of such clumps must be way below the beam size of the radio telescope, i.e., below $9'$ in the case of Effelsberg observations, and below $35'$ for the LAB data.

Our results further suggest that the b-values of many of the Na I absorbers are smaller than the instrumental resolution, i.e., $b \ll 7\ \mathrm{km\,s^{-1}}$. This also agrees with the derived upper limits of $b \leq 1$ to $5\ \mathrm{km\,s^{-1}}$, based on the line widths of the associated H I emission lines. Such low *b*-values, suggest that the turbulent motions in the gas are relatively small.

By comparing the results from sensitive high-resolution absorption-line data with the H I 21-cm data sampled over larger beams, we find indications for the presence of small substructures, which likely give rise to the observed IV and HV Na I (Ca II) features. Na I and Ca II are sensitive tracers of the neutral gas at low column densities, which remain undetected in the large H I surveys due to the beam smearing effects, as has also been shown by previous studies (Richter et al. 2005; Ben Bekhti et al. 2008, 2009).

At the end of this Chapter we looked at the column-density distribution of Na I as well as for H_2 measured in this work and by others (Gringel et al. 2000; Shull et al. 2000; Bluhm et al. 2001; Richter et al. 2001, 2003a,b; Gillmon et al. 2006; Wakker 2006; Ben Bekhti et al. 2008, Ben Bekhti et al., in preparation). The distribution of H_2 and Na I absorbers through the disc and the halo of the Milky Way suggests that these absorbers, and the cold discrete structures bearing them, are more pervasive in the disc and the disc-halo interface, the number and column density of which drops significantly towards the halo of the Galaxy. Thus, these structures probably are the product of a highly dynamic turbulent ISM, driven by Galactic fountains, chimneys, fragmented bubbles, stellar winds etc.

8.2 Concluding remarks and outlook

Using different approaches and different wavelength regimes of optical, UV, and FUV-absorption spectra, and H I 21-cm emission from single-dish radio telescopes we were able to find indications for confined structures at small scales embedded in the extended diffuse interstellar gas. Using the information of mainly H_2, O I, and C I absorption (Chapter 5), we found that the observed column-density variations in the Galactic disc gas trace true density enhancements, suggesting structures of different scales down to and likely below 0.1 pc. Based on the detection of H_2 in the diffuse IV gas (Chapter 6) we argued that the otherwise diffuse cloud must contain high-density high-pressure clumps on scales of ~ 100 AU, in which the H_2 is preserved. The fact, that H_2 has been detected in many IVCs, indicates that these clouds must contain relatively dense small structures allowing for the presence and maintenance of the H_2 (see Richter et al. 2003a,b).

The distribution of H_2 and Na I absorbers throughout the Galaxy further indicates the ubiquity of these absorbers and the cold discrete structures associated with them, the number of which is highest at low velocities, suggestively closer to the the Milky Way disc. This emphasises the role of turbulences and dynamical processes driven by Galactic fountains, which can produce high-density transient regions during the cooling and fragmentation phase. In the outer halo of the Milky Way, other dynamical instabilities in connection with tidal interactions with satellite galaxies and the intergalactic medium, and fragmentation of originally larger clouds may have caused high-density regions. This may also account for some of the discrete IVC structures. Detailed information on the scale heights and distances to the IVCs and HVCs that are associated with the detected

H_2 and Na I absorbers, as well as on the physical properties of the individual absorbers are necessary to relate their distribution to the actual distances for better testing these scenarios. Additional H_2 observations of the halo clouds are further needed to understand the high-velocity tail in the column-density distribution of these absorbers.

The analysis of the distribution and properties of these absorbers will further help us to grasp the overall and small-scale structure of the gas in the Galactic halo environment, and to determine the fractal dimensions. However, such a study would have to be limited by the instruments currently available. Considering the low column densities observed in Chapter 6 of $N(H_2) < 10^{15}$ cm^{-2}, data of high S/N is required for detection of H_2 absorption lines in IVCs and HVCs.

The theoretical challenge is to understand how the high-pressure small structures, at scales on the order of ~ 100 AU, can be produced and maintained over longer timescales, and what mechanisms are driving them. In addition, to better understand the physical conditions in such high-density halo clouds in the Milky Way, it would be of great importance to implement the grain formation and photodissociation of H_2 in numerical simulations of Galactic fountain flows and Galactic winds (e.g., de Avillez & Breitschwerdt 2007).

As further observational approach, very high resolution spectra (with a resolution of FWHM ≤ 1 km s^{-1}) at different wavelength regimes for the LMC sightlines in which IVC H_2 absorption have been detected (as well as for the Na I absorbers in the QSO spectra) would be very useful. Such high-resolution data would enable us to investigate in detail the individual gas components and to derive accurate b-values for the different neutral and ionised species with high and low ionisation potentials, in order to better apprehend the distribution of the different species and the gas phase structure (see e.g., Welty (1998); Welty et al. (1999) for a similar study with optical high-resolution observations). Comparing the low b-values indicated by the H_2 IV absorption (Chapter 6) with the measured line widths of low-ionisation species such as Ca II and Na I in very high resolution spectra will further help us to better constrain the contribution of the thermal and turbulence motions in the gas to the line broadening and the role they may play in preserving these small-scale structure against a pressure contrast in relation to the ambient diffuse medium.

Furthermore, follow-up interferometric 21-cm observations with high sensitivity and higher beam resolution are necessary for resolving the cloud structures on small spatial scale and to analyse the physical properties of the clumps related to the ones detected in absorption. However, given the small sizes of 100 AU, as derived in Chapter 6, it is unlikely that such clumps, detected in the FUV absorption-line spectroscopy, will be fully resolved by interferometric H I observations.

Thus, combining the measurements from different wavelength regimes is necessary for gaining a comprehensive understanding of the distribution of the different gas phases that contain or surround the small-scale structure in the ISM. The future as well as present instrument upgrades, such as the Cosmic Origins Spectrograph (COS) on HST, and interferometers such as VLA, the WSRT, the Australia Telescope Compact Array (ATCA), the Square Kilometre Array (SKA), and Australian Square Kilometre Array Pathfinder (ASKAP), will help in achieving a systematic understanding of the gas-phase distribution in the diffuse clouds containing small-scale structure, indicated by the H_2 or Na I low column density absorbers. Furthermore, numerical simulations which can produce the number density of these small-scale high density structures, are of great importance in understanding the physical conditions and the mechanisms responsible for this phenomenon.

Bibliography

Abgrall, H., Roueff, E., Launay, F., Roncin, J. Y., & Subtil, J. L. 1993a, A&AS, 101, 273 53, 63

Abgrall, H., Roueff, E., Launay, F., Roncin, J. Y., & Subtil, J. L. 1993b, A&AS, 101, 323 53, 63

Andrews, S. M., Meyer, D. M., & Lauroesch, J. T. 2001, ApJ, 552, L73 17

Arnal, E. M., Bajaja, E., Larrarte, J. J., Morras, R., & Pöppel, W. G. L. 2000, A&AS, 142, 35 51

Asplund, M., Grevesse, N., & Sauval, A. J. 2005, ASPC, 336, 25 73, 80, 81, 89, 90, 93

Bahcall, J. N. & Salpeter, E. E. 1965, ApJ, 142, 1677 24

Bahcall, J. N. & Wolf, R. A. 1968, ApJ, 152, 701 36

Bajaja, E., Arnal, E. M., Larrarte, J. J., et al. 2005, A&A, 440, 767 51

Ballesteros-Paredes, J., Klessen, R. S., Mac Low, M., & Vazquez-Semadeni, E. 2007, Protostars and Planets V, 63 19

Bates, B., Catney, M. G., & Keenan, F. P. 1990, MNRAS, 245, 238 17

Bates, B., Gilheany, S., & Wood, K. D. 1991, MNRAS, 252, 600 17

Bates, B., Shaw, C. R., Kemp, S. N., Keenan, F. P., & Davies, R. D. 1995, ApJ, 444, 672 17

Begum, A., Stanimirović, S., Peek, J. E., et al. 2010, ApJ, 722, 395 112

Ben Bekhti, N. 2009, PhD thesis, Rheinischen Friedrich-Wilhelms-Universität Bonn 24

Ben Bekhti, N., Richter, P., Westmeier, T., & Murphy, M. T. 2008, A&A, 487, 583 98, 105, 109, 110, 111, 118, 119

Ben Bekhti, N., Richter, P., Winkel, B., Kenn, F., & Westmeier, T. 2009, A&A, 503, 483 108, 109, 119

Bluhm, H., de Boer, K. S., Marggraf, O., & Richter, P. 2001, A&A, 367, 299 38, 85, 110, 111, 113, 119

Boissé, P., Rollinde, E., Hily-Blant, P., et al. 2009, A&A, 501, 221 18

Bomans, D. 1997, in HST Proposal, 7299 48

Bostroem, K. A., Aloisi, A., Bohlin, R., et al. 2010, STIS Instrument Handbook, version 10.0 edn., Baltimore: STScI 46

Bregman, J. N. 1980, ApJ, 236, 577 11

Bregman, J. N. 2004, in Astrophysics and Space Science Library, Vol. 312, High Velocity Clouds, ed. H. van Woerden, B. P. Wakker, U. J. Schwarz, & K. S. de Boer , 341 11

Brogan, C. L., Zauderer, B. A., Lazio, T. J., et al. 2005, AJ, 130, 698 16

Carruthers, G. R. 1970, ApJ, 161, L81 37

Charlton, J., Churchill, C., & Murdin, P. 2000, Quasistellar Objects: Intervening Absorption Lines, ed. Murdin, P. 31

Cho, J., Lazarian, A., & Vishniac, E. T. 2002, ApJ, 566, L49 19

Clifton, T. R., Frail, D. A., Kulkarni, S. R., & Weisberg, J. M. 1988, ApJ, 333, 332 16

Cohen, J. G. 1978, ApJ, 223, 487 17

Danforth, C. W., Howk, J. C., Fullerton, A. W., Blair, W. P., & Sembach, K. R. 2002, ApJS, 139, 81 47, 67

de Avillez, M. A. & Breitschwerdt, D. 2005, A&A, 436, 585 19

de Avillez, M. A. & Breitschwerdt, D. 2007, in EAS Publications Series, Vol. 23, EAS Publications Series, ed. M. A. Miville-Deschênes & F. Boulanger, 87 95, 120

de Boer, K. S. 2006, Physics and the interstellar medium. (University of Bonn) 33, 34, 35

de Boer, K. S., Koppenaal, K., & Pottasch, S. R. 1973, A&A, 28, 145 80

de Boer, K. S. & Morton, D. C. 1974, A&A, 37, 305 18, 35, 36, 80

de Boer, K. S., Richter, P., Bomans, D. J., Heithausen, A., & Koornneef, J. 1998, A&A, 338, L5 66

de Paolis, F., Ingrosso, G., Jetzer, P., Qadir, A., & Roncadelli, M. 1995, A&A, 299, 647 19

Deshpande, A. A. 2000, MNRAS, 317, 199 19

Deshpande, A. A., McCulloch, P. M., Radhakrishnan, V., & Anantharamaiah, K. R. 1992, MNRAS, 258, 19P 16

Dieter, N. H., Welch, W. J., & Romney, J. D. 1976, ApJ, 206, L113 16

Draine, B. T. 1998, ApJ, 509, L41 19

Draine, B. T. 2011, Physics of the Interstellar and Intergalactic Medium, ed. Draine, B. T. 30, 43

Draine, B. T. & Bertoldi, F. 1996, ApJ, 468, 269 78, 92

Elmegreen, B. G. 1997, ApJ, 480, 674 19

Elmegreen, B. G. 1999, ApJ, 527, 266 19

Faison, M. D. & Goss, W. M. 2001, AJ, 121, 2706 16

Faison, M. D., Goss, W. M., Diamond, P. J., & Taylor, G. B. 1998, AJ, 116, 2916F 16

Federman, S. R., Glassgold, A. E., & Kwan, J. 1979, ApJ, 227, 466 43

Field, G. B., Goldsmith, D. W., & Habing, H. J. 1969, ApJ, 155, L149+ 9

Field, G. B., Somerville, W. B., & Dressler, K. 1966, ARA&A, 4, 207 39, 40, 41

Fontana, A. & Ballester, P. 1995, The Messenger, 80, 37 56, 57

Frail, D. A., Weisberg, J. M., Cordes, J. M., & Mathers, C. 1994, ApJ, 436, 144 16

Gerhard, O. & Silk, J. 1996, ApJ, 472, 34 19

Gillmon, K., Shull, J. M., Tumlinson, J., & Danforth, C. 2006, ApJ, 636, 891 37, 110, 111, 112, 119

Gray, D. F. 1992, The observation and analysis of stellar photospheres., ed. Gray, D. F. 26

Gringel, W., Barnstedt, J., de Boer, K. S., et al. 2000, A&A, 358, L37 38, 85, 95, 110, 111, 117, 119

Hartmann, D. & Burton, W. B. 1997, Atlas of Galactic Neutral Hydrogen, ed. Hartmann, D. & Burton, W. B. 13, 51

Haverkorn, M. & Goss, W. M., eds. 2007, Astronomical Society of the Pacific Conference Series, Vol. 365, SINS - Small Ionized and Neutral Structures in the Diffuse Interstellar Medium 16

Heiles, C. 1997, ApJ, 481, 193 18, 85, 95

Heithausen, A. 2002, A&A, 393, L41 18

Heithausen, A. 2004, ApJ, 606, L13 18

Hjerting, F. 1938, ApJ, 88, 508 28

Jenkins, E. B. 2004, Ap&SS, 289, 215 19

Jenkins, E. B., Bowen, D. V., Tripp, T. M., et al. 2003, AJ, 125, 2824 37

Jenkins, E. B., Oegerle, W. R., Gry, C., et al. 2000, ApJ, 538, L81 73, 74

Jenkins, E. B. & Tripp, T. M. 2001, ApJS, 137, 297 18, 19

Johnston, S., Koribalski, B., Wilson, W., & Walker, M. 2003, MNRAS, 341, 941 16

Jura, M. 1974, ApJ, 191, 375 42

Jura, M. 1975, ApJ, 197, 575 42

Kaelble, A., de Boer, K. S., & Grewing, M. 1985, A&A, 143, 408 11, 15

Kalberla, P. M. W. 2003, ApJ, 588, 805 99, 100, 118

Kalberla, P. M. W., Burton, W. B., Hartmann, D., et al. 2005, A&A, 440, 775 11, 14, 15, 51, 98, 99

Kalberla, P. M. W., Dedes, L., Kerp, J., & Haud, U. 2007, A&A, 469, 511 14, 99, 100, 118

Kalberla, P. M. W. & Kerp, J. 2009, ARA&A, 47, 27 12

Kalberla, P. M. W., McClure-Griffiths, N. M., Pisano, D. J., et al. 2010, A&A, 521, A17 50, 74, 88

Kerp, J., Winkel, B., Ben Bekhti, N., Floeer, L., & Kalberla, P. 2011, ArXiv e-prints 50, 98

Kimble, R. A., Woodgate, B. E., Bowers, C. W., et al. 1998, ApJ, 492, L83 46

Lauroesch, J. T. & Meyer, D. M. 2003, ApJ, 591, L123 17

Lauroesch, J. T., Meyer, D. M., & Blades, J. C. 2000, ApJ, 543, L43 17, 18, 82, 116

Lehner, N., Staveley-Smith, L., & Howk, J. C. 2009, ApJ, 702, 940 94

Lindblad, P. O. 1967, Bull. Astron. Inst. Netherlands, 19, 34 12

Lockman, F. J. 2002, ApJ, 580, L47 12, 112

Lockman, F. J., Hobbs, L. M., & Shull, J. M. 1986, ApJ, 301, 380 12

Mac Low, M., Balsara, D. S., Kim, J., & de Avillez, M. A. 2005, ApJ, 626, 864 19

Marggraf, O. 2004, PhD thesis, Rheinischen Friedrich-Wilhelms-Universität Bonn 53, 56

Marggraf, O., Bluhm, H., & de Boer, K. S. 2004, A&A, 416, 251 18, 82, 116

McClure-Griffiths, N. M., Pisano, D. J., Calabretta, M. R., et al. 2009, ApJS, 181, 398 50, 74, 88

McKee, C. F. & Ostriker, J. P. 1977, ApJ, 218, 148 10

Meyer, D. M. 1990, ApJ, 364, L5 17

Meyer, D. M. & Lauroesch, J. T. 1999, ApJ, 520, L103 17

Minter, A. H., Balser, D. S., & Kartaltepe, J. S. 2005, ApJ, 631, 376 16

Moos, H. W., Cash, W. C., Cowie, L. L., et al. 2000, ApJ, 538, L1 46

Moos, H. W., Sembach, K. R., Vidal-Madjar, A., et al. 2002, ApJS, 140, 3 73

Morton, D. C. 2003, ApJS, 149, 205 53, 61

Morton, D. C. & Dinerstein, H. L. 1976, ApJ, 204, 1 61

Muller, C. A., Oort, J. H., & Raimond, E. 1963, C.R. Acad. Sci. Paris, 257, 1661 14

Münch, G. 1953, PASP, 65, 179 17

Münch, G. 1957, ApJ, 125, 42 17

Nasoudi-Shoar, S., Richter, P., de Boer, K. S., & Wakker, B. 2010, A&A, 520, A26 65

Pan, K., Federman, S. R., & Welty, D. E. 2001, ApJ, 558, L105 18, 82, 116

Peek, J. E. G., Heiles, C., Putman, M. E., & Douglas, K. 2009, ApJ, 692, 827 15

Péquignot, D. & Aldrovandi, S. M. V. 1986, A&A, 161, 169 80

Pfenniger, D., Combes, F., & Martinet, L. 1994, A&A, 285, 79 19

Pikel'Ner, S. B. 1967, Astr. Zu., 44, 915 9

Prochaska, J. X., Wolfe, A. M., Howk, J. C., et al. 2007, ApJS, 171, 29 49, 98

Richter, P. 2000, A&A, 359, 1111 66

Richter, P., Charlton, J. C., Fangano, A. P. M., Bekhti, N. B., & Masiero, J. R. 2009, ApJ, 695, 1631 98, 111

Richter, P. & de Boer, K. S. 2004, in Astrophysics and Space Science Library, Vol. 312, High Velocity Clouds, ed. H. van Woerden et al. (Kluwer Academic Publishers), 183 38, 85

Richter, P., de Boer, K. S., Widmann, H., et al. 1999, Nature, 402, 386 38, 85, 94, 113

Richter, P., Savage, B. D., Wakker, B. P., Sembach, K. R., & Kalberla, P. M. W. 2001, ApJ, 549, 281 38, 85, 94, 110, 111, 119

Richter, P., Sembach, K. R., & Howk, J. C. 2003a, A&A, 405, 1013 18, 38, 65, 82, 85, 91, 95, 110, 111, 116, 117, 119

Richter, P., Wakker, B. P., Savage, B. D., & Sembach, K. R. 2003b, ApJ, 586, 230 18, 37, 38, 65, 82, 85, 91, 92, 95, 110, 111, 116, 117, 119

Richter, P., Westmeier, T., & Brüns, C. 2005, A&A, 442, L49 98, 105, 108, 109, 111, 118, 119

Richter, P., Widmann, H., de Boer, K. S., et al. 1998, A&A, 338, L9 66

Routly, P. M. & Spitzer, Jr., L. 1952, ApJ, 115, 227 112

Sahnow, D. J., Moos, H. W., Ake, T. B., et al. 2000, ApJ, 538, L7 46

Savage, B. D. & de Boer, K. S. 1979, ApJ, 230, L77 49

Savage, B. D. & de Boer, K. S. 1979, ApJ, 230, L77 94

Savage, B. D. & de Boer, K. S. 1981, ApJ, 243, 460 49

Schwarz, U. J. & de Boer, K. S. 2004, in Astrophysics and Space Science Library, Vol. 312, High Velocity Clouds, ed. H. van Woerden et al. (Kluwer Academic Publishers), 55 95, 117

Sembach, K. R., Howk, J. C., Savage, B. D., & Shull, J. M. 2001, AJ, 121, 992 38, 94, 113

Shane, W. W. 1967, in IAU Symposium, Vol. 31, Radio Astronomy and the Galactic System, ed. H. van Woerden, 177 12

Shapiro, P. R. & Field, G. B. 1976, ApJ, 205, 762 11

Shull, J. M. & Beckwith, S. 1982, ARA&A, 20, 163 40

Shull, J. M., Tumlinson, J., Jenkins, E. B., et al. 2000, ApJ, 538, L73 37, 110, 111, 119

Sofia, U. J. & Jenkins, E. B. 1998, ApJ, 499, 951 74

Spangler, S. R. & Vázquez-Semadeni, E. 2007, in Astronomical Society of the Pacific Conference Series, Vol. 365, SINS - Small Ionized and Neutral Structures in the Diffuse Interstellar Medium, ed. M. Haverkorn & W. M. Goss, 347 16

Spitzer, L. 1978, Physical processes in the interstellar medium (New York Wiley-Interscience) 42, 43, 79

Spitzer, L., Drake, J. F., Jenkins, E. B., et al. 1973, ApJ, 181, L116 37

Spitzer, Jr., L. 1956, ApJ, 124, 20 9, 14

Spitzer, L. J. & Cochran, W. D. 1973, ApJ, 186, L23 72

Spitzer, L. J. & Zweibel, E. G. 1974, ApJ, 191, L127 40, 41, 71

Stanimirović, S., Putman, M., Heiles, C., et al. 2006, ApJ, 653, 1210 15, 112

Stanimirović, S., Weisberg, J. M., Hedden, A., Devine, K. E., & Green, J. T. 2003, ApJ, 598, L23 16

Stanimirović, S., Weisberg, J. M., Pei, Z., Tuttle, K., & Green, J. T. 2010, ApJ, 720, 415 16

Thom, C. & Chen, H.-W. 2008, ApJS, 179, 37 14, 15

van de Hulst, H. C. 1948, Harvard Observatory Monographs, 7, 73 42

Vazquez-Semadeni, E., Ostriker, E. C., Passot, T., Gammie, C. F., & Stone, J. M. 2000, Protostars and Planets IV, 3 19

Wakker, B. P. 1991, A&A, 250, 499 12

Wakker, B. P. 2001, ApJS, 136, 463 13, 14, 15

Wakker, B. P. 2004, in Astrophysics and Space Science Library, Vol. 312, High Velocity Clouds, ed. H. van Woerden, B. P. Wakker, U. J. Schwarz, & K. S. de Boer , 25 13

Wakker, B. P. 2006, ApJS, 163, 282 110, 111, 113, 119

Wakker, B. P., de Boer, K. S., & van Woerden, H. 2004, in Astrophysics and Space Science Library, Vol. 312, High Velocity Clouds, ed. H. van Woerden et al. (Kluwer Academic Publishers), 1 15

Wakker, B. P. & Mathis, J. S. 2000, ApJ, 544, L107 108

Wakker, B. P. & van Woerden, H. 1991, A&A, 250, 509 15

Wakker, B. P., York, D. G., Howk, J. C., et al. 2007, ApJ, 670, L113 14, 15

Wakker, B. P., York, D. G., Wilhelm, R., et al. 2008, ApJ, 672, 298 14, 15, 98

Walker, M. & Wardle, M. 1998, ApJ, 498, L125 19

Wardle, M. & Walker, M. 1999, ApJ, 527, L109 19

Watson, J. K. & Meyer, D. M. 1996, ApJ, 473, L127 17

Welty, D. 1998, in Lecture Notes in Physics, Berlin Springer Verlag, Vol. 506, IAU Colloq. 166: The Local Bubble and Beyond, ed. D. Breitschwerdt, M. J. Freyberg, & J. Truemper, 151–160 120

Welty, D. E. 2007, ApJ, 668, 1012 17, 18, 65

Welty, D. E. & Fitzpatrick, E. L. 2001, ApJ, 551, L175 17

Welty, D. E., Frisch, P. C., Sonneborn, G., & York, D. G. 1999, ApJ, 512, 636 49, 82, 96, 120

Winkel, B., Kalberla, P. M. W., Kerp, J., & Flöer, L. 2010, ApJS, 188, 488 50, 51, 98

Wolfire, M. G., Hollenbach, D., McKee, C. F., Tielens, A. G. G. M., & Bakes, E. L. O. 1995, ApJ, 443, 152 13, 95, 117

Wolfire, M. G., McKee, C. F., Hollenbach, D., & Tielens, A. G. G. M. 1995, ApJ, 453, 673 92

Woodgate, B. E., Kimble, R. A., Bowers, C. W., et al. 1998, PASP, 110, 1183 46

Remark: The small numbers after the references indicate the page numbers where the citations occur.

Acknowledgements

First of all, I like to thank my supervisors, **Klaas S. de Boer**, and **Philipp Richter**, who made this PhD-thesis possible. Thank you Klaas for being there through the past years, keeping up the pressure when I needed to be pushed, and leaving me on my own in between with the freedom that I needed to find my own way; and for teaching me how to write reader-friendly papers. Thank you also for always keeping an eye on me, for caring and being open to talk to. Thank you Philipp for inspiring me and guiding me into the right direction, and for making our meetings and discussions most efficient and fruitful. Thank you for believing in me, and giving your full support whenever it was required.

I would also like to thank **Uli Klein** for being the second referee of this thesis.

I am grateful to **Nadya Ben Bekhti** and **Jürgen Kerp** for their support for the last part of this thesis. Many thanks to **Nadya** for taking me into her group when (without her knowing at the time) it was most needed, and also for the help with the optical data, for giving careful comments on this thesis, and for all the good times.

Special thanks to **Ole Marggraf** for being there whenever I panicked, whether over a referee report or an error I could have made, or having an idea in my head I needed to get straight. Thank you for always being so pleasant to talk with, and for listening and giving thoughtful feedbacks, for installing my laptop, and for giving careful comments on most parts of this thesis.

Moving to a foreign country without knowing anyone, or the language, is not all smooth and easy. I guess it is particularly tough when you don't really want to leave in the first place. But astronomy does not leave you much choice, and in the end, probably no real home. But for sure, a lot of interesting people. Here I would like to acknowledge the ones who mattered the most along the way, and for this thesis. **Michael, Laia, Gautam,** and **Matthias**, you guys made Stockholm observatory such a great place. Our last trip to the airport (well I mean the first last one), was one of my saddest. And the visits, every second month, were most fun. Heartfelt thanks to my brother **Kavoos** for meeting my leaving with nothing but encouraging happiness, even though that left him with extra burden.

Of course, I came to meet some really great people in Bonn inside and outside AIFA... one in particular, who probably made all the difference!

Here, I would like to thank all of **you** who have created a nice pleasant place at the institute through the years, and great distractions outside. As fun as it may be seeing your names in the Acknowledgements, I do not want to risk leaving anyone behind. You know who you are. However, the last couple of years in particular, would not have been easy without

the cheerful and yet casual supportive words of friends. I am glad that you moved here **Sofia**. On the same line, thank you **Patrick**, **Sibylle**, and also my officemates **Jörg** and **Geneviève**. Thank you Jörg also for all the good stuff that you shared with me, and for bringing me closer to my persian side.

I would also like to thank my **father** for his weekly support and encouragements, and for his sacrifices through the years. Finally, saving the best at last, I would like to thank my dear friend **Maria** for always being there and constantly caring, and my most favourite guys, my dear brother **Kavoos** and my beloved **Marco**, for inspiring me and supporting me in all possible ways, and for believing in me more than I do. Thank you **Marco** also for putting up with me in my particularly stressed form during the last year, for giving me constant support and optimism, and for a million other things. Whether for my whole life, or for the passed few years, I sure am glad to have the three of you in my life!